Dissertation
submitted to the
Combined Faculties of the Natural Sciences and Mathematics
of the Ruperto-Carola-University of Heidelberg, Germany
for the degree of
Doctor of Natural Sciences

Put forward by
Juris Ulmanis
born in: Riga, Latvia
Oral examination: July 9th, 2015

Universality and non-universality in the heteronuclear Efimov scenario with large mass imbalance

Referees: **Prof. Dr. Matthias Weidemüller**
Prof. Dr. Selim Jochim

Abstract

This thesis investigates universal and non-universal aspects of few-body physics in a mass-imbalanced mixture of ultracold bosonic ^{133}Cs and fermionic ^{6}Li atoms. For this purpose an experimental apparatus for the creation of quantum degenerate gases has been constructed. Using radio-frequency association of weakly-bound LiCs molecules and additional atom-loss spectroscopy we determine the two-body interaction properties between Li and Cs atoms at low collision energies. The analysis with a coupled-channels calculation yields precise singlet and triplet electronic ground state molecular potential curves, from which scattering lengths and positions of Fano-Feshbach resonances are extracted. These results represent almost a tenfold improvement over the previous determination, and are used to study few-body recombination processes and, for the first time, their dependence on the interaction strength between the heavy atoms close to two broad scattering resonances at various temperatures. Measurements of three-body loss rates reveal two series of three and two consecutive $LiCs_2$ Efimov resonances that demonstrate the universal scaling factor 4.9 between the first and second excited state resonances. The ground state resonance deviates from the discrete scaling law. By the use of hyperspherical formalism with either pairwise zero-range or Lennard-Jones model potentials we identify the van der Waals interaction between Cs atoms as a significant source of these modifications.

Zusammenfassung

Diese Arbeit untersucht universelle und nicht-universelle Aspekte der Wenigteilchenphysik in einem Bose-Fermi Gasgemisch aus ultrakalten ^{133}Cs und ^{6}Li Atomen. Hierfür wurde eine experimentelle Apparatur zur Erzeugung quantenentarteter Gase aufgebaut. Mit Hilfe von Radiofrequenzassoziation schwach gebundener LiCs Moleküle und zusätzlicher Verlustspektroskopie werden die Eigenschaften der Zweikörperwechselwirkung zwischen Lithium und Cäsium bei niedrigen Stoßenergien bestimmt. Die Analyse dieser Messungen mit einer *coupled-channels* Rechnung ergibt präzise Singulett- und Triplettpotentialkurven des Molekulargrundzustands, aus denen die Streulängen und Positionen der Fano-Feshbachresonanzen extrahiert werden. Diese Ergebnisse stellen eine fast zehnfache Verbesserung gegenüber der früheren Bestimmung dar und werden verwendet, um Wenigteilchenrekombinationsprozesse und erstmals deren Abhängigkeit von der Stärke der Wechselwirkung zwischen den schweren Cäsiumatomen in der Nähe der beiden breiten Li-Cs Streuresonanzen bei verschiedenen Temperaturen zu untersuchen. Dreikörperverlustratenmessungen weisen zwei Serien von drei beziehungsweise zwei aufeinanderfolgenden Efimovresonanzen auf, die den universellen Skalierungsfaktor von 4,9 zwischen dem ersten und zweiten angeregten Zustand demonstrieren. Die Resonanz des Grundzustands weicht von dem diskreten Skalengesetz ab. Mit der hypersphärischen Darstellung, die die Paarwechselwirkung entweder durch nullreichweitige oder Lennard-Jones Modellpotentiale beschreibt, wird die Van-der-Waals-Wechselwirkung zwischen Cäsiumatomen als eine der bedeutendsten Ursachen für diese Abweichungen identifiziert.

Parts of this thesis are based on the following manuscripts and publications:

- **Finite-range effects in universal three-body recombination of ultracold Li and Cs atoms**
  J. Ulmanis, S. Häfner, R. Pires, E.D. Kuhnle, M. Weidemüller, Y. Wang, C.H. Greene
  Manuscript in preparation

- **Universal three-body recombination in an ultracold Li-Cs mixture**
  J. Ulmanis, S. Häfner, R. Pires, E.D. Kuhnle, M. Weidemüller, D. Petrov, F. Werner
  Manuscript in preparation

- **Universality of weakly bound dimers and Efimov trimers close to Li-Cs Feshbach resonances**
  J. Ulmanis, S. Häfner, R. Pires, E.D. Kuhnle, M. Weidemüller, E. Tiemann
  New Journal of Physics **17**, 055009 (2015)

- **Observation of Efimov Resonances in a Mixture with Extreme Mass Imbalance**
  R. Pires*, J. Ulmanis*, S. Häfner, M. Repp, A. Arias, E.D. Kuhnle, M. Weidemüller
  Physical Review Letters **112**, 250404 (2014)
  * Both authors contributed equally to this work.

- **Analyzing Feshbach Resonances – A ^{6}Li-^{133}Cs case study**
  R. Pires, M. Repp, J. Ulmanis, E.D. Kuhnle, M. Weidemüller, T.G. Tiecke, C.H. Greene, B.P. Ruzic, J.L. Bohn, E. Tiemann
  Physical Review A **90**, 012710 (2014)

- **Observation of interspecies ^{6}Li-^{133}Cs Feshbach resonances**
  M. Repp, R. Pires, J. Ulmanis, R. Heck, E.D. Kuhnle, M. Weidemüller, E. Tiemann
  Physical Review A **87**, 010701 (2013)

The author furthermore contributed to the following publications:

- **A helical Zeeman slower for sequential loading of two elements with large mass difference into optical dipole traps**
  M. Repp, R. Pires, J. Ulmanis, S. Schmidt, R. Müller, K. Meyer, R. Heck, E.D. Kuhnle, M. Weidemüller
  Manuscript in preparation

- **Ultracold Molecules Formed by Photoassociation: Heteronuclear Dimers, Inelastic Collisions, and Interactions with Ultrashort Laser Pulses**
  J. Ulmanis, J. Deiglmayr, M. Repp, R. Wester, M. Weidemüller
  Chemical Reviews **112**, 4890 (2012)

Contents

Chapter 1

Introduction

The binding of three pairwise resonantly interacting particles into three-body states, today often termed the Efimov effect, is one of the most fundamental building blocks in quantum mechanics [Efimov, 1970, 1973, 1979]. It is characterized the best by its extraordinary properties, one of which is the existence of an infinite number of bound three-body states, Efimov states (see Fig. 1.1, left panel), even when the underlying two-body interactions are not strong enough to support a single bound two-body state. Therefore, exactly as the three Borromean rings would fall apart, if only a single one was removed, the whole three-body system disintegrates as soon as one particle is missing, and each constituent goes its own way. The Efimov trimer energies and their overall spatial extent are following a geometrical progression, a discrete scaling law, that is governed solely by the quantum statistics, masses and number of resonant pairwise interactions. These states still persist when the two-body interaction strength is reduced, although their count reduces to a finite value. Since its first discovery, Efimov's idea has transformed now into one of the basic paradigms that allows us to examine and further our understanding about few-body physics [Braaten and Hammer, 2006, 2007; Hammer and Platter, 2010; Greene, 2010; Ferlaino et al., 2011; Frederico et al., 2013; Wang et al., 2013].

The important role of the Efimov effect in modern quantum mechanics is based on its predicted universal behavior for microscopically different three-body systems. The interaction between a pair of particles in the low-energy limit is described by the two-body s-wave scattering length a. Whenever its magnitude significantly exceeds the range of interparticle interactions r_0, the two-body wavefunction greatly extends into the regions, where the pairwise potentials do not exist anymore. Thus the specific details of the individual potential become irrelevant, giving rise to universal bound state energies close to the scattering threshold and halo wavefunctions, both of which are governed by the sole parameter a – a single length scale that characterizes the whole system. This essence of universality directly transfers from the two-body into the three-body realm, where it takes the form of the Efimov effect.

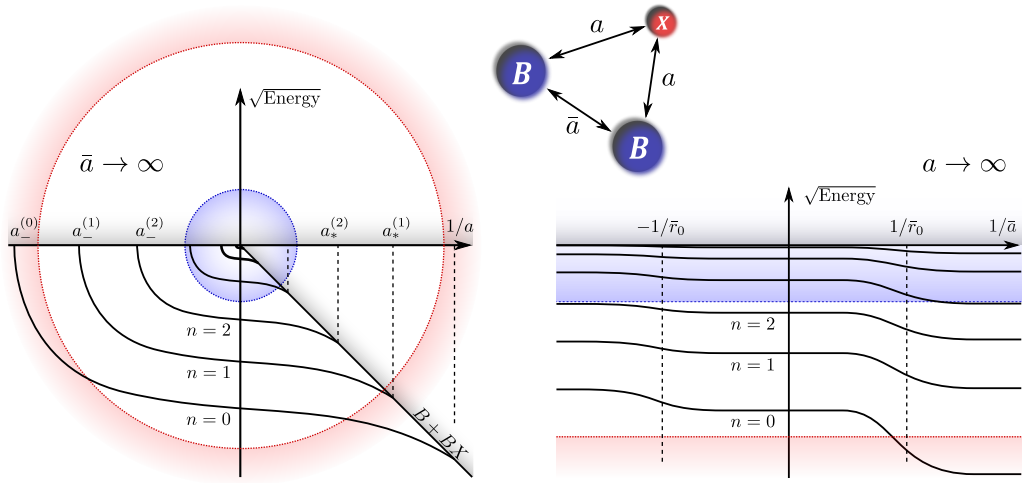

Figure 1.1: A sketch of the heteronuclear Efimov scenario for two identical bosons B and one distinguishable particle X. Left panel: a few of the deepest bound three-body energy levels as a function of the interspecies scattering length a between particles B and X. Atom-dimer scattering threshold is given as $B + BX$. The same structure manifests for any other system where the Efimov effect exists. Right panel: a few of the deepest bound energy levels as a function of the intraspecies scattering length $\bar{a}$ between bosons B for $a \to \infty$ and length scale $\bar{r}_0$ of the two-body interaction between B and B. The window of universality ($\Lambda \gg |a| \gg \max(r_0, \bar{r}_0)$) in both panels is located between the temperature (blue shaded area) and short-range (red shaded area) dominated regimes, which are characterized by the de Broglie wavelength Λ and the additional length scale r_0 of the two-body interaction between B and X, respectively.

In this way it manifests for any system interacting via short-range forces alike, independent if it is the van der Waals force between atoms or the strong force between nucleons [Nielsen et al., 2001; Braaten and Hammer, 2006; Hammer and Platter, 2010; Zinner and Jensen, 2013].

An even richer form of the Efimov effect emerges in a three-body system that is composed of two identical bosonic particles and a third one that is different. The intraparticle interaction between the like particles, which is described by the two-body s-wave scattering length $\bar{a}$ and the length scale $\bar{r}_0$, gives rise to two new length scales in the problem. Depending on their exact magnitude the Efimov scenario manifests differently. Two limiting regimes exist that can be identified by the number of resonant pairwise interactions, which is two, if $|\bar{a}| = 0$, or three, if $\bar{a} \to \infty$ [Braaten and Hammer, 2006]. All other values of $\bar{a}$ connect these cases. They are separated by the parameter $\bar{r}_0$ that contains the specific details of the intraspecies short-range interactions, which now becomes relevant for this transition (see Fig. 1.1, right panel). Remarkably, the complete progression of Efimov states is expected to adjust to the exact, finite value of $\bar{a}$ even in the resonant limit $a \to \infty$

[Wang et al., 2012d]. Thus, if an Efimov series is known at a single value of $\bar{a}$, it can be used to predict its behavior at others. In this work we make the first experimental step towards understanding such three-body systems with an ultracold mixture of fermionic ^{6}Li and bosonic ^{133}Cs atoms.

The Efimov effect and universal three-body problems can be often found in various areas of modern physics. Triatomic helium $^4He_3$ was the very first system, for which the existence of Efimov states was suggested [Lim et al., 1977; Nakaichi-Maeda and Lim, 1983; Esry et al., 1996; Nielsen et al., 1998; Blume and Greene, 2000]. Because of the accidental fine-tuning by nature, the scattering length between two identical ^{4}He atoms is $a = 90.4$ Å (1 Å=0.1 nm), while the extension of the van der Waals force is only around 5 Å [Cencek et al., 2012]. As a result, the helium potential supports a single bound two-body state, and two bound three-body states, for which the energies and their structure are precisely known from first principle calculations [Blume and Greene, 2000; Blume et al., 2000; Hiyama and Kamimura, 2012a,b; Blume et al., 2014]. Thus it was only a question of time until the ground trimer state was observed [Schöllkopf and Toennies, 1994]. Unfortunately as it is often in physics, it turned out that the verification of the excited trimer state is a more challenging feat [Hegerfeldt and Köhler, 2000; Bruch et al., 2002; Brühl et al., 2005], which only recently, more than 30 years after its initial prediction, came to an triumphant, long-sought conclusion. The exited $^4He_3$ state has at last been experimentally demonstrated in an impressive *tour de force* experiment [Kunitski et al., 2015], almost perfectly recovering the long-established predictions from the few-body theories and previous experiments. Observation of an universal $^4He_4$ tetramer might also be feasible [Hiyama and Kamimura, 2014].

Halo nuclei are the most prototypical examples of universality in nuclear physics [Zhukov et al., 1993; Hansen et al., 1995; Jensen et al., 2004; Frederico et al., 2012; Riisager, 2013]. The nuclei of ^{11}Be or ^{6}He and ^{11}Li, where a compact core of nucleons is surrounded by one or two loosely bound neutrons, respectively, are major archetypes for studies of universal properties in two- and three-body systems that are composed of different particles. The existence of Efimov trimer states have been speculated in many isotopes [Zhukov et al., 1993; Carlson and Schiavilla, 1998; Fedorov et al., 1994; Frederico et al., 2012], most recently in ^{22}C [Acharya et al., 2013], the heaviest observed Borromean nucleus so far [Tanaka et al., 2010], and ^{60}Ca [Hagen et al., 2013], in this way challenging the experimentalists and the present understanding of nuclear behavior in extreme conditions along the neutron drip line [Kemper and Cottle, 2010]. Studies of these and similar systems can have deep consequences not only for nuclear physics and astronomy, but also the potential to reveal new phenomena and three-body effects that are applicable in other fields as well.

The universal aspects of the Efimov effect extends well beyond the scope of

atomic and nuclear physics. The Hamiltonian of the Efimov effect is formally equivalent to the one of an electron bound by a small electric dipole [Lévy-Leblond, 1967], which also supports an infinite number of long-range dipole-bound states [Crawford, 1967; Camblong et al., 2001; Giri et al., 2008]. This has implications for chemistry in electron-anion scattering and binding [Domcke and Cederbaum, 1981; Desfrançois et al., 1996; Jordan and Wang, 2003; Simons, 2008] and positron-molecule complexes [Gribakin et al., 2010]. Similar three-body scenarios have been suggested in exotic biological [Pal et al., 2013, 2015] and condensed-matter [Nishida et al., 2013] systems. Besides the universal properties that extend our knowledge about the fundamental quantum physics, the three-body problem in general is relevant for many areas in physics that are not necessarily connected to the Efimov effect. Major examples of important weakly-bound few-body structures that are intensively investigated are Rydberg aggregates and macrotrimers [Liu and Rost, 2006; Liu et al., 2009; Bendkowsky et al., 2010; Han, 2010; Samboy and Côté, 2013; Schempp et al., 2014], few-nucleon systems [Zhukov et al., 1993; Carlson and Schiavilla, 1998], and vibrationally bound molecules [Manz et al., 1982, 1983; Macek, 1986, 2007; Fleming et al., 2014]. These large and floppy objects with long spatial extensions and energies that are just barely keeping them together have the potential to elucidate further aspects of the few-body problem.

The advent of laser cooling, production and control of ultracold atomic gases [Chu, 1998; Cohen-Tannoudji, 1998; Phillips, 1998; Ketterle, 2002; Cornell and Wieman, 2002] has opened a new epoch for the study of the universal and non-universal aspects of few-body physics. While in the previously described systems the existence of the Efimov effect depends on the accidental fine-tuning of interparticle interactions by nature, in ultracold gases the scattering length a can be experimentally tuned from $a \to +\infty$ to $a \to -\infty$ with extreme precision. This on magnetic Fano-Feshbach resonances [Chin et al., 2010; Köhler et al., 2006; Fano, 1961; Feshbach, 1958, 1962] based concept allows now experimentalists to routinely create strongly interacting binary systems with universal halo character and bound state energies, and consequently, the Efimov effect, at will. The signatures of the trimer states that emerge in the low-energy threshold scattering observables can be simply measured by observing the suppression or enhancement of ultracold three-atom recombination rates [Esry et al., 1999; Nielsen and Macek, 1999; Bedaque et al., 2000]. Exactly in this way the position of where an Efimov state crosses the three-body dissociation threshold, and also the first demonstration of an Efimov state was made [Kraemer et al., 2006]. Since then such recombination-rate spectroscopy, reminiscent, but not limited to, level-crossing spectroscopy from atomic and molecular physics, has often been the method of choice for the exploration of few-body phenomena in ultracold atomic gases (see Sect. 3.1 for a more extensive account on the recent experimental developments in this field).

The wealth of scientific few-body topics that can today be addressed with ultracold quantum gases has exploded well beyond the original Efimov scenario. The ability to create ultracold polar molecules in the absolute ground state [Ni et al., 2008; Ospelkaus et al., 2008; Deiglmayr et al., 2008; Molony et al., 2014; Takekoshi et al., 2014; Park et al., 2015] and samples of ultracold atoms with a permanent magnetic moment [Giovanazzi et al., 2002; Lu et al., 2011; Aikawa et al., 2012] that interact through long-range anisotropic potentials [Lahaye et al., 2009; Carr et al., 2009; Quéméner and Julienne, 2012] have inspired active research on few-particle systems, where the main binding mechanism is the dipole-dipole interaction [Ticknor and Rittenhouse, 2010; Wang and Greene, 2012; Wang et al., 2012a, 2011b,c]. The evidence of bound four- and five-body states in ultracold homonuclear gases [Ferlaino et al., 2008, 2009; Pollack et al., 2009; von Stecher, 2011; Zenesini et al., 2013] has triggered extensive studies of universal tetramers [Hammer and Platter, 2007; D'Incao et al., 2009b; von Stecher et al., 2009; Hadizadeh et al., 2011, 2012; Wang et al., 2012c; Blume, 2012; Frederico et al., 2013; Blume and Yan, 2014] and proposals for N-body universal cluster states [Blume and Greene, 2000; Mehta et al., 2009; von Stecher, 2010; Yamashita et al., 2011; Frederico et al., 2013; Gattobigio and Kievsky, 2014; Blume and Yan, 2014]. The inclusion of an increasingly larger number of particles is especially intriguing, since it probes the transition from few-to many-body physics, which is an exhaustive topic on its own (see, for example [Bloch et al., 2008; Dalfovo et al., 1999; Giorgini et al., 2008]). Essentially similar ideas are investigated in ultracold gases consisting of just a few atoms in well defined internal and external degrees of freedom [Serwane et al., 2011]. These experiments allow one to observe the transition from few- into a many-body system almost continuously [Wenz et al., 2013], and, in addition, deliver a deep understanding of the intricate structure of a few-body system, where quantum statistics and spins play the leading roles [Zürn et al., 2012, 2013; Deuretzbacher et al., 2014; Kaufman et al., 2014].

While there has been a tremendous theoretical progress in few-body ultracold atomic physics, the experimental realization of the envisioned universal scenarios has turned out to be more challenging. This lies in the extreme temperature and magnetic field stability regimes that are required for these experiments. For unambiguous verification of the discrete scaling law $a_-^{(n)} = \lambda^n a_-^{(0)}$ that is predicted by the Efimov scenario, the observation of at least three consecutive trimer states in the universal regime is necessary (see Fig. 1.1, left panel). In a homonuclear atomic system this might seem an impossible feat, since consecutive three-body resonances are spaced by a scaling factor $\lambda = 22.7$. Thus, if the first, the ground state, resonance is found at[1] $a_-^{(0)} \sim 900\ a_0$, then the third, the second exited state, should be located at $a_-^{(2)} \sim 460000\ a_0$. For low-energy scattering observables not to saturate at the magnitude of the thermal de Broglie wavelength, this tunability

[1] a_0 denotes one Bohr radius, which corresponds to 5.29177×10^{-11} m.

of a requires temperatures in the tens of pK range, which with the current technology is hardly accessible. Nevertheless, the first excited state can still be observed, as recently demonstrated in the seminal experiments with homonuclear Cs [Huang et al., 2014b] and Li [Williams et al., 2009] gases. The situation can be relieved in heteronuclear systems, for which the scaling factor λ is drastically reduced [D'Incao and Esry, 2006; Braaten and Hammer, 2006]. This leads to a much denser resonance spectrum, and, consequently, the observation of a series of more than two states is feasible.

In this thesis we explore the universal and non-universal Efimov scenario in a mass imbalanced mixture of ultracold ^{6}Li and ^{133}Cs gases. This is an ideal system for the studies of few-body phenomena, since the scaling factor is reduced to $\lambda = 4.9$ due to the large mass ratio. This has enabled us to observe three consecutive Efimov resonances for the first time. Intriguingly, not all of them are found within the window of universality, which is a perfect setting for the investigation of the finite-range influence on the three-body spectrum. Indeed, in this work we identify deviations from the universality and interpret them as the consequence of van der Waals interactions at the characteristic short-range distances, which has not been possible in any other system studied so far. Furthermore, in our system two, instead of a single, scattering lengths can be controlled by magnetic field dependent Feshbach resonances. Therefore, we have been able to investigate the Efimov scenario not only as a function of the interspecies scattering length a (Fig. 1.1, left panel), but also make one of the first experimental steps towards understanding its dependence on the intraspecies scattering length $\bar{a}$ (Fig. 1.1, right panel). We have performed pioneering experiments that demonstrate the formation of Efimov series at two different values of $\bar{a}$ in a single heteronuclear system. These studies not only elucidate the universality and finite-range deviations from it, but also constitute a new challenge and test for current few-body theories.

We start this thesis with a thorough investigation of the Li-Cs scattering properties in the energetically lowest scattering channels in chapter 2. The previous determination and analysis of the Feshbach resonances is improved by radio-frequency spectroscopy measurements. They deliver significantly more precise mapping between the externally applied magnetic field and the Li-Cs scattering length, which is critical for an appropriate analysis of the Efimov scenario in this system. We continue by the observation of a series of three consecutive Efimov resonances via three-body recombination spectroscopy in chapter 3. To illustrate the universal nature of the observed resonances we apply a zero-range interaction model. Remarkably, this demonstrates both, the universal and non-universal behavior of the Efimov series, where the ground state resonance do not follow the ideal scaling law. We explain the origin of this deviation in chapter 4 by showing how short-range interaction potentials can lead to shifts of the Efimov resonance positions. Inclu-

sion of more realistic van der Waals type model potentials recovers the experimental findings. Although they do not exactly recapture the short-range physics, such as, for example, deeply bound molecular states, they are excellent in modeling low-energy scattering problems and extraction of experimental observables. To test this approach we record another series of two consecutive Efimov resonances in a different Li-Cs scattering channel that is characterized by a different Cs-Cs background scattering length. The theoretical analysis of this series indicates that the internal atomic structure of the colliding atom pairs may manifest in a yet more complicated structure of three-body scattering observables. Finally we conclude by summarizing the results and giving a brief outlook of possible future avenues for ultracold Li-Cs experiments in chapter 5.

Chapter 2

Two-body interactions between Li and Cs atoms

Parts of this chapter are based on the following publications:

Universality of weakly bound dimers and Efimov trimers close to Li-Cs Feshbach resonances
J. Ulmanis, S. Häfner, R. Pires, E.D. Kuhnle, M. Weidemüller, E. Tiemann
New Journal of Physics **17**, 055009 (2015)

Analyzing Feshbach resonances: A ^{6}Li-^{133}Cs case study
R. Pires, M. Repp, J. Ulmanis, E.D. Kuhnle, M. Weidemüller, T.G. Tiecke, C.H. Greene, B.P. Ruzic, J.L. Bohn, E. Tiemann
Physical Review A **90**, 012710 (2014)

Observation of interspecies ^{6}Li-^{133}Cs Feshbach resonances
M. Repp, R. Pires, J. Ulmanis, R. Heck, E.D. Kuhnle, M. Weidemüller, E. Tiemann
Physical Review A **87**, 010701 (2013)

All coupled-channels calculations that are presented in this chapter have been performed by Prof. E. Tiemann from University of Hannover, Germany.

In this chapter we investigate the binary scattering properties of an ultracold Li-Cs mixture and develop a theoretical and experimental framework, on which the further exploration of few-body effects that are discussed throughout this thesis will be based. We start by establishing the basic theoretical structure that is used to describe ultracold scattering in Sect. 2.2. We introduce the s-wave scattering length and show its intrinsic connection to the internal structure of the colliding atoms. This gives rise to magnetically tunable Feshbach resonances, and the weakly bound universal dimer. We continue by presenting the typical experimental approach for

producing an ultracold mixture of Li and Cs atomic gases in a single, predetermined scattering channel in Sect. 2.3. It is followed by the description of the two most crucial experimental techniques that are employed throughout this thesis for controlling and probing interactions, namely, homogenous magnetic field generation, and radio-frequency and microwave-frequency pulses. Finally, in Sect. 2.4 we explain the measurements of weakly bound LiCs Feshbach dimers, and the procedure for obtaining the LiCs singlet and triplet molecular potential curves of the electronic ground state manifold with the help of coupled-channels calculation. It yields, up to date, the most precise parametrization of Li-Cs scattering properties in the explored magnetic field range. This knowledge will be critical for appropriate analysis of three-body physics that is explored in chapters 3 and 4 of this thesis.

2.1 Interactions in ultracold mixtures of Li and Cs atoms

The tunability of interactions between two ultracold, colliding particles is one of the most fundamental capabilities of modern quantum gas experiments. The tuning is achieved by magnetic field dependent interparticle scattering resonances, called Feshbach resonances (FR), at which a two-body bound state crosses the scattering threshold. These resonances are routinely employed to tune the interaction strength between the colliding particles [Chin et al., 2010] and to produce weakly bound dimers by ramping up or down the external magnetic field [Köhler et al., 2006]. They can be used to create strongly correlated many-body systems [Bloch et al., 2008], quasiparticles [Massignan et al., 2014], and explore intriguing topics in few-body physics [Braaten and Hammer, 2006; Wang et al., 2013]. However, the ability to study any of these fascinating systems, a as well as the underlying principles, on which the behavior of such systems is based, relies on precise knowledge of the properties of the particular FR.

The central quantity that governs an ultracold collision process, and therefore most of the physics at such temperatures, is the two-body s-wave scattering length a. The inelastic three-body scattering rate near a FR scales as a^4, resulting in magnetic field dependent atom losses that can be used to map out how a depends on the external field [Fedichev et al., 1996; D'Incao and Esry, 2005]. During the last decade, such atom loss spectroscopy in combination with theoretical models has become a standard tool for the determination of specific interparticle interaction properties [Chin et al., 2010].

These methods yield an excellent representation of the overall FR spectrum. The result of an extensive atom-loss spectroscopy of Li-Cs Feshbach resonances [Repp, 2013; Repp et al., 2013; Tung et al., 2013], part of which is shown in Fig. 2.1, is

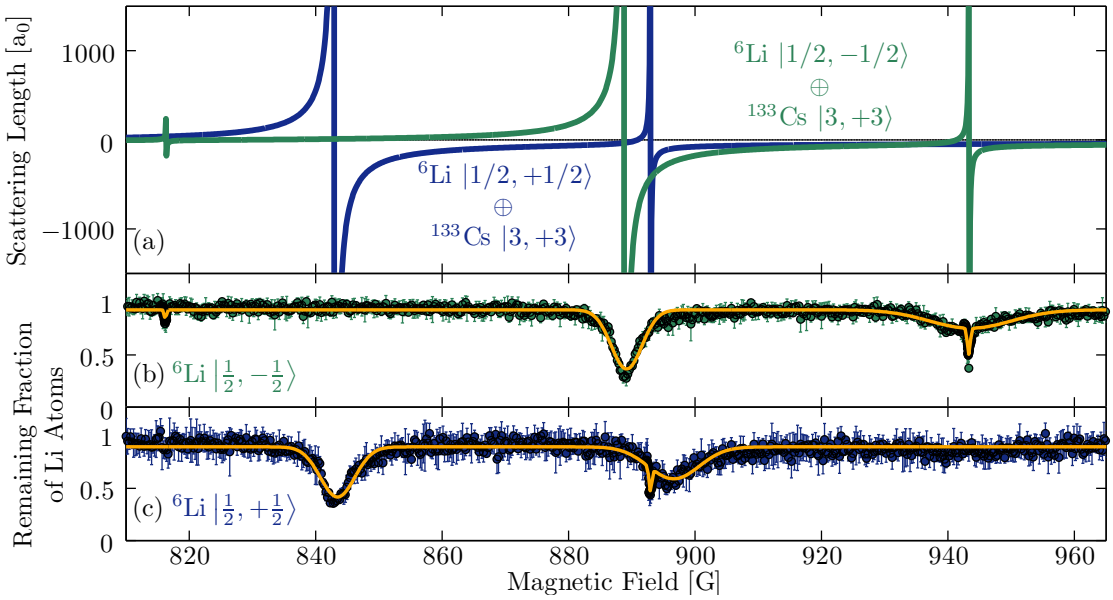

Figure 2.1: Li-Cs *s*-wave Feshbach resonances for the two energetically lowest scattering channels [Repp et al., 2013]. (a) Scattering length dependence on the magnetic field for the two energetically lowest Li-Cs scattering channels. (b) and (c) trap loss spectra and Gaussian profile fits to the loss data for Li$|1/2, -1/2\rangle$ and Li$|1/2, 1/2\rangle$ spin states. Each feature in the loss spectra corresponds to a Feshbach resonance in the scattering length. The additional loss features correspond to resonances in different Cs spin channels that are not shown here. Figure adapted from [Pires, 2014].

one illustration of this. In these measurements a total of 19 interspecies scattering resonances could be detected for the two energetically lowest spin states in the magnetic field range between 500 G and 1000 G (only 7 of them are shown in the figure). The explanation of these atom-loss spectra relied on precise models of magnetic field-dependent scattering length. Excellent agreement was obtained by several numerical methods, including coupled-channels (cc) calculation, asymptotic bound-state model (ABM), or multichannel quantum defect theory (MQDT) [Pires et al., 2014a; Pires, 2014]. All of the approaches describe the FRs with a sub-Gauss accuracy, thus the particular choice of the applied method depends on the required degree of precision for the final result and computational complexity. In this work we will exclusively use the cc approach, as it incorporates the least amount of assumptions out of the three models, and allows a straightforward calculation of the molecular energies required for FR pole determination (see Sect. 2.4).

However, not all of the observed atom losses can be unambiguously attributed to an increasing two-body scattering length. Especially when a becomes large, not only immediate loss of three atoms from the trap, but also other processes, for example, weakly-bound dimer formation and subsequent secondary losses may occur. This

can lead to shifts and asymmetric broadening of the loss signals [Dieckmann et al., 2002; Bourdel et al., 2003; Weber et al., 2008; Machtey et al., 2012a; Zhang and Ho, 2011; Khramov et al., 2012] thus weakening the relation to the functional dependence of the scattering length alone. A precursor to such underlying dynamics can already be seen in the asymmetric loss profiles of the broad Li-Cs Feshbach resonances in Fig. 2.1.

More accurate mapping between the magnetic field and scattering length can be obtained by going further than a simple atom loss spectrum. The most precise scattering length measurements so far are delivered by direct radio-frequency (rf) [Klempt et al., 2008; Regal et al., 2003; Bartenstein et al., 2005; Ospelkaus et al., 2006; Maier et al., 2010; Wu et al., 2012; Zürn et al., 2013; Huang et al., 2015] and magnetic field modulation [Weber et al., 2008; Fuchs et al., 2008; Thompson et al., 2005; Papp and Wieman, 2006; Lange et al., 2009; Thalhammer et al., 2009; Gross et al., 2010; Berninger et al., 2013; Dyke et al., 2013] spectroscopy of the least-bound molecular states. Since a FR intrinsically originates from the coupling of the scattering channel with such a molecular state, its energy E in the vicinity of the FR can be connected to the scattering length through the relation $E \propto a^{-2}$ [Gribakin and Flambaum, 1993; Góral et al., 2004]. By mapping the magnetic field dependence of the binding energy of this state, it is possible to study exclusively the two-body problem, and the extraction of a is less prone to systematic effects. For the specific case of Li-Cs, we employ rf spectroscopy throughout this thesis, and in this way reduce the uncertainty of the Li-Cs Feshbach scattering length parametrization by almost a factor of 20 for the broad Feshbach resonances [Ulmanis et al., 2015] in comparison to the initial atom-loss experiments [Repp et al., 2013; Tung et al., 2013].

2.2 Low-energy scattering in ultracold quantum gases

The elementary interaction mechanism of two neutral particles is a two-body collision in a potential that depends on the relative distance between them. In this section we shortly review the basic formalism of the scattering theory that is necessary to describe such process in the ultracold temperature regime where the dynamics are dominated by quantum threshold laws and single partial wave scattering. We start by recalling the concept of scattering length and collision cross section and their dependence on the quantum statistics in Sect. 2.2.1. It is followed by a discussion how the internal structure of the colliding particles leads to the emergence of Feshbach resonances that can be employed to control the interaction between the scattering partners in Sect. 2.2.2 and 2.2.3.

2.2.1 Basic physics of two-body scattering at ultracold temperatures

There exists many textbooks and lecture notes that treat the ultracold two-body scattering rigorously, see, for example, [Joachain, 1984; Ketterle et al., 1999; Schwabl, 2007; Dalibard, 1999; Landau and Lifshitz, 1991; Sakurai and Napolitano, 2010]. Here we give a short summary of the most important concepts that are required to understand the interaction between two colliding particles.

The Schrödinger equation in center-of-mass reference frame for two particles with mass m_1 and m_2 that interact through a potential $U(\vec{r})$ reads

$$\left[-\frac{\hbar^2}{2\mu}\vec{\nabla}^2 + U(\vec{r})\right]\psi(\vec{r}) = \frac{\hbar^2 k^2}{2\mu}\psi(\vec{r}), \tag{2.1}$$

where $\vec{r}$ denotes the interparticle separation, $k = \sqrt{2\mu E}/\hbar$ is the wavevector of the relative motion for positive collisional energy E, and $\mu = m_1 m_2/(m_1 + m_2)$ is the two body reduced mass. In general, the short-range part of the interaction potential $U(\vec{r})$ can take on any form. However we request that at large interparticle separation the potential vanishes, which corresponds to setting $U(\vec{r}) = 0$ for $|\vec{r}| \gg r_0$, where r_0 is a length scale that characterizes the short-range extent of the scattering potential. Then the wavefunction $\psi(\vec{r})$ in this region can be expressed by its asymptotic form

$$\psi(\vec{r}) = e^{ikr} + f(\theta, k)\frac{e^{ikr}}{r} \tag{2.2}$$

consisting of an incoming plane wave and an outgoing spherical wave with an angle θ and k dependent scattering amplitude $f(\theta, k)$.

With these basic constituents we can now introduce the partial wave expansion. Due to symmetry arguments for radial potentials $U(r)$ the scattering amplitude depends only on the angle θ between the colliding particle normal vectors, and the wavefunction can be expanded in the basis of spherical harmonics $Y_l^m(\theta, \phi)$ as

$$\psi(\vec{r}) = \sum_{l=0}^{\infty}\sum_{m=-l}^{l} Y_l^m(\theta,\phi)\frac{u_{k,l,m}(r)}{r}, \tag{2.3}$$

where $u_{k,l,m}(r)$ is the radial wavefunction that depends on k, the quantum number l that characterizes the angular momentum of the colliding particles and its projection m. Inserting this ansatz into the Schrödinger equation (2.1) one obtains

$$f(\theta, k) = \frac{1}{2ik}\sum_{l=0}^{\infty}(2l+1)(e^{2i\delta_l} - 1)P_l(cos(\theta)), \tag{2.4}$$

where P_l denotes the Legendre polynomial, and we have introduced a phase shift δ_l between the incoming and outgoing wave. In the asymptotic region it quantifies the effect of the short-range interaction potential on the scattering wavefunction and can be characterized by the Wigner threshold law $\delta_l \propto k^{2l+1}$ [Wigner, 1948].

The quantum statistics of the particles plays a crucial role for the differential scattering cross section $d\sigma/d\Omega$ and total scattering cross section σ. The scattering wavefunction has to be properly symmetrized or antisymmetrized if the two colliding particles are identical bosons or identical fermions, respectively. This can be achieved by noting that $f(\theta, k) = -\varepsilon f(\pi - \theta, k)$ where $\varepsilon = +1$ for bosons and $\varepsilon = -1$ for fermions. By integrating the differential cross section $d\sigma/d\Omega = |f(\theta, k) + \varepsilon f(\pi - \theta, k)|^2$ over the solid angle Ω one can express the partial scattering cross section through

$$\sigma_l(k) = \frac{4\pi}{k^2}(2l+1)\sin^2\delta_l, \tag{2.5}$$

from which the total cross section follows as $\sigma(k) = \sum_{l=0}^{\infty}\sigma_l$. Due to the imposed symmetry on the scattering wavefunction, $\sigma_l = 0$ if l is odd or even for identical bosons or identical fermions, respectively.

For scattering processes presented in this thesis, though, only scattering in the lowest partial wave $l = 0$, and consequently σ_0, are relevant, since the experimentally employed temperatures are well below the centrifugal barriers originating from higher partial waves with $l > 0$ (see discussion in Sect. 2.2.2). Thus one introduces the s-wave scattering length a through the expression

$$a = \lim_{k\to 0}\frac{\tan\left[\delta_0(k)\right]}{k}, \tag{2.6}$$

as the only parameter characterizing an ultracold collision. Employing this definition one finally arrives at the following scattering cross section

$$\sigma(k) = \begin{cases} \frac{4\pi a^2}{1+k^2a^2} & \text{for distinguishable particles,} \\ 0 & \text{for identical fermions,} \\ \frac{8\pi a^2}{1+k^2a^2} & \text{for identical bosons.} \end{cases} \tag{2.7}$$

This result already demonstrates one of the most fundamental consequences of quantum statistics on ultracold scattering, namely, that identical fermions do not interact with each other through s-wave collisions. It will become important later in the analysis of the three-body recombination spectra in Sect. 3.4.

In ultracold gas experiments with neutral atoms the interaction potential $U(\vec{r})$ typically corresponds to the Born-Oppenheimer molecular potential, which is a spherically isotropic short-range potential. An interesting exclusion is the dipole-dipole interaction that gives rise to anisotropic potentials, and scattering that in-

volves more partial waves than just the s-wave ($l = 0$). See, for example [Aikawa et al., 2012, 2014; Stellmer et al., 2009; Stuhler et al., 2005; Lu et al., 2012].

2.2.2 Scattering in external magnetic field

The ability to control the s-wave scattering length in ultracold neutral atomic and molecular gases that are subjected to external magnetic fields originates from the internal structure of the scattering particles. It gives rise to scattering resonances, called Fano-Feshbach resonances, in honor to Herman Feshbach and Ugo Fano who introduced the concept of energy dependent resonances due to coupling between a bound state and a continuum scattering state of two particles in nuclear physics [Feshbach, 1958] and atomic physics [Fano, 1961], respectively. The modification of this coupling by the externally applied magnetic field results in a change of the value of the scattering length and consequently interaction strength. A thorough review of Feshbach resonances in ultracold gases and the control of the scattering length is given in Refs. [Chin et al., 2010; Köhler et al., 2006]. Here we summarize the main results.

Consider the Schrödinger equation (2.1) and its Hamiltonian, which we now extended with an interaction term $H_{int} = H_{hf} + H_Z + H_{dd}$ to describe a binary collision in the presence of an external magnetic field [Stoof et al., 1988]:

$$H = T + U + H_{int}. \tag{2.8}$$

In addition to the kinetic energy term $T = -\hbar^2\vec{\nabla}^2/(2\mu)$ and potential U the Hamiltonian now contains the hyperfine energy operator

$$H_{hf} = \sum_{\xi=A,B} a_{hfs}^{(\xi)}(\vec{r})\vec{s_\xi}\cdot\vec{i_\xi} \tag{2.9}$$

with the electronic and nuclear spin operators $\vec{s_\xi}$ and $\vec{i_\xi}$, where the index ξ and the two terms in the sum correspond to the two atoms A and B. Here we consider the electronic ground state for alkali atoms ${}^2S_{1/2}$ with $l_\xi = 0$ and $s_\xi = 1/2$, as appropriate for the experiments presented in this thesis, and hence $\vec{j_\xi} = \vec{s_\xi}$. The separation dependent hyperfine constants $a_{hfs}^{(\xi)}(\vec{r})$ account for electronic distortions of one atom by the other at small separations [Strauss et al., 2010], and asymptotically approach the atomic hyperfine constant A_{hfs}^{ξ} for $r \to \infty$. The Zeeman interaction is given by

$$H_Z = \frac{\mu_B}{\hbar}\sum_{\xi=A,B}\left(g_{s,\xi}\vec{s_\xi} + g_{i,\xi}\vec{i_\xi} + g_{l,\xi}\vec{l_\xi}\right)\cdot\vec{B}, \tag{2.10}$$

where the magnetic field $\vec{B}$ couples to the electron spin, electron orbital, and nuclear magnetic dipole moments that are quantified with $g_{s,\xi}$, $g_{l,\xi}$, and $g_{i,\xi}$ gyromagnetic

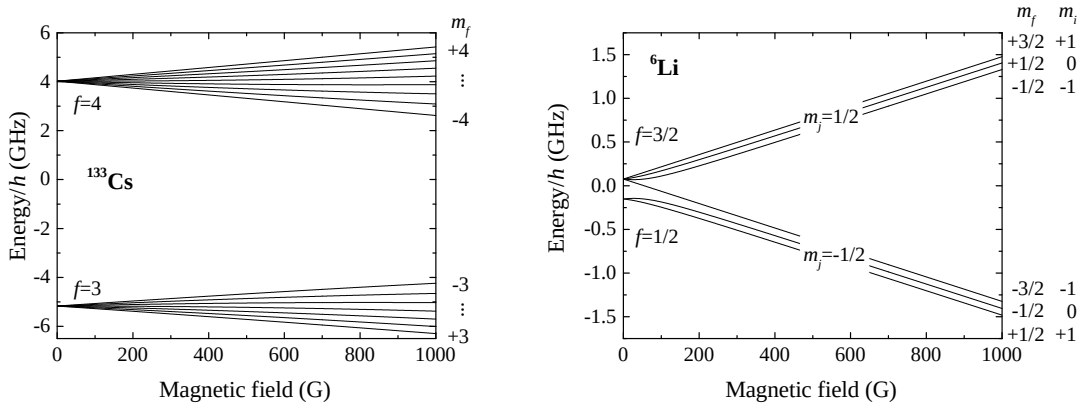

Figure 2.2: Atomic energy levels of ^{133}Cs and ^{6}Li atoms as function of applied magnetic field in the electronic ground state. f denotes the total angular momentum of the atom and m_f, m_j, and m_i are the magnetic total, electron spin, and nuclear spin quantum numbers, respectively.

ratios, respectively. In general, the interaction Hamiltonian contains also magnetic dipole-dipole couplings between the different spin operators that are described by the term H_{dd}. These contributions, however, are small and present only in p-wave resonances, since an anisotropic interaction potential is required to generate experimentally observable energy shifts [Ticknor et al., 2004]. The work presented in this thesis deals exclusively with s-wave resonances, therefore, from here on, we neglect the H_{dd} term in the interaction Hamiltonian. Its effective form and explicit application for the Li-Cs system can be found elsewhere [Pires, 2014].

Fig. 2.2 shows the calculated atomic hyperfine energy levels as a function of the applied magnetic field for ground state ^{133}Cs and ^{6}Li atoms that corresponds to the eigenenergies of H_{int} (see Eq. (2.8)). The hyperfine energy levels are labeled by their total angular momentum $f = \left|\vec{j} + \vec{i}\right|$ and its projection m_f on the quantization axis. For high magnetic field strengths the Zeeman energy becomes large in comparison to the hyperfine splitting, and consequently f is not a good quantum number anymore, while m_f is still a good one due to rotational symmetry around the magnetic field axis that we choose as the quantization axis. The individual quantum numbers allows one to define a scattering channel with the quantum number $M_F = m_{f,A} + m_{f,B}$ that is characterized by the state $|\zeta\rangle = A\,|f_A, m_{f,A}\rangle \oplus B\,|f_B, m_{f,B}\rangle$, also called scattering channel, and asymptotically corresponds to two noninteracting atoms in free space described by the combination $f_\xi, m_{f,\xi}$ for each atom. The scattering channels can be separated into two groups. A channel is called open or closed if the initial energy E of the scattering atoms is larger or smaller than the asymptotic channel energy, corresponding to the sum of the internal energies of two atoms in the limit $r \to \infty$.

The scattering channels with different M_F are diagonal in the interaction Hamiltonian H_{int} representation. Once additional terms are introduced in the Hamiltonian, the scattering channels can be coupled. The interatomic potential $U(\vec{r})$ is an important example, since exactly this coupling is responsible for the existence of Feshbach resonances (see Sect. 2.2.3). However, the scattering channels can be coupled also through other mechanisms, for which oscillating magnetic fields is an prime example. This will become important for the discussion of the radio-frequency association of Feshbach dimers in Sect. 2.4.

In this work we experimentally employ the energetically lowest Cs spin state with $f = +3$ and $m_f = +3$, and the two energetically lowest Li spin states with $f = +1/2$ and $m_f = +1/2; -1/2$ (see Fig. 2.2). For these energy levels we define the appropriate scattering channels by

$$\begin{aligned} |\alpha\rangle &= \mathrm{Li}\left|\frac{1}{2}, +\frac{1}{2}\right\rangle \oplus \mathrm{Cs}\,|3, +3\rangle\,, \\ |\beta\rangle &= \mathrm{Li}\left|\frac{1}{2}, -\frac{1}{2}\right\rangle \oplus \mathrm{Cs}\,|3, +3\rangle\,. \end{aligned} \tag{2.11}$$

The projections M_F for channels $|\alpha\rangle$ and $|\beta\rangle$ yields values $M_F^{(\alpha)} = 7/2$ and $M_F^{(\beta)} = 5/2$, respectively. The kinetic energy in the experiments presented here is on the order of ~ 10 kHz[1] and the typical energy separation between consecutive scattering channels is on the order of tens of MHz. Thus, if the system is prepared in $|\alpha\rangle$ or $|\beta\rangle$ channel, there is one or two open channels, respectively.

Now we turn our attention to the interatomic potential $U(\vec{r})$, specifically, we consider spherically isotropic potentials, which allows one to drop the vector notion. For interactions between two alkali atoms it corresponds to the Born-Oppenheimer molecular potentials, which are shown in the Fig. 2.3(a) for the LiCs dimer ground electronic state. The two potential curves differ by the orientation of the valence electron spins, as they can arrange themselves in either singlet ($S = 0$) or triplet ($S = 1$) configuration, where the total electron spin $S = s_A + s_B$. This leads to a significant difference between the molecular binding energies for the two arrangements, and the total potential $U(r) = P_0U_0 + P_1U_1$ has to be constructed as a superposition of the singlet and triplet contributions by projection operators P_0 and P_1, respectively.

By transforming the Schrödinger equation (2.1) into the spherical coordinate system an effective rotational potential barrier emerges, which adds to the radial potential energy seen by the atoms (see Fig. 2.3(b)). Its amplitude U_{rot} can be

[1] If expressed in the appropriate units 1 μK is equivalent to 20.8 kHz.

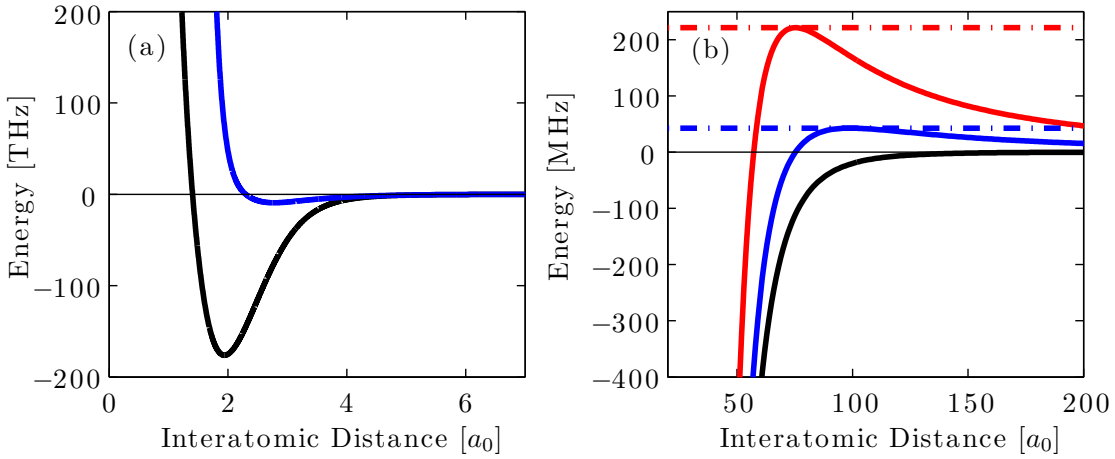

Figure 2.3: Born-Oppenheimer molecular potentials of the LiCs electronic ground state. (a) Full singlet (black) and triplet (blue) potentials as calculated from a coupled channels calculation. (b) Long range van der Waals potentials with $l = 0$ (black), $l = 1$ (blue), and $l = 2$ (red) centrifugal terms. The dash-dotted lines illustrate the rotational barrier; see Eq. (2.12). Figure adapted from [Pires, 2014].

expressed as

$$U_{rot} = \frac{1}{\sqrt{2C_6}} \left(\frac{\hbar^2 l(l+1)}{3\mu} \right)^{3/2} \tag{2.12}$$

that depends on the particular partial wave l, in which the two particles are colliding. It is on the order of 2 mK and 11 mK for Li-Cs p-wave ($l = 1$) and d-wave ($l = 2$) collisions, respectively. The experimentally employed temperatures are ranging from 1 μK down to a couple of tens of nK, thus effectively screening the particles colliding in higher partial waves from exploring the short internuclear distances where the interspecies potential $U(r)$ is significant. This confirms that the use of the s-wave scattering length a, as introduced in Sect. 2.2.1, is well suited for the description of the entire scattering process.

2.2.3 Interactions and weakly-bound dimers close to a Feshbach resonance

A Feshbach resonance is caused if the energy of an atom pair that is scattering in the entrance scattering channel matches the one of a bound state that is supported by a closed channel, and a coupling exists between them. If the magnetic moments of the involved channels are different, the energy difference can be controlled via an external magnetic field. This gives rise to magnetic field dependent coupling and, consequently, scattering length. Scattering theory provides an elegant way of calculating the transition amplitudes between the involved open channels. In order

to illustrate the basic concepts we shortly recapture the two-channel scenario that was introduced by [Moerdijk et al., 1995] and elaborated on by [Timmermans et al., 1999; Mies and Raoult, 2000; Góral et al., 2004; Köhler et al., 2006].

The starting point is the Schrödinger equation and Hamiltonian from Eq. (2.8), which we project onto the open and closed channel subspaces via the projection operators $\hat{P}$ and $\hat{Q}$, respectively. One obtains a set of coupled equations

$$(E - H_{PP})\Psi_P = H_{PQ}\Psi_Q \tag{2.13}$$
$$(E - H_{QQ})\Psi_Q = H_{QP}\Psi_P, \tag{2.14}$$

where the projection onto the respective open and closed subspaces is denoted by subscripts P and Q. Here $H_{\hat{i}\hat{j}} = \hat{i}H\hat{j}$, and $\Psi_{\hat{i}} = \hat{i}\Psi$ and the total scattering wavefunction

$$\Psi = \sum_{\zeta} \psi_\zeta(\vec{r}) \left|\zeta\right\rangle, \tag{2.15}$$

which is expanded over the basis of the scattering channels $|\zeta\rangle$ and r dependent coefficients $\psi_\zeta(\vec{r})$. We can formally solve Eq. (2.14) by Green's operator $1/(E - H_{QQ} + i0)$, which yields

$$\Psi_Q = \frac{1}{E - H_{QQ} + i0} H_{QP}\Psi_P. \tag{2.16}$$

Substituting this equation back into Eq. (2.13) gives an effective expression for the scattering process in the open channel that reads

$$\left(H_{PP} + H_{PQ}\frac{1}{E - H_{QQ} + i0}H_{QP}\right)\Psi_P = E\Psi_P. \tag{2.17}$$

This Schrödinger equation illustrates the basic mechanism behind a Feshbach resonance. The second term in the effective Hamiltonian can be interpreted as a transition from open P-subspace to closed Q-subspace, followed by propagation in Q-subspace, and completed by re-emission back into P-subspace. The phase shift acquired by the wavefunction during this propagation is reflected in the modification of the scattering length a, which was introduced in Eq. (2.6). The first term H_{PP} is present also if no closed channels exist, and hence it corresponds to a pure scattering process in the open channel subspace P, where its primary role is giving rise to the background scattering length a_{bg}. The couplings H_{PQ} and H_{QP} are determined by the Coulomb interaction, to which the main contribution arises from the electron exchange that is proportional to the energy difference between the singlet and triplet molecular potentials.

The object that characterizes the collision process in a multichannel system is

the unitary scattering matrix S. The matrix elements S_{ji} quantifies the transition amplitudes from incoming channel i into the outgoing channel j. For a single channel the S-matrix element is related to the scattering phase shift $\delta(k)$ via relation $S(k) = e^{2i\delta(k)}$, and the elastic cross section can be expressed as $\sigma_\zeta = g_\zeta \pi/k^2 \left|1 - S_{\zeta\zeta}\right|^2$, where g_ζ characterizes the quantum statistics of the colliding particles [Chin et al., 2010]. Therefore, we investigate the behavior of the matrix element S_{ii} in case when the total energy E is close to a discrete bound state energy ε_B and there is only one open channel. It requires spacing between the discrete energy levels of H_{QQ} that is much larger than any of the near-threshold couplings and energy distributions, which is the case for all of our experiments.

This is known as the single resonance, two-channel approach [Moerdijk et al., 1995; Timmermans et al., 1999; Mies and Raoult, 2000; Köhler et al., 2006]. For an ultracold mixture prepared in the energetically lowest spin states the single energetically allowed outgoing channel is also the incoming channel. The S matrix reduces to a single element, which can be written as [Moerdijk et al., 1995]

$$S = S_{bg}\left(1 - \frac{i\Gamma(E)}{E - \varepsilon_B - \mathcal{A}(E)}\right), \tag{2.18}$$

where $\Gamma = 2\pi \left|\langle\psi_B| H_{PQ} |\zeta^+\rangle\right|^2$ describes the coupling between the corresponding molecular eigenstate $|\psi_B\rangle$ and the incoming part of the scattering state, which is denoted by $|\zeta^+\rangle$, and ε_B denotes the energy of the molecular state (bare energy) in the closed subspace Q. S_{bg} describes the scattering in the open P-channel, and $\mathcal{A}(E)$ is the complex energy shift that is expressed by

$$\mathcal{A}(E) = \langle\psi_B| H_{QP} \frac{1}{E - H_{PP} + i0} H_{PQ} |\psi_B\rangle, \tag{2.19}$$

decomposed as $\mathcal{A}(E) = \Delta(E) + i\Gamma(E)/2$ into a real part $\Delta(E)$ and an imaginary part $\Gamma(E)$. For energies above the scattering threshold ($E > 0$), the molecular state with the bare energy ε_B can be interpreted as a quasi-bound state in the Q-subspace that is shifted by $\Delta(E)$ due to the couplings to the P-subspace, and has a width $\Gamma(E)$. For negative energies ($E < 0$) the energy shift $\mathcal{A}(E)$ is real, and hence it describes an actual energy shift of the bare molecular state due to coupling to the scattering channel.

In our experiments, the closed and open scattering channels consist of a pair of atoms in different hyperfine states, so the two channels exhibit different magnetic moments. This leads to magnetic field dependent differential energy shifts between ε_B, E, and $\mathcal{A}(E)$. Thus, if a bound state in the closed channel is close enough to the scattering threshold, one can bring them into degeneracy by changing the external magnetic field. Therefore, we consider ultracold scattering where only the s-waves

contribute, and the relative collision energy $\varepsilon_r = E - E_{th} \sim k^2$, where E_{th} is the threshold energy. Noting that $S = e^{-2ika}$ and $S^{bg} = e^{-2ika_{bg}}$, the magnetic field dependence of the scattering length can be expressed as

$$a(B) = a_{bg} - \frac{\pi\hbar m}{\epsilon_{res}}\Gamma(B), \tag{2.20}$$

where $\epsilon_{res} = \varepsilon_B(B) + \Delta(B)$ in the zero-energy limit. By introducing the explicit B-dependence of $\epsilon_{res}(B) = (\mu_P - \mu_Q)(B - B_{FR})$ on the magnetic moments μ_P and μ_Q of an asymptotically separated pair of atoms in the scattering channel and the molecular state, respectively, this equation recovers the well-known dispersive expression for Feshbach resonances

$$a(B) = a_{bg}\left(1 - \frac{\Delta B}{B - B_{FR}}\right), \tag{2.21}$$

which is parametrized by the resonance pole position B_{FR} and width ΔB, quantifying the coupling strength between the P and Q subspaces. This behavior is shown in Fig. 2.4 for a generic Feshbach resonance. In general, a_{bg} and ΔB contains a weak dependence on B, however for near-resonant scattering close to the pole of a Feshbach resonance this dependency is negligible in comparison to the resonant behavior.

According to Eqs. (2.18), the energy of the molecular state in the vicinity of the pole of the Feshbach is given by

$$E_b = \varepsilon_B + \mathcal{A}(E_b), \tag{2.22}$$

which consists of the bare energy ε_B of the closed subspace Q that is "dressed" by the coupling to the scattering channel in the open subspace P. For energies below the scattering threshold the expression reduces to $E_b = \varepsilon_B + \Delta(E_b)$. In the limit $E_b \to 0$ and $B \to B_{FR}$, the real part of the complex energy shift vanishes, i.e. $\Delta(0) \to 0$, which implies that the properties of the near-resonant molecular state is almost solely determined by the properties of the scattering state, and consequently a. Therefore, this regime and the molecular state are usually referred to as universal regime. A rigorous derivation of this relation is given in [Góral et al., 2004; Köhler et al., 2006], and relies upon an explicit determination of the energy dependence of the complex energy shift $\mathcal{A}(E_b)$. Here, we give only the final result [Köhler et al., 2006]

$$E_b(B) = \frac{1}{2m}\left(\frac{\hbar}{a_{bg}}\frac{B - B_{FR}}{\Delta B}\right)^2, \tag{2.23}$$

which is also shown in Fig. 2.4. In the limit of large scattering lengths $a \gg a_{bg}$ and in combination with Eq. (2.21) it reduces to the well-known universal formula for

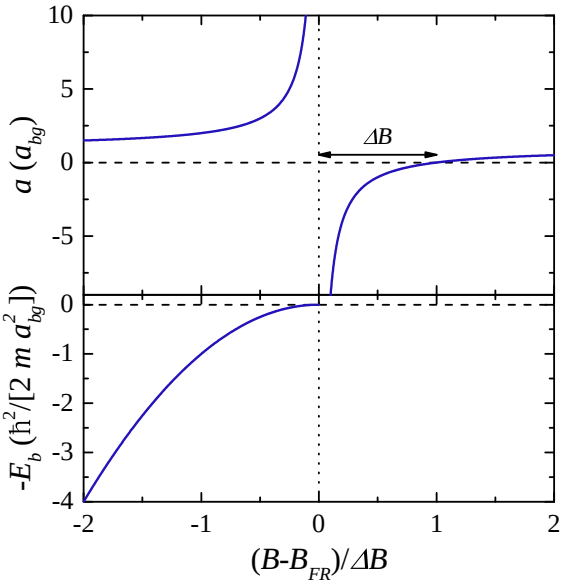

Figure 2.4: Structure of a generic Feshbach resonance. The upper panel shows the scattering length given by Eq. (2.21) with the zero-crossing located one resonance width ΔB away from the pole position B_{FR}. The lower panel depicts the universal energy dependence of the "dressed" molecular state, given by Eq. (2.23).

the bound-state energy of a weakly bound dimer

$$E_b = \frac{\hbar}{2ma^2}. \tag{2.24}$$

2.3 Producing and probing ultracold Li-Cs mixtures

In this section we discuss our approach for the preparation of an ultracold Li-Cs mixture, which is used to obtain ensembles of ultracold Li and Cs atoms in a specific scattering channel with temperatures ranging from around 500 nK down to approximately 250 nK. Even lower temperatures can be reached in this setting for single species, evidenced by the observation of Bose-Einstein condensation of Cs atoms and Li_2 molecules during this thesis. Details on the experimental procedure for this can be found in Refs. [Pires, 2014; Arias, 2014; Repp, 2013]. However, with the approach presented in this chapter, at such low temperatures the gas clouds spatially separate because of the high mass imbalance, which is causing significantly different gravitational potentials for each of the species. This can be overcome by extending the setup that is used for the generation of external trapping potentials, which will be discussed in Sect. 3.3.

Here, we exclusively focus on the mixture preparation at around 400 nK, which is

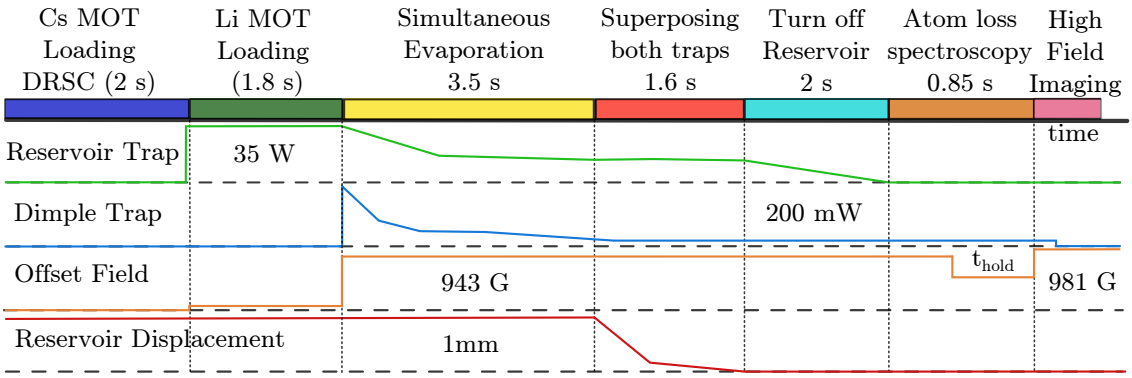

Figure 2.5: Experimental sequence for the preparation of Li-Cs mixture near the 843 G Feshbach resonace in the scattering channel $|\alpha\rangle$. This sequence represents the general cooling and mixing approach of the two atomic species that is used in this chapter and for the observation of the Efimov resonances at 450 nK temperatures. The experiments on radio-frequency association of LiCs dimers follow the same approach with slightly different magnetic field values for the offset field, which are given in the text. Figure adapted from [Pires, 2014].

largely unaffected by the gravitational sag. The experimental apparatus and cooling and imaging techniques have been already presented in great detail in Refs. [Pires, 2014; Repp, 2013; Arias, 2014; Häfner, 2013; Schönhals, 2013; Heck, 2012]. Therefore, we start by introducing the experimental cooling sequence that was employed in the experiments on weakly bound LiCs molecules and, in part, the observation of $LiCs_2$ Efimov resonances in Sect. 2.3.1. Since magnetic and radio-frequency fields play a crucial role not only in the two-body sector, but also for three-body physics, we shortly describe their most important characteristics, especially the determination of the systematic errors in Sect. 2.3.2 and 2.3.3 for homogenous offset and oscillating (with radio- and micro-wave frequency) magnetic fields, respectively.

2.3.1 Experimental procedure for the sample preparation at 400 nK

The overview of our experimental preparation sequence is given in Fig. 2.5. We start by loading a Cs MOT for typically 2 s, followed by two degenerate Raman sideband cooling [Vuletić et al., 1998; Kerman et al., 2000; Treutlein et al., 2001] cycles of approximately 15 ms that spin polarize the atoms to about 90% in the energetically lowest Zeeman state $\mathrm{Cs}|f = 3, m_f = +3\rangle$. The second cycle is performed already with the reservoir trap turned on at 35 W. As the atoms in the wings of the trap are heated due to the conversion of higher potential into kinetic energy, it is beneficial to apply the second pulse after a short propagation period in the optical dipole

potential, during which more of the atoms have reached the center of the trap[2]. In this way an approximate two-fold increase in final phase-space density in the reservoir trap is achieved. At this point we apply an offset magnetic field of ~ 4.5 G to preserve the spin polarization by providing a quantization axis.

The sequence is continued by a spatially separated loading of a Li MOT for 1.8 to 2.5 seconds. After a short compression phase the Li atoms are loaded into the dimple trap, which is ~ 1 mm displaced from the reservoir trap in which the Cs is being held. At the end of the MOT phase we apply a short optical pumping pulse that transfers all of the Li atoms into the $f = 1/2$ hyperfine state. Since we have not applied any spin polarization techniques so far, Li atoms populate both of the Zeeman sublevels, namely, Li$|f = 1/2, m_f = +1/2\rangle$ and Li$|f = 1/2, m_f = -1/2\rangle$.

At this point we set the homogenous offset field to $B_{evap} \approx 920$ G to ensure rapid thermalization of both species, and perform simultaneous forced evaporation with still spatially separated reservoir and dimple traps. After approximately 3.5 s long evaporation ramp, we superimpose both traps with a piezo-driven mirror within one fast (600 ms) and one slow ramp (1 s) to ensure approximately adiabatic merging. While keeping the power in the dimple trap constant, we turn off the reservoir trap in a 2 s long ramp, which transfers a part of the Cs atoms into the dimple trap. As the potential depth decreases the temperature of the gas in the reservoir trap is further reduced. Because these atoms are still in thermal contact with the ones in the dimple trap due to collisions, the thermal energy can be exchanged, which leads to cooling in the dimple trap as well, and equal temperature in both of the traps. Additionally, the local increase in the trapping frequencies leads to increased phase space density in the dimple trap, which is often in the literature refereed to as the *dimple trick* [Pinkse et al., 1997; Hammes et al., 2002; Weber, 2003].

During the last ramp of the reservoir trap the atom clouds already overlap. The ramp is performed at $B_{mix} \approx 875$ G to minimize three-body losses of Cs atoms while still ensuring high enough scattering cross section for intra and interspecies collisions. This value was experimentally found to optimize the remaining number of atoms in all the three different spin states of both species after the reservoir trap had been ramped off.

The mixed sample in the dimple trap now consists of Cs atoms in spin state $|3, +3\rangle$ and Li atoms in spin states $|1/2, +1, 2\rangle$ and $|1/2, -1/2\rangle$. The final scattering channel $|\alpha\rangle$ or $|\beta\rangle$ (see Eq. (2.11) for the definition of the scattering channels) is selected by shining in a laser light pulse that is resonant with the D2 transition of Li$|1/2, -1/2\rangle$ or Li$|1/2, +1/2\rangle$ spin states at the given magnetic field, thus removing the unnecessary spin component. After a slight re-compression of the dimple trap in 500 ms, that stops the residual evaporation, but increases the final temperature to

[2]Note that in a harmonic trap the oscillation period is the same, independent at which potential energy the oscillation is started.

about 450 nK, we are left with about $4{\times}10^4$ Li and $4{\times}10^4$ Cs atoms in the necessary scattering channel. At these conditions we measure the secular trapping frequencies f_x, f_y, f_z of 11 Hz, 114 Hz, 123 Hz (33 Hz, 275 Hz, 308 Hz) for Cs (Li) atoms, where the external magnetic field is parallel to the z axis. This procedure is discussed in detail in Refs. [Repp, 2013; Häfner, 2013; Pires, 2014].

2.3.2 Homogenous magnetic fields

The magnetic fields are of fundamental importance for all of the measurements performed in this thesis. As explained in Sect. 2.2, the use of magnetic Feshbach resonances allows one to change the magnitude and sign of the scattering length, which is an essential ingredient for the observation of Efimov physics. Furthermore, the energy of the weakly bound molecular state that gives rise to the scattering resonance also tunes with the applied magnetic field (see Sect. 2.2.3). In fact, exactly this connection allows one to infer the structure of the scattering resonance and its relation to the magnetic field, as presented in Sect. 2.4.

Here we explain the main characteristics of our setup for generating homogenous magnetic fields, which are used to control and tune the properties of ultracold atomic samples in all of the measurements that are presented in this work. In the next paragraphs we highlight two of the most relevant magnetic field properties for the performed experiments: the long-term stability and the switching speed. We do not discuss the technical setup, since it has already been described in detail elsewhere [Pires, 2014; Repp, 2013].

The stability of magnetic fields that is on the order of a couple of mG is crucial. To illustrate this we consider the behavior of scattering length in the vicinity of a Feshbach resonance, given by Eq. (2.21). As the uncertainty in the magnetic field increases, the ability to resolve scattering length close to the pole of the resonance diminishes. The maximum value that can be still resolved can be estimated employing Gaussian error propagation. The uncertainty of scattering length δa, which is caused by magnetic field uncertainty δB, is given by

$$\delta a = \frac{a_{bg}\Delta B}{(B - B_{FR})^2}\delta B. \tag{2.25}$$

By loosely defining the theoretical resolution limit at the magnetic field value, for which $\delta a(B) = a(B)$, Eq. (2.25) yields $\delta a_r \approx a_{bg}\Delta B/\delta B$, for $(B - B_{FR}) \ll \Delta B$. We can apply this estimation for the case of Li-Cs Feshbach resonances by choosing a hypothetical resonance that approximately mimics Li-Cs ones. Using width $\Delta B =$ 60 G and $a_{bg} = 30\ a_0$ we obtain $\delta a_r \approx 10^5\ a_0$ for magnetic field uncertainty $\delta B =$ 16 mG, which is the value that is achieved with the experimental setup. Although δa_r quantifies the largest scattering length that can be distinguished from the pole,

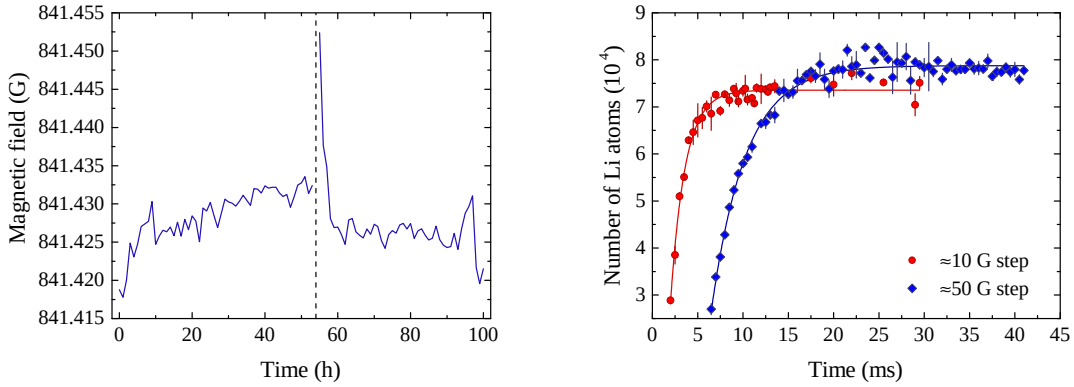

Figure 2.6: Long-term stability (left panel) and step response (right panel) of magnetic fields. In the left panel, each data point is obtained from an independent determination of magnetic field by rf-spectroscopy of Li (see Sect. 2.3.3). The vertical dashed line shows the time when the execution of the experimental sequence was paused and resumed after several hours. The solid lines depict fits of an exponential growth equation to the data, with time constants 1.6 ms and 3.8 ms for 10 G and 50 G step size, respectively.

in practical applications the resolution will be lower, since, instead of the pole, one is interested in resolving resonant features close to it, for which more than one point is necessary.

The magnetic field uncertainty for the performed experiments originates from the following sources:

- Calibration of magnetic fields. The calibration of magnetic fields is typically performed over 5 to 6 uniformly distributed values within the magnetic field range at which the measurements are taken. The resulting dependence of the magnetic field values on the control parameter is fitted with a linear function, which is later used to infer the magnetic field value for the given control parameter. This procedure introduces an magnetic field uncertainty of 9 mG. For calibration we use radio-frequency spectroscopy to drive transitions between Li hyperfine states, which is desribed in detail in Sect. 2.3.3.

- Long-term stability. The magnetic field calibration is performed once every several days, during which the absolute value of the field with respect to the control parameter may vary. To characterize this variation an extended series of measurements was taken, which is depicted in the left panel of Fig. 2.6. After the experimental setup has thermalized and reached a steady state, which may take a little bit longer than a day, if initialized from completely "cold" state (not shown in the figure), the fluctuations of the absolute value of magnetic field stay within ≈10 mG. In fact, the maximum standard deviation from the

mean during the course of a 24 hour period is 8 mG, which we use as the uncertainty quantifying the long-term drifts. To estimate the time that is necessary for the experimental system to reach the steady state after a short break, we stopped the execution of the experimental sequence (vertical dashed line in Fig. 2.6 (left panel)) and resumed the operation after several hours. Within three to four hours the magnetic field stabilizes to the previous level.

- Experimental sequence length. The steady state conditions may depend on the length of the experimental sequence. For example, due to the generated ohmic heat that is deposited in the magnetic field coils their geometry may change, which would lead to a different absolute value of the applied field. We quantify this uncertainty by comparing magnetic field calibration immediately after the sample preparation (see Sect. 2.3.1) and after 3000 ms. The difference yields 8 mG, which are included in the total uncertainty.

- Residual magnetic field gradient. Since the magnetic coil setup deviates from an exact Helmholtz configuration, the final field in which the atoms are located may exhibit rest-gradient [Repp, 2013; Pires, 2014]. The upper limit of this uncertainty is estimated from the linewidth of the Li electron spin flip transition as described in Sect. 2.3.3, yielding 8 mG.

We assume that these sources are uncorrelated and use simple addition of squares to extract the total systematic uncertainty, which results in 16 mG.

An important component of any experimental sequence is the switching of magnetic fields, especially the time that is necessary for the field to stabilize to the new value after the control parameter has been changed. Since the performed experiments rely on extracting different observables as a function of magnetic field, the short term stability of the field is critical, therefore we optimize the experimental sequence in such a way that the measurements are taken only after the field has stabilized.

In order to determine the necessary wait time, we recorded the step response of our magnetic coil setup, which is depicted in the right panel of Fig. 2.6. Here, a sample of Li atoms in $|1/2, +1/2\rangle$ spin state was prepared and the magnetic field was suddenly switched to 870 G. Immediately after setting the new value a 190 μs long π-pulse was applied that, in case of no additional Zeeman shifts, would transfer all of Li atoms into $|1/2, -1/2\rangle$ spin state, which was being imaged. Depending on the amplitude of the magnetic field step size, an fit of the exponential growth model $N(t) = N_0 + C(1 - e^{-t/\tau})$ to the data yields time constant $\tau = 1.6$ ms or 3.8 ms for 10 G or 50 G step size, respectively, where $N(t)$ denotes the number of atoms, N_0 stands for the initial number of atoms, and C is an amplitude constant. Typically we start recording data after a wait time of approximately five to ten time constants.

2.3.3 Radio- and microwave frequency fields

In the context of this thesis, microwave (mw) and radio-frequency (rf) spectroscopy is used to measure the energy difference between two energy eigenstates of a system consisting of atoms or molecules that are confined in an external potential. The system is exposed to a mw or rf pulse that induces population transfer from one eigenstate into another. Since the experimentally employed samples are very dilute, this process is well described by a two-level system, which allows one to drive Rabi oscillations between the eigenstates or perform rapid adiabatic passages in order to prepare the required scattering channel. Additionally, from the energy of the applied photon one can infer the energy difference between the two eigenstates of the system. Since typical linewidths of these transitions are very narrow, these techniques are well suited for precision measurements of such energy differences in ultracold gas experiments.

In our measurements three different transitions are employed (for Breit-Rabi energy level diagrams and corresponding quantum numbers see Fig. 2.2):

(i) Nuclear spin flip transition between Li$|1/2, +1/2\rangle$ and Li$|1/2, -1/2\rangle$ Zeeman sublevels with $\Delta m_i = 1$ (also referred as free-free transition in the context of LiCs dimer association, see Sect. 2.4),

(ii) Electron spin flip transitions from Li$|1/2, +1/2\rangle$ to Li$|3/2, 3/2\rangle$, and from Li$|1/2, -1/2\rangle$ to Li$|3/2, 1/2\rangle$ Zeeman sublevels with $\Delta m_j = 1$,

(iii) Nuclear spin flip transitions starting in the Li-Cs scattering channels $|\alpha\rangle$ and $|\beta\rangle$ (see Eq. (2.11)), and the corresponding molecular state $\left|\psi_B^\beta\right\rangle$ and $|\psi_B^\alpha\rangle$, respectively, with $\Delta m_i = 1$.

Here, Δm_i and Δm_j indicates selection rules of magnetic quantum numbers for nuclear and electron spin flip transitions, respectively. For type (i) and (iii) transitions the difference between the energy eigenstates is $\sim h \times 76$ MHz in the magnetic field range from 800 G to 900 G, hence they are referred to as rf-transitions. Type (ii) transitions are referred to as mw-transitions because they require driving fields at frequencies that are around 2 GHz.

In what follows, we shortly discuss our application of type (i) and (ii) transitions for the characterization of the magnetic field setup and entrance scattering channel preparation. Type (iii) transitions in this work are used for weakly bound LiCs dimer production and their rf-spectroscopy, and are described in more detail in Sect. 2.4.

A spectrum of a type (i) transition at 888.535 G magnetic field is shown in the left panel of Fig. 2.7. We employ the resonance frequency of the transition in conjunction with the Breit-Rabi formula to calibrate the absolute magnetic field

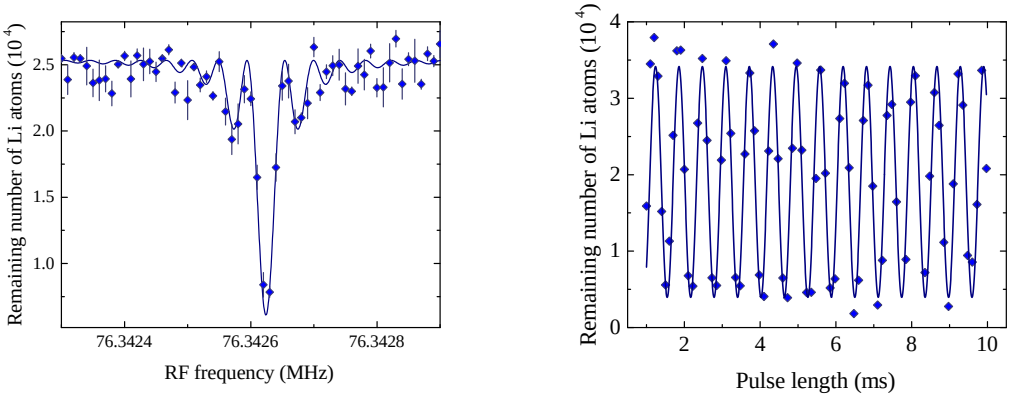

Figure 2.7: Radio-frequency spectroscopy of Li$|1/2, +1/2\rangle$ to Li$|1/2, -1/2\rangle$ transition. Left panel, spectra of the transition with an rf-pulse length of 25 ms. The solid line shows the fit of Eq. (2.26) to the data. The fit yields a resonance frequency of $\omega_{ij}/(2\pi) = 76.34262$ MHz, which corresponds to a magnetic field of 888.535 G, and a Rabi frequency $\Omega_0 = 2\pi \times 0.265$ Hz. Error bars correspond to one standard error. Right panel, Rabi oscillations of the same transition at a magnetic field of 841.430 G, and a Rabi frequency of $2\pi \times 1.6$ kHz.

strength, as described in Sect. 2.3.2. In order to do this, we fit the data points with the lineshape function, given by

$$P(\omega, t) = \left(\frac{\Omega_0}{\Omega_{\text{eff}}(\omega)}\right)^2 \sin^2\left(\frac{\Omega_{\text{eff}}(\omega)}{2}t\right), \tag{2.26}$$

where Ω_0 denotes the Rabi frequency on the resonance, and $\Omega_{\text{eff}} = \sqrt{\Omega_0^2 + \delta^2}$ is the effective Rabi frequency with detuning $\delta = \omega_{ij} - \omega$. Here, ω_{ij} stands for the resonance frequency between the energy levels i and j and ω is the frequency of the driving field. A typical statistical error of the resonance frequency determination for a single spectrum is around a couple of mHz that corresponds to roughly 1 mG, if expressed in magnetic field uncertainty. This is at least an order of magnitude better than our total systematic error.

By recording the remaining number of Li atoms in the Li$|1/2, -1/2\rangle$ spin state as a function of the applied rf-pulse length, we observe Rabi oscillations, which are depicted in the right panel of Fig. 2.7. During the first 10 ms of the oscillations we do not observe any significant decay of decoherence, however longer measurements indicate time constants of around 200 ms, probably limited by dephasing through magnetic field inhomogeneities. At full power the setup can deliver Rabi frequencies of up to $2\pi \times 3.8$ kHz in the magnetic field region from 800 G to 900 G.

We use rf fields not only to perform high-precision spectroscopy, but also to gain greater control over the initial state preparation. By using π or $\pi/2$ pulses

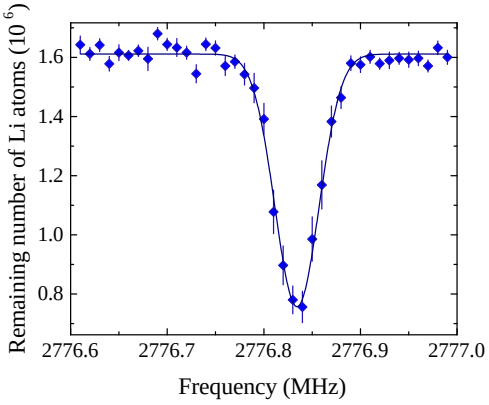

Figure 2.8: Atom-loss spectrum of the microwave transition between Li$|1/2,-1/2\rangle$ and Li$|3/2,+3/2\rangle$ spin states at 935.151 G offset magnetic field. Each point is an average of at least six independent measurements, and the error bars depict the standard error of the mean. The solid line shows the fit of a Gaussian profile to the data, yielding a variance of 23 kHz, which corresponds to 8 mG field uncertainty.

the population can be transferred between two states. Although theoretically 100% transition efficiency can be achieved, in the experiment it can be limited by small drifts in the magnetic offset fields. Thus, instead of a coherent pulse, a rapid adiabatic passage can be realized that consists of sweeping the magnetic field over the resonance for a fixed rf frequency. The advantage of this approach is its inherent insensitivity of the exact values of the offset magnetic field at the beginning and end of the sweep. The implementation of this technique for preparation of Li-Cs spin mixtures at 100 nK temperatures is described in Sect. 3.3.2. In principle, these methods could be applied to obtain ultracold gas samples in scattering channels that initially are empty, and cannot be created by removal of impurity atoms, for example, channels involving Li$|3/2,-3/2\rangle$ or Cs$|3,+2\rangle$ spin states.

For experiments involving type (ii) transitions the final spin state is unpopulated, therefore the preparation sequence can be simplified, as additional spin cleaning procedure is not necessary. As a drawback, this prevents one from observing coherent Rabi oscillations, since for typical experimental conditions the three-body recombination rate is much higher than the frequency of Rabi flopping. Additionally, the excitation of the higher lying Li $m_j = +1/2$ manifold induce two-body inelastic collisions, since dipolar spin relaxation channels open up that may lead to a significant portion of the incoming scattering flux to exit through energetically lower lying channels with high excess kinetic energy.

Nevertheless, we can employ type (ii) transitions to also calibrate the magnetic field and determine the upper limit of magnetic field inhomogeneities in our setup. A typical spectrum for the transition between Li$|1/2,-1/2\rangle$ and Li$|3/2,+3/2\rangle$ spin

states is shown in Fig. 2.8. The differential frequency shift of the transition amounts to ≈ 2.794 GHz/G in this magnetic field range. The transition does not exhibit any coherent fringes, which is a combined result from a large atom loss rate and fast dephasing due to magnetic field inhomogeneities. A fit of a Gaussian profile to the spectrum yields FWHM of 54 kHz and resonance frequency of 2776.834 MHz. This corresponds to 935.151 G offset magnetic field. Since it is a complicated problem to separate between the contributions of individual line broadening mechanisms, we attribute the total linewidth to the rest-gradient of our magnetic field setup as a simplification. In this way we obtain an upper limit of 8 mG for the uncertainty on the offset magnetic fields due to inhomogenieties.

2.4 Radio-frequency association of weakly-bound LiCs dimers

In the following section we investigate the interspecies scattering properties of ultracold Li-Cs mixtures of the two energetically lowest LiCs spin channels (see Eq. (2.11)) in the magnetic field range between 800 G and 1000 G. The performed experiments on rf association and atom-loss spectroscopy to precisely measure the positions of the LiCs s-wave Feshbach resonances are described in Sect. 2.4.1. Depending on the width of the resonance we separate them into two groups and use complementary approaches to determine their properties. For the broad resonances close to 843 G and 889 G we measure magnetic field dependent binding energies of weakly bound dimers through rf association. For the narrow resonances close to 816 G, 893 G, and 943 G we employ atom loss spectroscopy. Due to their small width the resonance position can still be detected with high accuracy.

Finally, we use these measurements as an input for a coupled-channels (cc) calculation that allows us to construct accurate Li-Cs molecular potentials, from which scattering length a_{LiCs}, resonance positions and widths are determined. This procedure is explained in Sect. 2.4.3. The obtained parameters agree well with the previous observations [Repp et al., 2013; Tung et al., 2013] and recent extensive theoretical studies [Pires et al., 2014a].

The determined mapping between a_{LiCs} and the external magnetic field will be pivotal for further experiments exploring or involving ultracold scattering between Li and Cs atoms. Up to now, a precise s-wave FR parameterization existed only for pure Cs [Berninger et al., 2013] and Li [Zürn et al., 2013; Julienne and Hutson, 2014] intraspecies scattering resonances, while Li-Cs interspecies collision properties were only approximately known from atom-loss measurements [Repp et al., 2013; Tung et al., 2013; Pires et al., 2014a]. Rf spectroscopy experiments that are described in the following section bridges this gap, because they allow to obtain precise FR

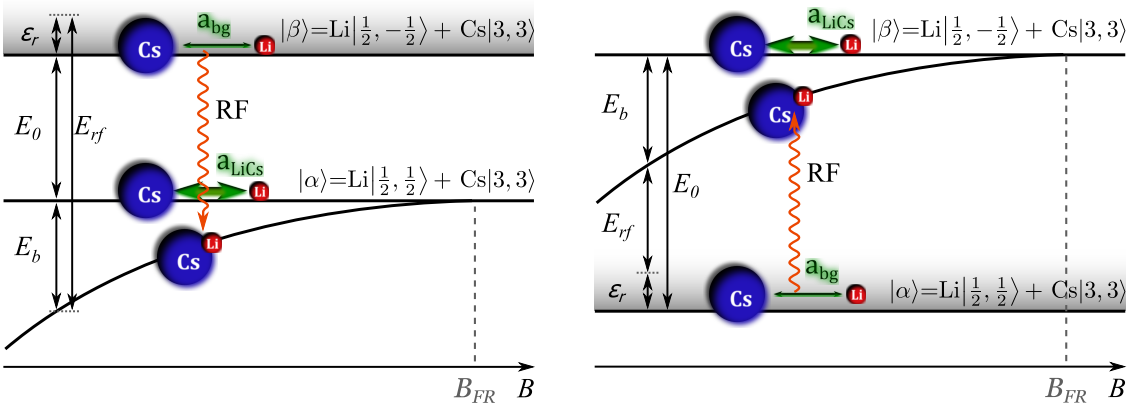

Figure 2.9: Radio-frequency association of Li-Cs Feshbach molecules close to the 843 G (left panel) and 889 G (right panel) interspecies Feshbach resonance. The mixture is initially prepared in the non-resonant scattering channel $|\beta\rangle$ ($|\alpha\rangle$) at a magnetic field close to the broad 843 G (889 G) s-wave Feshbach resonance in the resonant scattering channel $|\alpha\rangle$ ($|\beta\rangle$), which couples to the weakly bound molecular state under study. Depending on the frequency of the rf driving field either the free-free transition with the energy E_0 or the free-bound transition with the energy E_0+E_b or E_0-E_b for the 843 G or 889 G FR, respectively, can be studied. The energy ε_r denotes the relative collision energy of the scattering Li-Cs atom pair, and typically is much smaller than the other energy scales. The vertical scaling does not correspond to the real energy scale and is modified for better presentation.

parametrization, also in a close vicinity of the pole of a Li-Cs scattering resonance. They represent an order of magnitude improvement in accuracy over the previous determination. With respect to the s-wave scattering length, this knowledge now gives a complete description of the various three-body systems that can be constructed of Li and Cs atoms in the energetically lowest spin states.

2.4.1 Spectroscopy of LiCs Feshbach dimers

We start our experiments with the sample preparation as described in Sect. 2.3.1. By slightly adjusting the dipole trap power in the last two evaporation ramps we reduce the temperature to about 400 nK. To associate the molecules we create a mixture in the non-resonant scattering channel at a variable magnetic field close to the FR in the resonant state (see Fig. 2.9). For the measurements close to the 843 G Li-Cs Feshbach resonance this corresponds to the initial scattering channel $|\beta\rangle$, from which the colliding atom pairs are associated into bound dimers that couple to the scattering channel $|\alpha\rangle$, as depicted in the left panel of Fig. 2.9. For the 889 G resonance we invert this sequence and start with the scattering channel $|\alpha\rangle$ and associate dimers that couple to channel $|\beta\rangle$, as schematically given in the

right panel of Fig. 2.9. In order to create the LiCs Feshbach molecules we drive the system with a rectangular rf pulse with the frequency E_{rf}/h that is close to the resonance frequency E_0/h between the two energetically lowest Li spin states. In order to determine the molecular binding energy E_b, we scan the frequency of the applied rf field and observe the number of Li atoms that are left in the non-resonant state after the rf pulse.

Depending on the detuning of the rf-photon, in the atom-loss spectrum one can observe two distinct loss features. At energies E_0 the free-free transition that corresponds to a flip of the Li nuclear spin is populating the other Li spin state. This creates a mixture of three distinguishable particles that consist of atoms in the following spin states: Cs$|3,+3\rangle$, Li$|1/2,1/2\rangle$, and Li$|1/2,-1/2\rangle$. Since the scattering lengths at which these experiments are performed are large, rapid three-body loss can take place leading to a broad loss feature around the rf frequency E_0/h. The linewidth of this feature (see Fig. 2.11) is much larger than a typical linewidth of a magnetic field calibration line, for example, like the one depicted in Fig. 2.7. Additionally, its position may be shifted due to residual Cs density, which may lead to a mean-field shift of the free-free transition energy that is proportional to a_{LiCs}. Therefore we do not use this transition for neither magnetic field calibration nor direct extraction of the molecular binding energies.

In fact, a typical measurement procedure only records the free-bound spectrum, shown for each of the broad Li-Cs FRs in Fig. 2.10. Detuned from the free-free transition (not shown), which corresponds to a flip of Li nuclear spin, we observe an additional loss feature that originates from the association of LiCs Feshbach dimers. Here, during the rf-association pulse a mixture of LiCs Feshbach molecules and Li and Cs atoms in the initial scattering state is created, also leading to rapid three-body losses. The asymmetric lineshape originates from the relative collision energy distribution for the finite temperature of atoms, as explained in the next section. We also identify a similar loss signal at comparable values of detuning and amplitude in the remaining number of Cs atoms. To limit saturation effects, we experimentally optimize the power and length of the association pulse such that at most 30% of atoms are lost at the end of the rf pulse. The optimized pulse lengths range from 0.5 s close to the FR and 7 s away from it.

For magnetic field values at which the dimer binding energy is smaller than $\lesssim 10$ kHz the Feshbach molecule association line starts to overlap with the broadened free-free transition, therefore complicating extraction of binding energies. This situation is depicted in Fig. 2.11. The loss feature of the free-free transition develops a shoulder at frequencies around 76.286 MHz, which indicates the formation of bound dimers. We extract the corresponding molecular signal by fitting the free-free spectrum by a Lorentzian profile in the regions far away from this feature and subtracting the result from the total loss spectrum. While this gives a strong in-

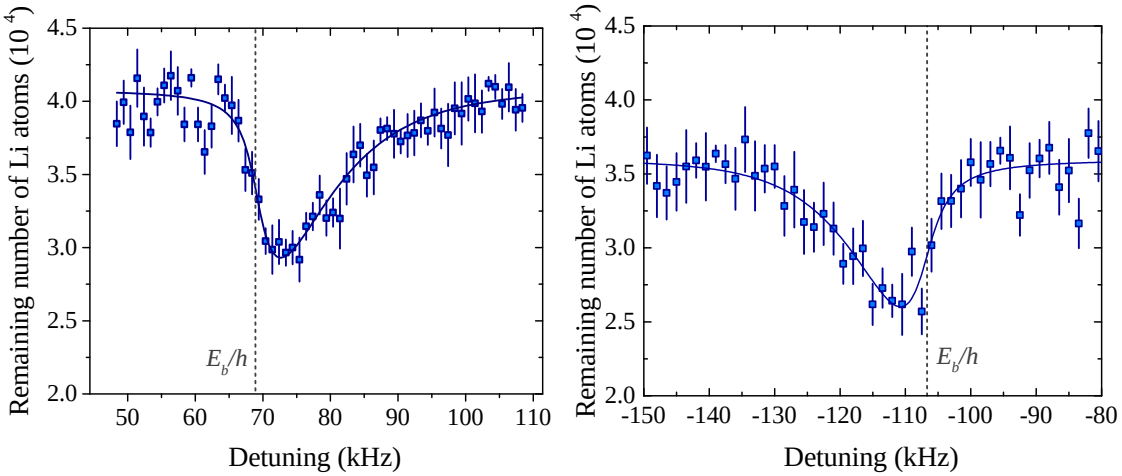

Figure 2.10: Remaining number of Li atoms after an rf association (free-bound) pulse of LiCs molecules at a magnetic field of 842.04 G (left panel) and 887.599 G (right panel) for the broad s-wave resonance in $|\alpha\rangle$ and $|\beta\rangle$ scattering channel, respectively. For these measurements the relative Li-Cs temperature was 400 nK. Each data point is an average of three measurements and the error bars represent the standard error. The solid line shows the fit to the data. In the left panel the binding energy is determined from the fit of Eq. (2.27), while for the fit in the right panel appropriate transformation of $K_2^M(E_{rf})$ has been made (see text). The vertical dashed line corresponds to the fitted binding energy.

dication that at these magnetic field values molecule formation is possible, precise determination of their binding energies is not feasible due to the strong influence of the free-free transition. The fitted binding energies significantly depend on the exact parameters of the fitted Lorentzian profile, therefore we exclude the spectra taken closer than 200 mG from the pole of the FR from the final analysis in Sect. 2.4.3.

2.4.2 Model of the association lineshape

We model the observed loss spectrum with the help of rate equations and the dimer binding energy dependent two-body association rate K_2^M [Chin and Julienne, 2005; Klempt et al., 2008]. The long association pulse lengths and low molecule yield, which is below our detection limit, indicates that the dimer association rate is much smaller than their loss rate. Assuming a quasi-stationary state, in which each produced molecule immediately gets lost through atom-dimer collisions, the time dependent Li atom loss at a given magnetic field is governed by K_2^M and thus can be described through the following equation

$$N_{\mathrm{Li}} = N_{\mathrm{Li}}^0 e^{-n_{\mathrm{Cs}} K_2^M t}, \tag{2.27}$$

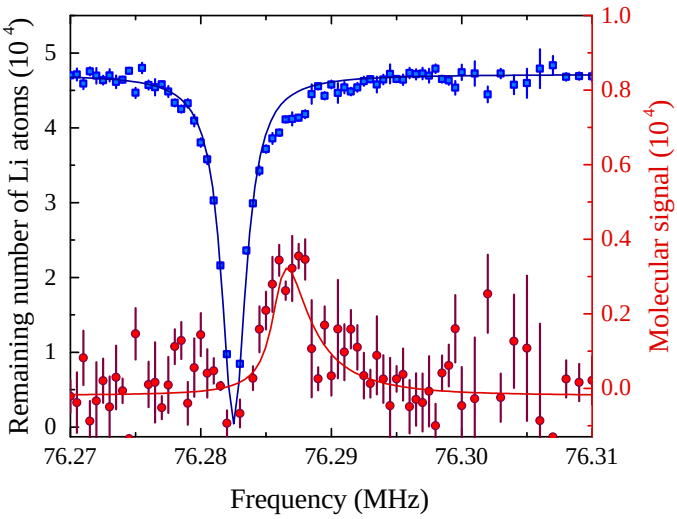

Figure 2.11: LiCs dimer association spectrum at 842.761 G. The free-bound transition is overlapping with the strongly broadened free-free transition. The blue rectangles depict the remaining number of Li atoms in the $|\beta\rangle$ scattering state after a 500 ms long rf pulse, and the blue solid line is a fit of a Lorentzian profile to the data. The red circles and line show the molecular signal and a fit of Eq. (2.27) to the data, respectively. The fit yields $E_b/h = 3.3(2)$ kHz and $\gamma = 2.1(7)$ kHz. Each point is an average of at least three independent measurements and the error bars represent the standard error of mean.

where N_{Li}^0 is the initial number of Li atoms in the non-resonant state, n_{Cs} denotes the density of the Cs gas cloud, t is the length of the applied rf pulse and K_2^M contains the functional form (see below) of the molecular association rate. Here we neglect single-body losses and assume constant n_{Cs}, which is justified by the fact that we are working in a low saturation limit of the rf transition. By solving the full system of rate equations we estimate that this approximation, using the simple Eq. (2.27), may introduce a minor error on the fitted atom loss amplitude, which does not exceed 10 %. Since the number of produced LiCs molecules at any given point through the experimental cycle is insignificant, we do not include the loss terms associated with the molecule-molecule recombination.

The rf-association process is equivalent to photoassociation (PA) from an initial scattering continuum state into an excited vibrational level [Napolitano et al., 1994; Jones et al., 2006]. Though, the lifetimes of the final states are significantly different. Whereas in PA it is given by the spontaneous decay of the associated level, for rf-associated dimers it is typically limited by collisions. This leads to the situation, where the association lineshape at ultracold temperatures contains information not only about the energy distribution of the initial scattering channel, but also its energy dependent Franck-Condon overlap with the molecular state [Chin and Julienne, 2005]. For a thermal ensemble that is prepared in the scattering state

$|\beta\rangle$ the two-body association rate K_2^M can be expressed as

$$K_2^M(E_{rf}) = C \int_0^\infty h(\varepsilon_r) F(\varepsilon_r, E_b) L_\gamma(E_{rf}, E_0 + E_b + \varepsilon_r) d\varepsilon_r, \tag{2.28}$$

where $h(\varepsilon_r) \propto e^{-\varepsilon_r/k_bT}$ is the number density of colliding atom pairs with relative energy ε_r and temperature T, and

$$F(\varepsilon_r, E_b) \propto \left(1 - \sqrt{\frac{E_b}{E_b'}}\right)^2 \frac{\sqrt{\varepsilon_r E_b} E_b'}{(\varepsilon_r + E_b)^2(\varepsilon_r + E_b')} \tag{2.29}$$

is the energy normalized Franck-Condon density between the scattering wave function of a free Li-Cs atom pair and a bound Feshbach dimer with binding energy E_b [Chin and Julienne, 2005; Klempt et al., 2008]. E_b' is defined through the Li-Cs reduced mass μ and the non-resonant channel scattering length a' as $E_b' = \hbar^2/(2\mu a'^2)$. The convolution of the spectroscopic line shape with the Lorentzian profile $L_\gamma(E_{rf}, E_0+E_b+\varepsilon_r)$ of width γ accounts for the strong collisional broadening, yielding an estimated lifetime of LiCs molecules in the mixture of around 30 μs. The prefactor C contains all the numerical factors resulting from the integration of rate equations, and experimental parameters that affect the molecule production rate, but which are approximately constant for a given magnetic field, as well as species-dependent atom-dimer inelastic collision rates[3]. It also accounts for uncertainties in the determination of the absolute gas densities, which, under realistic experimental conditions, can vary up to a factor of two due to systematic errors in measurements of the trap frequencies, temperature and the exact number of atoms.

The analysis of the atom-loss lineshape for a sample prepared in the scattering state $|\alpha\rangle$ is identical to the one presented above, with the sole exception that in this case the rf-photon energy needed for dimer association is smaller than the energy of the free-free transition (see Fig. 2.9). Consequently, the functional form of the association rate has to be adapted according to the energy conservation laws. The final expression for the association lineshape in state $|\alpha\rangle$ is obtained by the substitution $L_\gamma(E_{rf}, E_0 + E_b + \varepsilon_r) \to L_\gamma(E_{rf}, E_0 - E_b - \varepsilon_r)$, which is used for the fitting and analysis of dimer association lineshapes corresponding to the 889 G FR, as shown in the right panel of Fig. 2.10.

The binding energy of the Feshbach dimers at a given magnetic field is extracted by fitting Eq. (2.27) to the loss spectrum of Li atoms, as displayed in Fig. 2.10. We use E_b, N_{Li}^0, γ, and C as free fitting parameters and set $a' = -28.5\ a_0$ [Repp et al., 2013; Tung et al., 2013; Pires et al., 2014a]. Small variations in a' that are of the order of a few of percent affect the fitted binding energies on a permille level.

[3]The prefactor C slightly depends on n_{Cs} and n_{Li}. For atom losses, which do not exceed $\approx 30\%$ of the initial number of atoms, it does not change by more than 5 %.

The temperature of each species is determined in an independent measurement with identical trapping parameters and is kept fixed during the fit. To exclude systematic effects associated with the precise determination of relative temperature we verify that by increasing it by a factor of two the value of the fitted binding energy does not change by more than 1 kHz (see Fig. 2.12).

The extracted binding energy can be affected by several other systematic effects. One of them is the mean-field shift, which starts to dominate in the regime where the scattering length is comparable to the interparticle spacing, i.e. $na^3 \sim 1$. For our experimental densities of $n \approx 10^{11}$ cm^{-3} such shifts would become relevant at magnetic field regions with binding energies on the order of $E_b \approx 1$ kHz, which is sufficiently far away from the region where the experiments were performed. Additionally, by changing the background Cs atom density we checked that the observed molecular association line shifts stay within the statistical uncertainties of the fit, and therefore we do not include the mean-field shift in the analysis.

Another source of systematic resonance shifts is the confining optical dipole potential. The detuning of the dipole trap laser beam is large in comparison to the hyperfine splitting of the involved spin states, hence its created light shift is equal for both of them and can be neglected. However, the confining potential can contribute to the scattering state energy shift in two other ways. The first one is the confinement induced shift of the relative ground state energy for two colliding free atoms. Its magnitude can be calculated for two interacting particles in a cigar shaped harmonic trap [Idziaszek and Calarco, 2006], and for our dipole trap geometry with aspect ratio $\eta \approx 9$ it yields 325 Hz. The second complication is the fact that, in contrast to two identical atoms [Busch et al., 1998], the problem of two different atoms in a harmonic trap with unlike trapping frequencies does not separate into center-of-mass and relative coordinates (see, for example, [Bertelsen and Mølmer, 2007; Deuretzbacher et al., 2008]). The magnitude of the shift of the associated lowest energy state in a Li-Cs mixture can be estimated for our trapping geometry and mass-ratio, and is on the order of 50 Hz [Bertelsen and Mølmer, 2007]. Since the order of magnitude of these corrections is much smaller than the measured binding energies we neglect these effects in the model that we use to fit the data, however, we include them in the total systematic error budget.

It has been recently demonstrated in the ^{6}Li-^{40}K system that the scattering length, and thus the binding energy of the dimer can be manipulated by the differential light shift between the molecular and scattering state, leading to shifts in the FR positions [Jag et al., 2014]. In our measurements that were preformed in the vicinity of the 843 G Li-Cs Feshbach resonance, no modification of the binding energies with respect to the intensity of the trapping light could be observed. The measured binding energy as a function of the potential depth can be seen in Fig. 2.12. The fluctuations of the data points give an independent estimation of

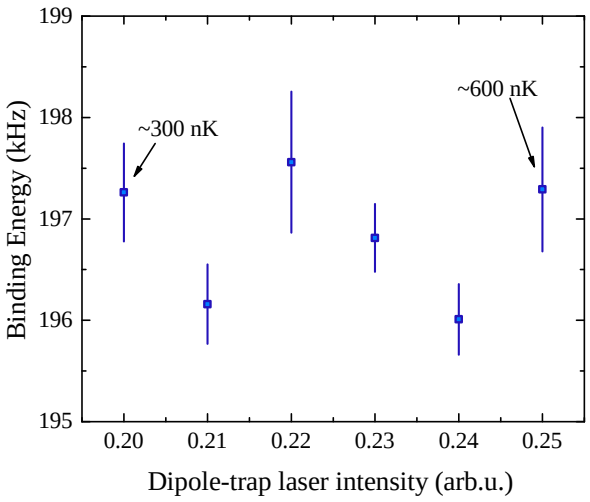

Figure 2.12: Binding energy as a function of the dipole-trap laser intensity at 841.5 G. The error bars depict the uncertainty of fitting Eq. (2.27) to the data. The corresponding temperature of the two limiting trapping settings is given in the graph next to the data points.

the accuracy with which the binding energy can be extracted from the association spectra. We include these fluctuations as an additional statistical error in the total error budget, since the trapping parameters and temperature may slightly drift from day-to-day.

2.4.3 Li-Cs scattering length and Feshbach resonances

To obtain a complete set of Li-Cs s-wave FR properties we employ two complementary approaches that separate the resonances in two groups based on their width ΔB. From the comparison of the atom-loss data with the binding energy measurement in Fig. 2.13 one can estimate that the shift of the atom-loss maximum with respect to the true resonance pole position can reach a couple permill of the resonance width ΔB. While for a narrow resonance with a width of 5 G this corresponds to a shift of $\sim$ 10 mG, on the order of our experimental uncertainty, for broad resonances it can reach several hundreds of mG, significantly impeding a correct determination of the scattering length.

By performing the measurements and the fitting procedure described in Sect. 2.4.2 for different external magnetic fields, we record the binding energy dependence on the external magnetic field, which is displayed in Fig. 2.13 for the two broadest FRs in the Li-Cs mixture.

Additionally, we determine the positions of the narrow s-wave resonances in the magnetic range between 800 G and 1000 G by atom-loss measurements, similar to

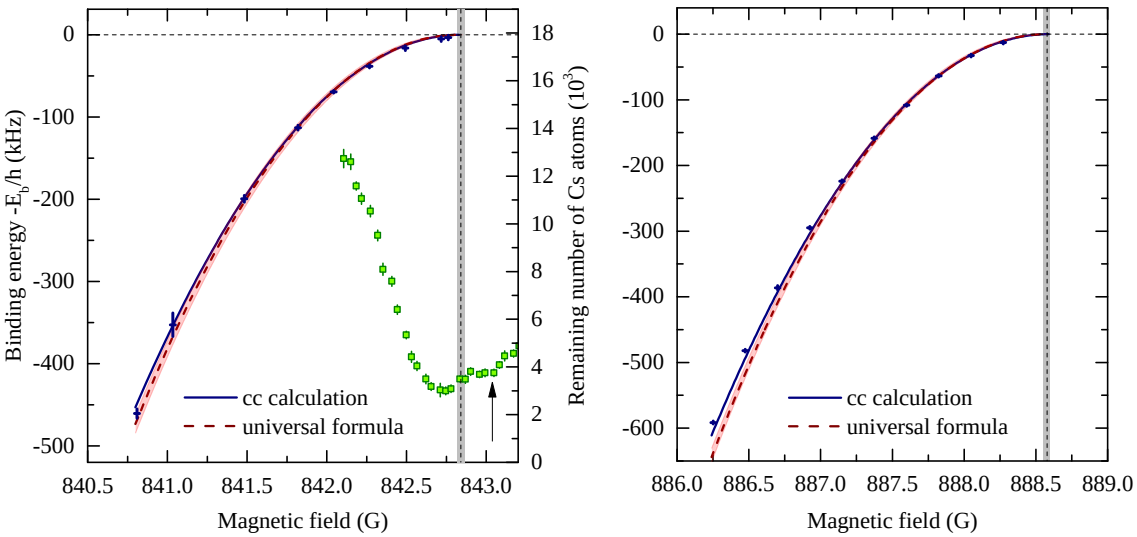

Figure 2.13: Binding energies of LiCs Feshbach molecules near the 843 G (left panel) and 889 G (right panel) Feshbach resonance, and corresponding atom-loss spectroscopy. The blue crosses show the dimer binding energy as extracted from a fit of Eq. (2.27) to the rf association spectrum at the given magnetic field. The error bars represent one standard deviation of the total error, resulting from statistical and systematic uncertainties. The blue and red solid lines show the calculated molecular energies from the coupled-channels model and the universal binding energy from Eq. (2.24) with the resonance parameters given in Table 2.1. The red shaded region corresponds to the uncertainty of the resonance parameters. The green squares show the remaining number of Cs atoms, and the error corresponds to one standard error of the mean. The systematic magnetic field uncertainty for the atom loss measurements in this figure is 30 mG. The vertical dashed line displays the resonance pole position and the shaded region corresponds to the uncertainty. The arrow in the left panel shows the position of the second excited $LiCs_2$ Efimov resonance with scattering length $a_-^{(2)}$.

the ones presented in Fig. 2.1. For these measurements we reach roughly an order of magnitude lower relative kinetic energies than in the previous works [Repp et al., 2013; Tung et al., 2013]. Their experimental positions B^e are extracted from a Gaussian profile fit to each of the loss features in the magnetic field range where the line shape is approximately symmetric, and are summarized in Table 2.1. The improved magnetic field stability and lower temperatures allow us to determine them with a roughly five-fold better precision than in our previous measurement [Repp et al., 2013].

To obtain an accurate mapping between the scattering length and the magnetic field that is independent of the employed analytical fitting model [Julienne and Hut-

Table 2.1: Positions of the LiCs s-wave Feshbach resonances. Unless specifically noted, the experimentally obtained resonance positions B^e are extracted by fitting a Gaussian profile to the loss spectra for the relative collision temperature T, at which the measurements were made. The numbers in the brackets represent the total error that includes uncertainty of the magnetic field, and statistical and systematic errors of determining the position of the resonance. The results of the coupled-channels calculation B^t are given as deviations $\delta = B^e - B^t$ from the observations and show excellent agreement with the data. B_{FR}, ΔB, and a_{bg} give the fitted resonance pole position, width, and background scattering length, respectively, for the calculation with kinetic energy of 1 nK.

Entrance channel	B^e (G)	δ (G)	T (nK)	B_{FR} (G)	ΔB (G)	a_{bg} (a_0)
Li$\|1/2,-1/2\rangle$	816.128(20)	-0.005	300	816.113	-0.37	-29.6
$\oplus$Cs $\|3,+3\rangle$	888.595(16)*	0.002	100	888.578	-57.45	-29.6
	943.020(50)	-0.033	400	943.033	-4.22	-29.6
Li$\|1/2,+1/2\rangle$	842.845(16)*	-0.000	100	842.829	-58.21	-29.4
$\oplus$Cs $\|3,+3\rangle$	892.655(30)†	0.005	100	892.629	-4.55	-29.4

* Extrapolated from rf association. The temperature shown is only used for the calculation of the scattering resonance and selected sufficiently low to reduce its influence to less than 5 mG. The error reflects the uncertainty of the field calibration.

† This measurement was performed in the bichromatic dipole trap with species selective optical potentials, as described in Sect. 3.3.

son, 2014], the data was analyzed with the full cc calculation[4] for the Li(2s)+Cs(6s) asymptote as in the previous work [Repp et al., 2013; Pires et al., 2014a]. In short, the determination of the final resonance positions relies on the creation of accurate LiCs molecular potential curves for the electronic singlet $X^1\Sigma^+$ and triplet $a^3\Sigma^+$ ground states. The potentials are constructed as a power series of the internuclear separation R, as in previous calculations on other alkaline-metal systems (see, e.g., Refs. [Marzok et al., 2009; Schuster et al., 2012; Strauss et al., 2010]), adding a short and long range part which gives the required degree of freedom for modeling the asymptotic binding energies. All coefficients are obtained by fitting, although the correlation between the conventional long range parameters C_6, C_8 and C_{10} is still significant, and thus they can only be taken as effective parameters. The derived potential model simultaneously reproduces the binding energies of the Feshbach molecules, the refined s-wave FR positions B^e from atom loss experiments, and 6498 rovibrational transitions from laser-induced Fourier-transform spectroscopy [Staanum et al., 2007]. We deduce the theoretical resonance positions

[4]The cc calculations were performed by Prof. E. Tiemann from University of Hannover, Germany.

B^t from the maxima of calculated two-body collision rates at the experimental kinetic energy.

For the binding energies below the 843 G resonance the two data points with the smallest binding energies are excluded from the fit. Their rf association spectra, due to experimental limitations, already overlap with the Li free-free transition spectra, which hinders a reliable extraction of the free-bound spectra for these respective magnetic field values, as discussed in Sect. 2.4.1 and shown in Fig. 2.11. Nevertheless, the calculated molecular binding energies are consistent also with these data points, indicating that at these magnetic field values a weakly bound dimer state still exists.

The results of the modeling are listed in Table 2.1 as deviation $\delta = B^e - B^t$ from the measured positions for the experimentally employed relative collision temperature T and drawn as solid lines in Fig. 2.13. These results provide almost an order of magnitude improvement over the previous determination of the FR positions through the trap-loss measurements [Repp et al., 2013; Tung et al., 2013] and the rf spectroscopy [Pires et al., 2014b], and they are consistent with the recent theoretical analysis [Pires et al., 2014a], if the differences in determining the resonance positions and experimental accuracy are taken into account.

Finally, we characterize the resonance profiles by calculating the scattering length dependence on the magnetic field at a kinetic energy of 1 nK and fitting this dependence with the conventional functional form

$$a(B) = a_{bg}\left(1 - \frac{\Delta B}{B - B_{FR}} - \dots\right) \tag{2.30}$$

with as many terms as there are resonances in the given channel. The resonance position B_{FR}, its width ΔB, and background scattering length a_{bg} are used as free fitting parameters, and they are given in Table 2.1. By including all observed resonances in a single fit of Eq. (2.30) one removes a possible slope of the effective background scattering length resulting from neighboring resonances. One could also fit the calculated profiles by a product of resonance functions, given by Eq. (2.21), for each resonance instead of the sum. This would result mainly in different values of ΔB, but as long as a consistent set of fitting function an corresponding parameters is used, the interpretation remains unchanged. The fitted values reproduce the calculated s-wave scattering length to better than 2% in the entire magnetic field range between 500 G and 1000 G, which we also use for the evaluation of the Efimov resonance positions in Chapter 3. There is a slight difference between the two theoretically obtained resonance pole positions B^t and B_{FR}. We suspect that it originates from the different types of numerical calculations that were used to extract these parameters, however further investigation is necessary to find the exact reason behind this difference. Therefore we estimate the error for the resonance pole positions from the systematic error from the magnetic field uncertainty and the

difference between the theoretical values, which yields ± 23 mG.

The resonance parameters that were obtained from the cc calculation are used to plot the simple single-channel formula defined by Eq. (2.24), which relates the universal dimer binding energy to the scattering length (see Fig. 2.13). The Li-Cs characteristic van der Waals energy scale [Chin et al., 2010] is 157 MHz, thus the influence of the short range effects on the measured binding energies is minimal. This is reflected in the nearly ideal $1/a^2$ scaling of the measured binding energies in this magnetic field range. Since the Li-Cs background scattering length $a_{bg} \approx -29.5\,a_0$ is small and negative, we expect only very minor influence of the virtual state in this regime. This contributes to the simple situation where the two LiCs binding energies are well described with the universal relation and can be treated independently from other neighboring resonances in the same scattering channels. This is in contrast to more complicated situations, like the one in Cs atoms where FRs overlap [Lange et al., 2009; Jachymski and Julienne, 2013].

Here determined position of the 843 G FR pole clearly deviates from the previously observed atom loss maximum [Pires et al., 2014b; Tung et al., 2014], as can be seen in Fig. 2.13. It also deviates from the result $B_{FR} = 842.75(3)$ G obtained in Ref. [Tung et al., 2014], where exclusively atom loss measurements are used to infer the resonance pole position. This illustrates that the use of atom loss alone is questionable for a reliable determination of the FR pole position, especially if the resonance width is much larger than experimental uncertainties, as it is in the present case. The definition of the resonance pole position is based on pure two-body scattering, whereas a number of different loss mechanisms may contribute to the total loss effect, the most prominent being the three-body collisions. The situation in the vicinity of the resonance's pole is complicated furthermore by the fact that not all of the inelastic three-body collisions result in an immediate loss of the atoms from the trap. Contribution from other recombination processes, for example, weakly-bound dimer formation and subsequent atom-dimer recombination, should be considered, which may lead to increased loss away from the pole of the FR. In this case the maximum of total atom losses can be shifted with respect to the maximum in the corresponding three-body loss rate [Dieckmann et al., 2002; Bourdel et al., 2003; Zhang and Ho, 2011]. The specific loss channels and the exact pathway of this decay in Li-Cs system still remain an open question, requiring a selective product state determination, which is not available at the present stage of our experiment. However, we expect that the shifts between the determined scattering pole positions and experimentally observed loss maxima can be explained or influenced by similar mechanisms as those discussed for other systems of ultracold gas mixtures [Weber et al., 2008; Machtey et al., 2012a; Zhang and Ho, 2011; Khramov et al., 2012; Dieckmann et al., 2002; Bourdel et al., 2003].

Chapter 3

Universality of $LiCs_2$ Efimov resonances

Parts of this chapter are based on the following manuscript and publication:

Universal three-body recombination in an ultracold Li-Cs mixture
J. Ulmanis, S. Häfner, R. Pires, E.D. Kuhnle, M. Weidemüller, D. Petrov, F. Werner
Manuscript in preparation

Observation of Efimov resonances in a mixture with extreme mass imbalance
R. Pires*, J. Ulmanis*, S. Häfner, M. Repp, A. Arias, E.D. Kuhnle, M. Weidemüller
Physical Review Letters **112**, 250404 (2014)
* Both authors contributed equally to this work.

The code for the calculations that were performed within the zero-range formalism via Eq. (3.31), as well as the function s_{11} that are used in this chapter have been provided to us by D. Petrov from Université Paris-Sud, Orsay, France.

In this chapter we investigate the universal behavior of weakly-bound $LiCs_2$ three-body states near a scattering resonance in the s-wave regime, often called the Efimov scenario. We start with a short phenomenological introduction in Sect. 3.1, and follow it up by a more rigorous discussion about its origin and mathematical description in a more general setting of the three-body problem in Sect. 3.2. We establish the hyperspherical framework in Sect. 3.2.1 that is later used for the interpretation and analysis of the Efimov effect in an ultracold Li-Cs Fermi-Bose mixture. With the help of zero-range potentials we recall how the Efimov effect originates as a direct consequence of an effective $-1/R^2$ potential in hyperspherical coordinates, and discuss the extension from homonuclear to heteronuclear systems. We intro-

duce the notion of scaling factors and Efimov resonance positions, which intimately characterizes the Efimov scenario, in Sect. 3.2.2. The basic physical picture behind recombination resonances that are used to probe the Efimov scenario in state-of-the-art experiments and its connection to the thermally averaged zero-range theory is explained in Sect. 3.2.3.

The creation of an ultracold mixture of different species in a single scattering channel at the required temperatures for the observation of Efimov resonances is a challenging task, as already discussed in Sect. 2.3. We introduce our upgraded approach for the preparation of Cs-Li Bose-Fermi mixtures at around 100 nK, a factor of four lower temperature than in the previous chapter, in Sect. 3.3. Finally, the observation of a series of three consecutive Li-Cs-Cs Efimov resonances with various approaches and in different temperature regimes and a comparison with a thermally averaged zero-range model are presented in Sect. 3.4.

3.1 The Efimov scenario in ultracold gases

The Efimov effect is defined by the emergence of an infinite series of weakly-bound trimer states in a three-body system interacting through resonant pairwise interactions that follows discrete scaling symmetry [Braaten and Hammer, 2006; Greene, 2010; Ferlaino et al., 2011; Wang et al., 2013]. Although the first derivation of Efimov [1970] did not specifically consider ultracold gas experiments, and he had ideas of nuclear physics in mind, the concept of three colliding particles with equal and resonant scattering lengths in the zero-energy ($k \to 0$) and zero-range ($r_0 \to 0$) limits is surprisingly similar in both, nuclear and ultracold physics [Zinner and Jensen, 2013]. Its basic morphology in a vicinity of a scattering resonance is illustrated in Fig. 3.1, using a Feshbach resonance in the Li-Cs system as an example[1]. The energy diagram consists of three major parts. Above the three-body dissociation threshold, the particles are unbound and their energy spectrum is continuous independent of the magnetic field or the scattering length, represented by the scattering continuum. Below the three-body dissociation spectrum the system behaves differently depending on the sign of the scattering length a. For $a > 0$ the system supports a weakly bound two-body state, the universal dimer state that was discussed in Sect. 2.2.3, while for $a < 0$ no two-body bound states are present at all. For systems consisting of atoms deeply bound two-body states are nevertheless present[2], independent of the scattering length, however, they are not required, per se, for the existence of the

[1] Most of the basic properties that are discussed in this section are independent of the exact composition of the three-body system and the nature of the scattering resonance itself, given that the Efimov effect is displayed for the considered system at all. See Sect. 3.2.2

[2] An exception is the $^4He_2$ interaction potential, which supports only a single bound state, close to the universal regime.

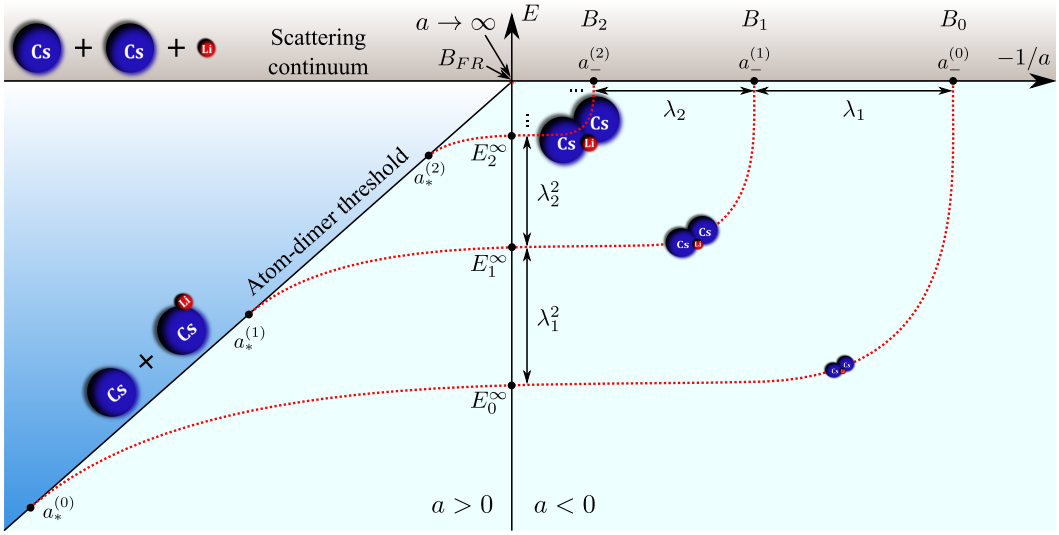

Figure 3.1: Sketch of the Efimov scenario. Schematic three-body energy spectrum of an ultracold Li-Cs-Cs system close to a Feshbach resonance as a function of the external magnetic field B or, equivalently, reciprocal Li-Cs scattering length $1/a$. Above the three-body dissociation threshold at $E = 0$ and the atom-dimer threshold at $E \propto 1/a^2$ the three free particles and the atom-dimer pair, respectively, exhibit continuous energy spectrum. In the light shaded area below both the thresholds, only three-body bound states are possible, shown as red dotted lines. The bound trimer energies intersect with the dissociation threshold at critical magnetic field values B_n that correspond to scattering lengths $a_-^{(n)}$, which denotes the positions of Efimov resonances.

Efimov effect. The three-body bound states that connect the atom-dimer threshold at positive scattering lengths with the three-body dissociation threshold at negative scattering lengths are the Efimov states.

These weakly-bound three-body states exhibit several remarkable properties, one of them being the discrete scaling symmetry. The Efimov trimer states are self-similar under rescaling of all length scales by a discrete scaling factor λ. Their energy spectrum at the scattering resonance E_n^∞, the positions $a_-^{(n)}$ and $a_*^{(n)}$ at which each trimer state crosses the three-body dissociation threshold and the atom-dimer threshold, respectively, are described by the discrete scaling laws

$$E_n^\infty = \lambda_{n+1}^2 E_{n+1}^\infty, \quad a_-^{(n+1)} = \lambda_{n+1} a_-^{(n)}, \quad \text{and} \quad a_*^{(n+1)} = \lambda_{n+1} a_*^{(n)}, \tag{3.1}$$

where the scaling factor[3] $\lambda = e^{\pi/s_0}$ is governed by a single dimensionless parameter s_0. s_0, in turn, is given by the mass ratios, quantum statistics, and number of

[3]We already anticipate minor corrections to the scaling laws in realistic systems by defining the scaling factor λ_n that depends on the Efimov period n. In the resonant limit ($a \to \infty$) $\lambda = \lambda_n = \lambda_{n+1}$.

resonant interactions of the three scattering particles. For example, for a system of three identical bosons $s_0 = 1.00624$, which yields $\lambda = 22.7$, and for a Li-Cs-Cs system with two resonant interactions $s_0 = 1.98277$, and hence $\lambda = 4.88$. Once these properties are known the parameter s_0 determines the complete structure of the Efimov spectrum. The procedure to obtain them is shortly illustrated in Sect. 3.2.2.

At the magnetic field values B_i or, equivalently, scattering length values $a_-^{(i)}$, at which the trimer states cross the tree-body dissociation threshold, enhanced recombination probability of three free particles at the scattering continuum into deeply bound dimer states exist. For an ultracold gas the obtained kinetic energy of the recombination products is typically much larger than the depth of the external confining potential, thus a fraction of the colliding trios leaves the trap. As a consequence, Efimov resonances emerge as enhanced inelastic three-body loss features in the recombination spectrum [Esry et al., 1999; Nielsen and Macek, 1999; Bedaque et al., 2000]. In fact, this approach is one of the main tools for the experimental investigation of Efimov states and with them related universal physics in ultracold quantum gases. Since we also probe the Efimov scenario in our experiment with atom recombination, we describe it in more detail in Sect. 3.2.3.

In ultracold atom experiments Efimov scenario has been investigated in equal mass systems of ^{6}Li [Ottenstein et al., 2008; Wenz et al., 2009; Lompe et al., 2010a; Huckans et al., 2009; Williams et al., 2009; Nakajima et al., 2010; Naidon and Ueda, 2011; Huang et al., 2014a], ^{7}Li [Gross et al., 2009, 2010, 2011; Pollack et al., 2009; Dyke et al., 2013; Machtey et al., 2012a], ^{39}K [Zaccanti et al., 2009; Roy et al., 2013], ^{85}Rb [Wild et al., 2012], and ^{133}Cs [Kraemer et al., 2006; Esry and D'Incao, 2007; Lee et al., 2007; Ferlaino et al., 2008, 2009, 2011; Berninger et al., 2011; Knoop et al., 2009b,a; Zenesini et al., 2013, 2014; Huang et al., 2014b; Huang et al., 2015] using three-body recombination resonances and in ^{6}Li [Lompe et al., 2010b; Nakajima et al., 2011] and ^{7}Li [Machtey et al., 2012b] using direct radio-frequency association of the weakly-bound three-body Efimov states out of the scattering continuum. The He systems are also approaching the required experimental regimes for the observation of the Efimov physics [Knoop et al., 2012; Voigtsberger et al., 2014]. The large scaling factor $\lambda = 22.7$ for homonuclear systems demands a temperature regime and magnetic field control that makes the observation of the excited Efimov states highly challenging, which is the reason why the first excited Efimov resonance has been observed only in a three-component Fermi gas of ^{6}Li [Williams et al., 2009; Huang et al., 2014a] and, recently, in a Bose gas of identical ^{133}Cs atoms [Huang et al., 2014b]. The observation might be feasible also in ^{7}Li system with the current experimental conditions [Rem et al., 2013; Dyke et al., 2013].

In heteronuclear systems, only ^{40}K^{87}Rb [Bloom et al., 2013; Hu et al., 2014] and ^{41}K^{87}Rb [Barontini et al., 2009, 2010] mixtures have been investigated so far, with

varying success. For them only ground state Efimov resonances have been observed, since the large scaling factor of $\lambda_{\mathrm{KRb}} \sim 131$ makes the observation of the excited Efimov resonances practically impossible if only two of the scattering lengths are resonant. In contrast, for three resonant interactions, if the success in homonuclear gases is any indication, it might be still feasible, since $\lambda_{\mathrm{KRb}} \approx 20.1$ (see discussion in Sect. 3.2.2 and Fig. 3.2).

In this work we probe the formation of Efimov scenario in a ^{6}Li-^{133}Cs Fermi-Bose gas, adding the third mixture to this list. The reduced scaling factor of $\lambda_{\mathrm{LiCs}} \approx 4.9$ allows us to observe a series of three consecutive Efimov resonances. The results presented in this chapter have been published in Ref. [Pires et al., 2014b]. Simultaneously, three Efimov resonances were observed also by Tung et al. [2014], however using atom-loss spectroscopy as the sole approach.

In a realistic system, in addition to the scaling factor, the energy spectrum of Efimov trimers is characterized by a three-body parameter (3BP), which in the resonant limit ($a \to \infty$) determines the trimer ground state energy E_0^{∞} or, alternatively, positions $a_*^{(0)}$ or $a_-^{(0)}$ on the atom-dimer or three-body dissociation thresholds, respectively. In the zero-range Efimov scenario, any one of these parameters represents sufficient amount of information to describe the entire ladder of Efimov states.

The necessity of such additional parameter, though, is a result of the simplified description of short-range interaction via the zero-range contact potentials and will be discussed in Sect. 3.2.2. The limits of this approach for the Li-Cs system will become apparent when analyzing a series of Efimov resonances in Sect. 3.4.4, and a possible remedy, especially for highly mass-imbalanced three-body systems in which the Born-Oppenheimer approximation can be well justified, will be offered in chapter 4.

3.2 Three-body scattering and the Efimov effect

In contrast to the two-body problem that was discussed in chapter 2, where semi-analytical solutions often exist for simple enough model potentials [Flambaum et al., 1999; Gao, 1998, 2000, 2001, 2003], analytical three-body solutions are generally unavailable. Different frameworks have been developed to treat this issue in various degrees of simplifications, for example, effective field theory [Bedaque and van Kolck, 2002; Kaplan, 2005; Platter, 2009; Hammer et al., 2013], renormalization group methods [Wilson, 1983; Fisher, 1998; Hammer and Platter, 2011], and the hyperspherical formalism [Zhen and Macek, 1988; Lin, 1995; Nielsen et al., 2001; Rittenhouse et al., 2011]. An extensive review of them is presented by Braaten and Hammer [2006], and an excellent overview can be found in Ref. [Wang et al., 2013]. In one, though, all of them are unified - the Efimov effect. In this work we analyze the experimental observations within the hyperspherical formalism, as it

delivers on interaction potentials based picture, reminiscent to the two-body framework discussed in chapter 2, and yields straightforward interpretation of underlying physics. In the next sections we closely follow the discussion from Refs. [Braaten and Hammer, 2006; Wang et al., 2013].

3.2.1 Key concepts of the hyperspherical formalism

A three-body system of particles $i = \{1, 2, 3\}$ with mass m_i that are interacting through potential $V_{3b}(\vec{r}_1, \vec{r}_2, \vec{r}_3)$ is governed by the time-independent Schrödinger equation

$$\left[-\sum_{i=1}^{3} \frac{\hbar^2}{m_i} \nabla_i^2 + V_{3b}(\vec{r}_1, \vec{r}_2, \vec{r}_3) \right] \Psi(\vec{r}_1, \vec{r}_2, \vec{r}_3) = E\Psi(\vec{r}_1, \vec{r}_2, \vec{r}_3). \tag{3.2}$$

In the most general form it contains nine degrees of freedom, which can be reduced to six when transforming it to the center of mass coordinates. Hyperspherical coordinates allow to simplify the problem further, by expressing Eq. (3.2) as a system of coupled equations that consist of a single length coordinate R, and five angular coordinates $\vec{\Omega}$, here condensed in a vector form. The hyperradius R is describing the overall size of the system, and is expressed as the root-mean-square separation of the three particles

$$R^2 = \frac{1}{3}\left(\vec{r}_{12}^2 + \vec{r}_{23}^2 + \vec{r}_{31}^2\right), \tag{3.3}$$

where $\vec{r}_{ij} = \vec{r}_i - \vec{r}_i$ are the separation vectors between individual pairs. The remaining angular coordinates can be defined through one of the Delves hyperangles[4] [Delves, 1960]

$$\alpha_k = \arctan\left(\frac{\sqrt{3}}{2}\frac{\vec{r}_{ij}}{\vec{r}_{k,ij}}\right) \tag{3.4}$$

in the range between 0 and $\pi/2$, and the corresponding vectors $\vec{r}_{ij}$ and $\vec{r}_{k,ij} = \vec{r}_k - (\vec{r}_i + \vec{r}_j)/2$. In the following we drop the vector signs for brevity and record the Schrödinger equation using the introduced hyperspherical coordinates, which yields

$$\left(-\frac{\hbar^2}{2\mu_3}\frac{\partial^2}{\partial R^2} + \frac{\Lambda^2 + 15/4}{2\mu_3 R^2} + V_{3b}(R, \Omega)\right)\psi(R, \Omega) = E\psi(R, \Omega), \tag{3.5}$$

[4] There exist several different choices for the mathematical definition of the hyperangles. Their advantages and disadvantages are discussed in great detail in [Wang et al., 2013].

where μ_3 is the three-body reduced mass that is defined by[5]

$$\mu_3 = \sqrt{\frac{m_1 m_2 m_3}{m_1 + m_2 + m_3}} \tag{3.6}$$

and Λ^2 denotes the generalized hyperangular kinetic energy operator in this six-dimensional space. The total wavefunction has been rescaled as $\psi = R^{5/2}\Psi$, and all of the interactions have been collected in potential $V_{3b}(R, \Omega)$.

The Schrödinger equation (3.5) can be conveniently solved using the *adiabatic hyperspherical representation*, introduced by Macek [1968]. In a close analogy to Born-Oppenheimer approximation, we treat the hyperradius R as an adiabatic variable. In other words, we assume that the angular dynamics can be separated from the hyperradial motion, which, for each fixed R, results in the adiabatic equation

$$\left[\frac{\Lambda^2 + 15/4}{2\mu_3 R^2} + V^R(\Omega)\right] \Phi_\nu^R(\Omega) = U_\nu(R)\Phi_\nu^R(\Omega). \tag{3.7}$$

This equation defines quantized hyperangular channel functions $\Phi_\nu^R(\Omega)$ and adiabatic potentials $U_\nu(R)$. It allows us to expand the reduced wavefunction $\psi(R, \Omega)$ on this basis as

$$\psi(R, \Omega) = \sum_\nu F_\nu(R)\Phi_\nu^R(\Omega), \tag{3.8}$$

with hyperspherical channel functions $F_\nu(R)$. Upon inserting Eq. (3.8) into the hyperspherical Schrödinger equation (3.5), and using orthonormality of hyperangular functions $\Phi_\nu^R(\Omega)$ one finally arrives at a coupled set of eigenvalue equations

$$\left[-\frac{\hbar^2}{2\mu_3}\frac{d^2}{dR^2} + U_\nu(R) - E\right] F_\nu(R) - \frac{\hbar^2}{2\mu_3}\sum_{\nu'}\left[2P_{\nu\nu'}(R)\frac{d}{dR} + Q_{\nu\nu'}(R)\right] F_{\nu'}(R) = 0, \tag{3.9}$$

for $F_\nu(R)$ at a given energy E, where $Q_{\nu\nu'}(R)$ and $P_{\nu\nu'}(R)$ represent non-adiabatic couplings between different hyperangular channel functions $\Phi_\nu^R(\Omega)$. These couplings characterize the first and second derivative of $\Phi_\nu^R(\Omega)$ with respect to R, thus if hyperangular channel functions change slowly enough, these couplings are small compared to the hyperspherical potential U_ν and can be neglected [Braaten and Hammer, 2006]. In this case the set of equations decouple, and one obtains

$$\left[-\frac{\hbar^2}{2\mu_3}\frac{d^2}{dR^2} + U_\nu(R)\right] F_\nu(R) = EF_\nu(R), \tag{3.10}$$

[5] Again, several different definitions for the reduced mass can be used. The combination $\mu_3 R^2$ is invariant, so different choices of μ_3 implies different definitions of R [Braaten and Hammer, 2006; Wang et al., 2013].

which describes a set of independent one-body problems in effective hypersherical potential $U_\nu(R)$. This is equivalent to the Born-Oppenheimer approximation for systems consisting of two heavy and one light particle that will be discussed in Sect. 4.2.

Equations (3.7) and (3.10) illustrate the essence of the adiabatic hyperspherical formalism. The solution of the three-body problem is reduced to finding the hyperangular channel functions $\Phi_\nu^R(\Omega)$ and adiabatic potentials $U_\nu(R)$, and using them to obtain the hyperspherical channel functions $F_\nu(R)$ and eigenenergies E, which in the case of the adiabatic equation (3.10) is a manageable task. If the non-adiabatic couplings are included, as in Eq. (3.9), the hyperspherical equations yield an exact representation of the three-body Schrödinger equation in terms of the adiabatic states and potentials, which contains most of the three-body scattering physics. The hyperspherical formalism in this form is often the method of choice for performing calculations of few-body low-energy scattering properties with realistic interparticle potentials [Esry et al., 1996; Nielsen et al., 1998; Suno et al., 2002; Wang et al., 2013].

3.2.2 The Efimov effect within the zero-range model

One of the major challenges in the description of the three-body problem is the choice of the interaction potential $V_{3\mathrm{b}}(\vec{r}_1, \vec{r}_2, \vec{r}_3)$. The reproduction of the *exact* three-body potential requires exquisite knowledge not only about the two-body interactions, but also short-range three-body physics [Hammer et al., 2013; D'Incao et al., 2009a]. In ultracold systems when atom pairs are sufficiently far away from the third particle, the interaction potential can be simplified as sum of isotropic pairwise interactions $V(r_{ij})$:

$$V_{3\mathrm{b}}(\vec{r}_1, \vec{r}_2, \vec{r}_3) = V(r_{12}) + V(r_{23}) + V(r_{13}), \tag{3.11}$$

to which additional three-body terms can be included if necessary [Braaten and Hammer, 2006; Wang et al., 2013; Hammer et al., 2013].

At this point one might be tempted to use the immense information about the two-body interaction potentials that have been obtained for various atomic species by molecular spectroscopy. With the advent of Feshbach resonance spectroscopy potential models with unprecedented precision are either available or obtainable for different combinations of atoms that are used in ultracold experiments. However, as already discussed in chapter 2, interactions at these temperature regimes are probing an energetically small window around the two-body scattering threshold. Thus the large de Broglie wavelength makes the short-range properties of the potential characterized by the range r_0 largely irrelevant, while long-range behavior is dominant.

Therefore, let us recall the properties of an universal few-body system, which

by the definition, do not depend on the exact shape of the underlying interaction potentials. The universal nature of a three-body system, for example, the three-body energy spectrum or the three-body scattering observables, become particularly well apparent, if the interaction between the particles is represented by a pseudo-potential with an interaction range that is zero. In this way all non-universal physics, which, in general, depend on the exact shape of interaction potentials, are excluded from the description. Clearly, the probability amplitude of the scattering wavefunction is non-zero also in the short-range part of the potential, which may eventually lead to corrections, but this is discussed in more detail in chapter 4. The simplest zero-range pseudo-potential $U_{\mathrm{zr}}(r)$ for binary interaction in three dimensions is the contact potential

$$U_{\mathrm{zr}}(r) = \frac{2\pi\hbar^2 a}{\mu}\delta(\vec{r})\frac{\partial}{\partial r}r. \tag{3.12}$$

which is equivalent to the Bethe-Peierls boundary condition $\Psi = 1/r_{ij} - 1/a$ for interparticle distance $r_{ij} \to 0$ [Petrov, 2010]. The length scale r_0 defines the short range limit, which for alkali atoms in the electronic ground state can be described by the characteristic van der Waals range r_{vdW}, thus $r_0 \approx r_{\mathrm{vdW}}$, typically on the order of couple tens of a_0 (see Sect. 4.2.2 for the definition of r_{vdW}). Nevertheless, the zero-range potential by construction is required to reproduce the behavior of the two-body wavefunction in the limit $a/r_{\mathrm{vdW}} \to \infty$. It is well fulfilled for most of the Efimov states in homonuclear systems, for which the ratio $|a|/r_{\mathrm{vdW}} \gtrsim 7$ [Berninger et al., 2011; Wild et al., 2012; Roy et al., 2013; Huang et al., 2014a].

The key advantage of zero-range approaches is that the Schrödinger equation (3.2) can be often solved analytically with a large variety of approaches, all of which produce equal results [Braaten and Hammer, 2006; Wang et al., 2013]. In fact, the essential features of Efimov physics can already be understood by analyzing the energy spectrum of Eq. (3.10), which was also done in Efimov's original analysis [Efimov, 1970]. The insertion of pairwise contact interaction (3.12) into the three-body potential in Eq. (3.11), yields the adiabatic hyperspherical potentials

$$U_\nu(R) = \frac{\hbar^2}{2\mu_3}\frac{\bar{s}_\nu^2 - 1/4}{R^2}, \quad \text{for } r_0 \ll R \ll |a|\,, \tag{3.13}$$

where the parameters $\bar{s}_\nu$ are determined by the solutions of the transcendental equation

$$\bar{s}_\nu \cos\left(\frac{\pi}{2}\bar{s}_\nu\right) - \frac{8}{\sqrt{3}}\sin\left(\frac{\pi}{6}\bar{s}\nu\right) = 12^{-1/4}\sin\left(\frac{\pi}{2}\bar{s}_\nu\right)\frac{2R}{a} \tag{3.14}$$

for three identical bosons. The Efimov effect emerges in the limit $R/a \to 0$. In this case there exists only one imaginary solution, $\bar{s}_0 = is_0 = i1.00624$, which corresponds to an attractive hyperspherical potential $U_0(R)$ that supports three-body bound states, the Efimov states. The rest of the infinitely many solutions $\bar{s}_{\nu>0}$

are real and positive and the corresponding potentials $U_{\nu>0}(R) > 0$ are repulsive.

The Efimov effect is a direct consequence of the attractive $\propto -(s_0^2 + 1/4)/R^2$ hyperspherical potential given by Eq. (3.13) with the parameter s_0. The bound state energies $E_n^{(a)}$ in the resonant limit $a \to \infty$ are obtained by solving Eq. (3.10) for single attractive channel with the potential $U_0(R)$, given by Eq. (3.13). The hyperspherical equation then reads

$$-\frac{\hbar^2}{2\mu_3}\left[\frac{d^2}{dR^2} + \frac{s_0^2 + 1/4}{R^2}\right] F_0(R) = E_n^{\infty} F_0(R)., \tag{3.15}$$

and results in an energy spectrum

$$E_n^{\infty} = -e^{-2\pi(n+1)/s_0}\frac{\hbar^2 k_*^2}{\mu_3}, \tag{3.16}$$

with infinitely many bound states that are separated by the scaling factor $\lambda^2 = E_n^{\infty}/E_{n+1}^{\infty}$. Here, n is the index of the Efimov state, and k_*^2 denotes the wave vector of the ground Efimov state labeled by $n = 0$. The energy spectrum is characterized by the scaling factor $\lambda = e^{\pi/s_0} = 22.7$. The remarkable property of an $-1/R^2$ potential to support an infinite number of quantized energy levels [Landau and Lifshitz, 1991; Coon and Holstein, 2002; Essin and Griffiths, 2006] is the reason behind the infinite geometrical progression of the three-body bound states in the resonant limit, which Efimov predicted 45 years ago.

As a consequence of the employed zero-range potential, resulting in an $-1/R^2$ potential, the ground state of the trimer energy spectrum diverges, reminiscent of the Thomas effect [Thomas, 1935], and well know in quantum physics as "fall to the center" [Landau and Lifshitz, 1991]. In nature, however, the short-range part of the potential is strongly repulsive, which also leads to formation of a strongly repulsive barrier in the hyperspherical potential. In the zero-range model, though, such information is lost because of the assumption of the contact interaction. It can be re-introduced by choosing an appropriate value of k_*^2 or introducing a hard-sphere potential at a particular value of r_0, such that the three-body energy of the ground Efimov state is reproduced. These are two of the possible definitions of the three-body parameter. Various other ways of taming the diverging ground state of a generic $\propto -1/R^2$ potential are discussed by, for example, Coon and Holstein [2002] and Essin and Griffiths [2006].

For a general three-body system the parameter s_0 is determined by the mass ratio, number of resonant interactions, and the quantum statistics of the particles, as the correct symmetry of the scattering wavefunction needs to be imposed. Such situations were already discussed by Amado and Noble [1972] and Efimov himself [Efimov, 1970, 1971, 1973, 1979]. In fact, not every combination of three particles

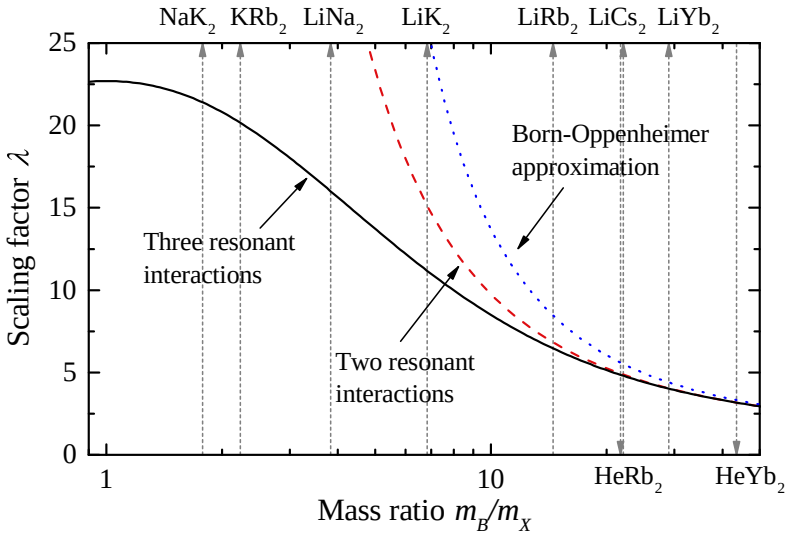

Figure 3.2: Efimov scaling factor as a function of the mass ratio for a system of two identical bosons B and one distinguishable particle X with three (black solid line) and two (red dashed line) resonant interactions, and in Born-Oppenheimer approximation (blue dotted line, see Sect. 4.2.1). Vertical dashed lines show mass-ratios for a selection of experimentally employed heteronuclear mixtures.

results in the Effimov effect, however all of these situations are extensively reviewed in Refs. [Braaten and Hammer, 2006; Wang et al., 2013].

Here we will discuss a general system BBX consisting of two identical bosons B and a third distinguishable particle X with masses m_B and m_X, respectively, which is of the most interest for our experiments. In this case the effective potential is equal to the one in Eq. (3.13). Identical to the three-boson case, only a single attractive hyperspherical potential for s_0 is obtained, leading to the effective hyperspherical equation (3.15), and formation of the Efimov series. The resulting scaling factors $\lambda = e^{\pi/s_0}$ are shown in Fig. 3.2 as a function of the mass ratio m_B/m_X, and have been calculated from an analogous to Eq. (3.13) system of equations. Two possible approaches in determining them are the Faddeev equations [Fedorov and Jensen, 1993] and the original Efimov's work [Efimov, 1970, 1971, 1973] that are reviewed by Braaten and Hammer [2006] and Wang et al. [2013], respectively. In producing Fig. 3.2 we have used the matching equations that are obtained from the low-energy Faddeev equation, given in Ref. [Braaten and Hammer, 2006].

As the mass ratio is increased the scaling factor decreases, leading to a denser three-body energy and recombination resonance spectrum (see Sect. 3.2.3). As already mentioned in Sect. 3.1 this is beneficial for the experimental observation of several consecutive Efimov resonances [D'Incao and Esry, 2006; Helfrich et al., 2010]. A series of denser lying features can be observed at higher temperatures, and the requirements for the tunability of the scattering length, for example, the required

magnetic field stability and width of the employed Feshbach resonance, can be relaxed in comparison to the homonuclear case.

It is interesting to note that depending on the number of resonant interactions in the system[6] the scaling factor can take two distinct limiting values. The difference between them increases as the mass ratio is decreased, suggesting that the scaling factor in systems with intermediate mass imbalance, for example, LiK_2 or $LiNa_2$, can take a broad range of values depending on the exact magnitude of the interaction strength between the two like particles. Furthermore, in this range the limit $R/a \to \infty$ is not strictly justified anymore, which may lead to deviations from the limiting $1/R^2$ scaling behavior of the hyperspherical potential and, consequently, modified trimer energy and recombination resonance spectrum. This, however, has not been actively investigated, since the scaling factor itself is large, and therefore experimental observation of a series of Efimov states is challenging. For the Li-Cs system the scaling factor ranges between 4.88 and 4.80 for two and three resonant interactions, respectively, on the order of few percent, thus well below the present experimental uncertainties.

3.2.3 The Efimov scenario as recombination resonances

Up till now we have mostly discussed the properties of the Efimov trimers at the pole of the scattering resonance ($a \to \infty$). However, with the exception of direct radio-frequency association of the three-body states [Lompe et al., 2010b; Nakajima et al., 2011; Machtey et al., 2012b], observations of the Efimov scenario rely on the detection of scattering observables close to the three-body dissociation threshold. Since the detection of number of atoms is one of the major tools for ultracold gas experiments, let us briefly recall how the three-body inelastic collision rate changes as the scattering length is tuned from a small and negative value, far away from the pole of the resonance, to the pole itself. We expect the Efimov resonances to appear as enhanced three-body loss features that emerge at the specific values of B_n (equivalently, $a_-^{(n)}$), since at these positions the recombination into deeply-bound atom-dimer states are enhanced due to Efimov trimers crossing the three-body dissociation threshold (see also Fig. 3.1) [Esry et al., 1999; Nielsen and Macek, 1999; Bedaque et al., 2000]. Here, we focus on the for our experiments relevant scattering length range $a < 0$ that excludes the possibility of three-body recombination into weakly-bound dimer-atom pairs, and exemplify the formation of a recombination resonance with the zero-range S-matrix scenario for a mixture BBX consisting of two identical bosons B and one distinguishable particle X [Petrov and Werner, 2015; Mikkelsen et al., 2015]. The same picture holds for a general three-body system if

[6] We don't discuss the case for a single resonant interaction, since in such systems the Efimov effect does not occur [Braaten and Hammer, 2006].

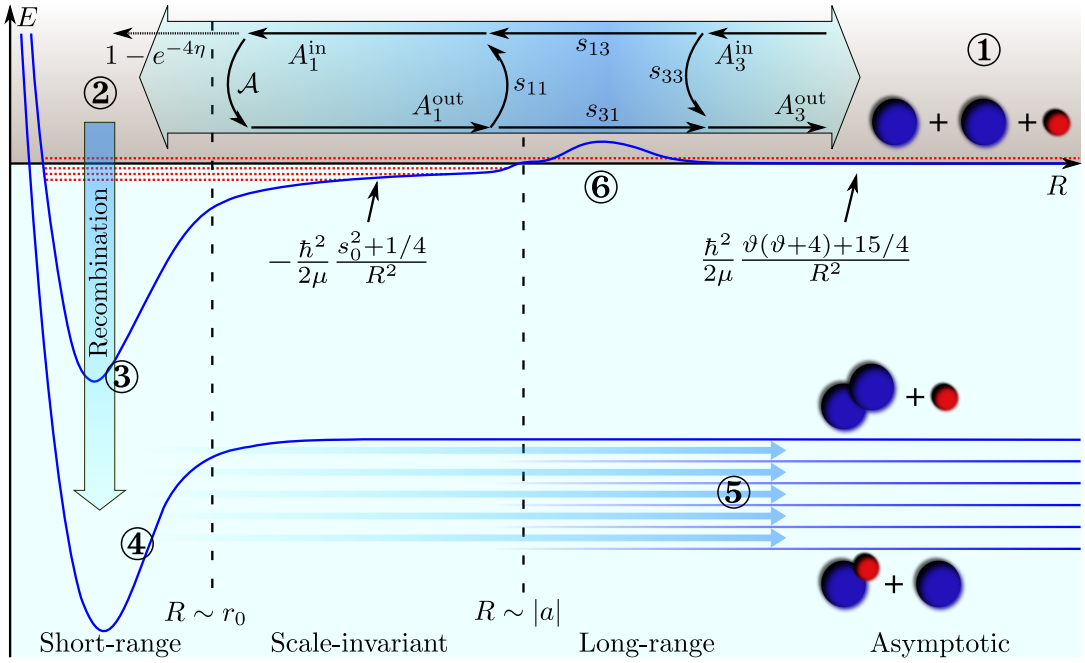

Figure 3.3: Three-body collision and recombination in hyperspherical potentials for $a < 0$. The system is initially prepared in the asymptotic region of the triatomic channel ① ($R \gg |a|$) and approaches smaller hyperradius R with amplitude $A_3^{\rm in}$. In the short-range region ② ($R \lesssim r_0$) it undergoes a three-body recombination ③ into a deeply-bound dimer and atom channel ④ with probability $1-e^{-4\eta}$, which is not confined anymore, thus leading to trap losses ⑤. The initial three-body wavefunction is reflected to large R and leaves with amplitude $A_3^{\rm out}$. The transmission and reflection amplitudes s_{11}, s_{13}, s_{31}, s_{33} at the potential barrier ⑥ ($R \sim |a|$), generated by the asymptotic behavior of the hyperspherical potentials, and the reflection amplitude $\mathcal{A}$ determines the distribution of the incoming wavefunction over the various pathways. The recombination may proceed into many deeply-bound states that couple to the incoming channel with various probabilities, all of which are parametrized by the single parameter η. The energies of Efimov states are schematically represented by the red dotted lines.

the wavefunctions are appropriately symmetrized, as explicitly shown and applied for the case of three-identical bosons [Braaten et al., 2008; Rem et al., 2013; Huang et al., 2014b].

The basic morphology of a three-body collision for $a < 0$ in hypershperical coordinates is illustrated in Fig. 3.3. The Efimov resonances arise due to three-body shape resonances behind a potential barrier [Esry and D'Incao, 2007]. In a general three-body system the extraction of the corresponding recombination rates is a complicated task that requires accurate treatment of coupling between scattering channels and short-range potentials, which can be highly demanding even for modern numerics. However, analytic inelastic and elastic collision rates can be obtained from

simple arguments based on the probability conservation and the asymptotic forms of the hyperspherical potentials and three-body wavefunctions [Efimov, 1979; Braaten and Hammer, 2006; Braaten et al., 2008; Rem et al., 2013; Petrov and Werner, 2015]. We briefly discuss this procedure for the zero-range theory. It starts by separating the ground state hyperspherical potential into two asymptotic regions, in which the wavefunction of the three-body problem can be solved analytically:

(i) $R \gg |a|$, the asymptotic region, in which the potential has the behavior

$$U_0(R \to \infty) = \frac{\hbar^2}{2\mu_3} \frac{\vartheta(\vartheta+4)+15/4}{R^2}, \tag{3.17}$$

where ϑ is a non-negative integer, and

(ii) $|a| \gg R \gg r_0$, the scale-invariant region, equivalent to Eq. (3.13) with $\nu = 0$.

The wavefunctions in these regions are characterized by incoming and outgoing contributions with corresponding amplitudes $A_1^{\text{in,out}}$ and $A_3^{\text{in,out}}$ for the scale-invariant and asymptotic region, respectively (see Fig. 3.3).

In the short-range region $R \lesssim r_0$ the wavefunction and couplings for realistic interaction potentials strongly depend on the interaction potential, which are typically difficult to calculate. In the zero-range theory ($r_0 \to 0$) this is conveniently parametrized by imposing the three-body contact condition [Petrov and Werner, 2015]

$$A_1^{\text{in}} = \mathcal{A} A_1^{\text{out}} \tag{3.18}$$

where the reflection amplitude $\mathcal{A}$ from the point $R = r_0$ is expressed by

$$\mathcal{A} = -(kR_0)^{-i2s_0} e^{-2\eta}. \tag{3.19}$$

The modulus of the reflection probability $|\mathcal{A}|^2 = e^{-4\eta}$ gives the decrease of the probability flux incident on the boundary r_0 that is parametrized by the single, non-universal inelasticity parameter η. It encapsulates all of the specific short-range interaction details, and is typically determined experimentally. The total lost flux φ_{loss} is obtained by integrating the probability current over a vanishingly small hypersphere encircling the origin, which yields $\varphi_{\text{loss}} = (1-e^{-4\eta})\,|A_1^{\text{out}}|^2$. The phase of the reflected wavefunction with respect to the incoming wavefunction is determined by R_0, which in this form of the zero-range theory fulfills the role of the three-body parameter.

In the intermediate region $R \sim a$ the couplings between different hyperspherical channels are important, as discussed in Sect. 3.2.1, thus the potential may exhibit a non-trivial shape, and the explicit wavefunction in this region cannot be easily acquired. The formation of a repulsive potential barrier is evidence of it, although

expected, because of the transition between the repulsive asymptotic and attractive scale-invariant regimes. Nevertheless, the incoming and outgoing probability flux can only originate from the scale-invariant and asymptotic regions and must be conserved, which allows to express the evolution in this region by equation (see also Fig. 3.3)

$$\begin{pmatrix} A_1^{\text{out}} \\ A_3^{\text{out}} \end{pmatrix} = \begin{pmatrix} s_{11} & s_{13} \\ s_{31} & s_{33} \end{pmatrix} \begin{pmatrix} A_1^{\text{in}} \\ A_3^{\text{in}} \end{pmatrix}, \tag{3.20}$$

where S-matrix elements s_{ij} represent the scattering amplitudes from the channel j into i, and can be easily computed [Petrov and Werner, 2015]. In combination with Eq. (3.18) and the unitary property $|s_{13}|^2 = 1 - |s_{11}|^2$ of the S-matrix this yields

$$\varphi_{\text{loss}} = (1 - e^{-4\eta}) \frac{1 - |s_{11}|^2}{|1 - s_{11}\mathcal{A}|^2} \left|A_3^{\text{in}}\right|. \tag{3.21}$$

Finally, amplitude A_3^{in} is obtained by evaluating the energy dependent hyperangular overlap between the incoming plane wave in the asymptotic region and the hyperangular wavefunction $\Phi_0^R(\Omega)$ of the lowest three-body scattering channel (see Sect. 3.2.1 and 3.2.2). After averaging over the hyperangular coordinates and the direction of $\hat{k}$, the energy dependent rate of three-body recombination events per unit volume $L_3(k) = \cos(\phi) \langle \varphi_{\text{loss}} \rangle_{\hat{k}} / 2$ is obtained as

$$L_3(k) = \frac{64\pi^2 \cos^3 \phi}{2\mu k^4} (1 - e^{-4\eta}) \frac{1 - |s_{11}|^2}{\left|1 + s_{11}(kR_0)^{-i2s_0} e^{-2\eta}\right|^2}. \tag{3.22}$$

The expression in Eq. (3.31) that is compared with experimentally determined three-body loss rates at finite temperatures follows immediately after thermal averaging [Petrov and Werner, 2015].

The behavior of the thermally averaged three-body recombination rate given by Eq. (3.31) is depicted in Fig. 3.4. In addition to a general scaling with a_{LiCs}^q, where $q \sim 4$, the spectrum is modulated with maxima that are approximately log-periodically distributed. Their origin can be intuitively understood by noting that the approximate hyperspherical potential in Fig. 3.3 contains a barrier, behind which a quasi-bound three-body energy level may be located. This is the typical setting of a shape resonance [Esry and D'Incao, 2007]. As the scattering length is varied, the position and height of the barrier changes as $|a_{\text{LiCs}}|$ and $1/a_{\text{LiCs}}^2$, respectively. The resonance energy decreases with increasing $|a_{\text{LiCs}}|$, and becomes resonant at some particular a_{LiCs}, which gives rise to a significant amplitude gain of the scattering wavefunction in the scale-invariant and short-range regimes, i.e. behind the barrier. This, in turn, increases the coupling to the atom-dimer channels and the inelastic recombination rate grows.

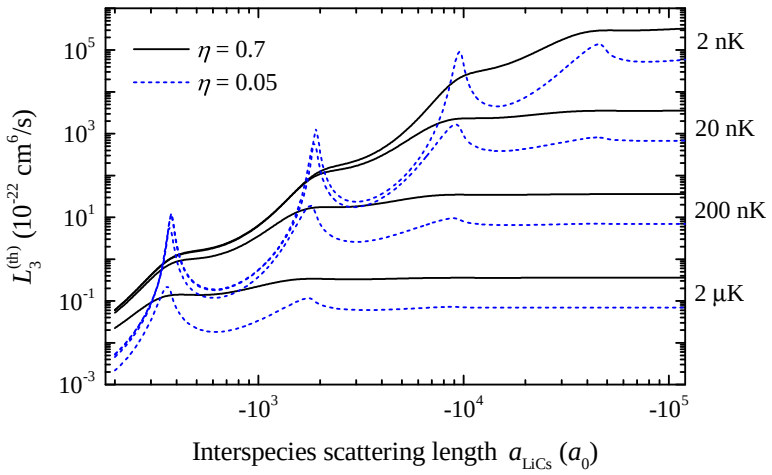

Figure 3.4: Li-Cs-Cs three-body recombination rate as a function of scattering length in the vicinity of the 843 G Feshbach resonance for $\eta = 0.7$ (black lines) and $\eta = 0.05$ (blue dashed lines), with the correct $a_{\mathrm{CsCs}}(a_{\mathrm{LiCs}})$ dependence included. Labels on the right side give the temperature for which the thermal averaging was performed. The graph was produced with zero-range three-body parameter $R_0 = 141\ a_0$.

The upper bound of the three-body recombination rate can also easily be understood. The maximum collisional cross section that can be achieved by increasing the scattering length a_{LiCs} is limited by the thermal de Broglie wavelength. It is decreased for increasing temperatures, which reduces the likelihood of three particles to collide and thus the overall amplitude of the incoming three-body scattering wavefunction around the unitarity ($a_{\mathrm{LiCs}} \to \infty$) is smaller. The difference between the two different inelasticity parameters is caused by the reflection from the short-range region, i.e. $R \sim r_0$. For smaller η more of the probability flux is reflected, which increases the amplitude of the outgoing scattering wavefunction and leads to a smaller fraction of atoms undergoing recombination.

Essentially similar results for the BBX system interacting through pairwise zero-range potentials in the zero-temperature limit have also been obtained by the effective field theory [Helfrich et al., 2010; Helfrich and Hammer, 2010]. The model assumes two resonant interactions $a_{BX} \to \infty$, while the intraspecies scattering length is set to zero $a_{BB} = 0$. The here presented S-matrix formalism explicitly includes the collisional energy dependence that enables straightforward thermal averaging and appropriate treatment of a_{BB}, contained in the generalized scattering matrix

amplitude s_{11} [Petrov and Werner, 2015]. For the analysis of our experiments both of these attributes are important. Although the temperatures at which our experiments are performed are in the hundred nano-Kelvin regime, the contribution of the finite collisional energy distribution is non-negligible, and the excited Efimov resonances are located in the unitarity limit $|a_{\mathrm{LiCs}}| \gtrsim 1/k$, as can be seen in Fig. 3.4. Additionally, the $a_{BB}(a_{BX})$ dependence contributes to the shape of the three-body loss rate, and is required for accurate comparison with the experiment. Both of these aspects in our measurements are further analyzed with here presented formalism in Sect. 3.4.4.

3.3 Producing ultracold Li-Cs mixtures II

The creation of an appropriate confining potential for an ultracold gas mixture consisting of different atomic species is one of the major experimental challenges. Generally, the internal structure of each of the species is different, which leads to dissimilar responses to externally applied fields that are used for the production of the confining potential. This complication is, in general, present in any state-of-the-art mixture experiment, for which the confining potential is generated by optical dipole traps [Grimm et al., 2000]. It is based on the interaction of the induced electric dipole moment with the light field, which often allows one to trap and manipulate neutral particles almost independently of their internally occupied degrees of freedom, nevertheless, differently for each of the species. A very versatile concept is the use of species-selective optical potentials, which allows one to individually shape and manipulate the confining potentials for each of the species [LeBlanc and Thywissen, 2007], demonstrated in the studies of entropy exchange between two gases [Catani et al., 2009] and mixed dimensional systems [Lamporesi et al., 2010] for the KRb system. While these differences can be used to create and engineer broad variety of effective potentials for each of the species, influencing a single, a selection, or all of the given species in a predetermined manner, it can also lead to increased experimental complexity and situations where the generation of the preferential potential landscape is highly demanding.

An important issue when dealing with ultracold mixtures with a large mass imbalance is the significantly different gravitational potential that is experienced by each of the species. This may lead to reduced spatial overlap between the ultracold gas clouds, which can be disadvantageous, for example, if the observation of interspecies interactions is important. In one of the prototypical mass-imbalanced alkali systems, the Li-Cs mixture, a factor of 22 differing gravitational potentials lead to spatial shifts of atomic cloud positions with respect to each other, which, in the extreme, case may result in a complete spatial separation . This, so called gravitational sag can be compensated or at least reduced by creating species-selective

potentials that influence each of the species independently, or at least differently[7]. In the simplest form it is achieved by engineering a bichromatic trapping potential, created by overlapping optical dipole traps with two distinctive wavelengths, which ensures atom cloud overlap for much lower optical potential depths. This is the approach that we also follow in our experiment. Initially, it has been implemented by Häfner [2013], and is extended during this work.

In this section we discuss our approach for the preparation of ultracold ensembles of Li and Cs atoms in a specific scattering channel with temperatures around 100 nK, especially focusing on gravitational sag compensation. We start by discussing the few crucial components of species-selective optical potentials and introduce our approach for creating bichromatic trapping potential for Li and Cs atoms in Sect. 3.3.1. Afterwards, we present the experimental approach and timing diagrams that are employed for the preparation of Li-Cs mixture in Sect. 3.3.2. This timing sequence is employed to observe the temperature dependence of the Efimov spectrum that is discussed in Sect. 3.4 and explore the finite-range effects in chapter 4.

3.3.1 Bichromatic optical-dipole trap

The optical dipole force arises from the interaction of the induced electric dipole moment with the intensity gradient of the light field. The interaction between a neutral particle with a complex polarizability $\alpha(\omega)$ and the intensity distribution $I(\vec{r})$ of a light field with the angular frequency ω leads to the formation of potential $U_{\mathrm{dip}}(\vec{r},\omega) = -\Re(\alpha(\omega))\, I(\vec{r},)/(2\epsilon_0 c)$, which is used to trap the atoms. The particles scatter photons from the light field with rate $\Gamma_{\mathrm{sc}}(\vec{r},\omega) = \Im(\alpha(\omega))\, I(\vec{r})/(\hbar\epsilon_0 c)$, where ϵ_0 and c stands for the vacuum permittivity and speed of light, respectively. The final trapping potential for each of the species is determined by the two main quantities, the light intensity distribution, and the wavelength dependent complex polarizability[8]. At the same time, the same two quantities govern light-induced heating due to photon scattering, which may limit the achievable stationary temperatures when working with ultracold atoms. Therefore, we start by shortly discussing the wavelength dependence of the complex polarizability specifically for Li and Cs atoms, and then introduce the experimental setup and considerations that are required for gravitational sag compensation at temperatures below 250 nK.

The calculated real part of the complex polarizability for Li and Cs atoms in the electronic ground state for a selected near-infrared wavelength region is given in the

[7] In the author's opinion, the most elegant way, but by far neither the easiest nor the cheapest one, of compensating the graviational sag would be to perform the mentioned ultracold mixed species experiments in gravity-free environment, to which a low Earth orbit of, say, 400 km height might be an excellent candidate.

[8] In fact, these expressions are valid for any polarizable neutral particle in an oscillating electric field, see [Grimm et al., 2000].

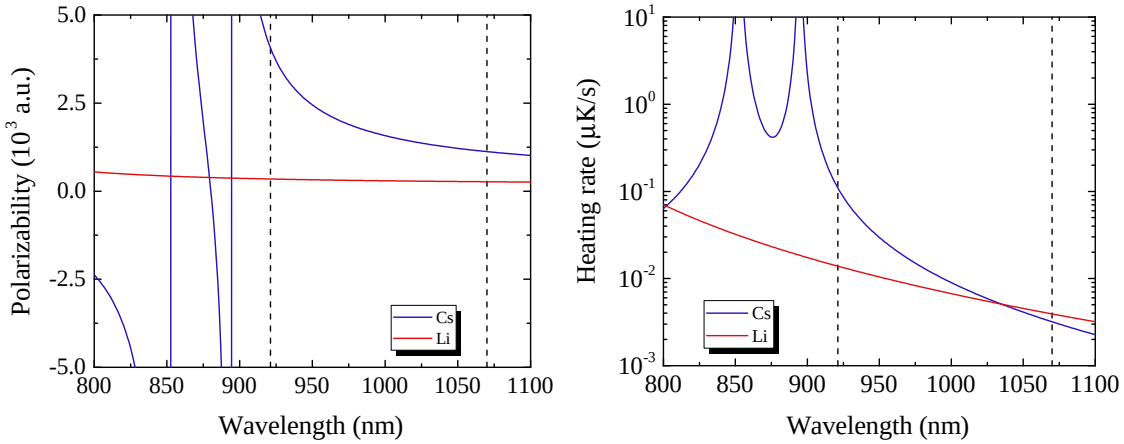

Figure 3.5: Polarizability (left panel) and heating rates (right panel) for Li (red lines) and Cs (blue lines) atoms. For the calculation of the heating rates a typical light intensity of 10^4 W/cm^2 was used. The dashed lines correspond to the laser wavelengths of 1070 nm and 921.2 nm that are used for the generation of the confining potential in our experiment.

left panel of Fig. 3.5. We have used the semiclassical approach and assumed that saturation effects can be neglected [Häfner, 2013; Grimm et al., 2000]. In the case of pure optical-dipole force, the depth of the confining potential would be proportional to the polarizability. While the Li atom polarizability is approximately constant over this range, two pronounced resonances corresponding to the D1 (894.6 nm) and D2 (852.3 nm) lines of Cs are visible. Depending on the exact wavelength of the dipole trap laser this tunability can be employed to generate both, attractive or repulsive potentials with almost arbitrary depth[9], opening up the possibility for the exploitation of various schemes for gravitational sag compensation, one of which is discussed below. At the wavelength of 880.25 nm the polarizabilities of Cs D1 and D2 lines cancel each other, yielding $U_{dip}^{\mathrm{Cs}} = 0$. This is called the *tune-out* wavelength, and allows one to generate single-species selective optical potentials [LeBlanc and Thywissen, 2007].

The major contribution of the imaginary part of the complex polarizability is its induced heating due to continually scattered photons, which leads to the increase of ensemble's thermal energy. Even if the polarizability is zero, continuous absorption and re-emission of far-detuned photons lead to heating. For a spatially averaged scattering rate $\bar{\Gamma}_{sc}$ in a three-dimensional harmonic trap, the wavelength dependent heating rate $\dot{T}$ is given by $\dot{T} = T_{\mathrm{rec}}\bar{\Gamma}_{sc}/3$, where $T_{\mathrm{rec}} = \hbar^2 k^2/m$ is the recoil temperature, associated with the kinetic energy gain by emission of single photon with a wavenumber k [Häfner, 2013; Grimm et al., 2000]. For Cs and Li atoms it is shown

[9] The maximal trap depth is limited by the saturation of the optical transition and intensity of the light.

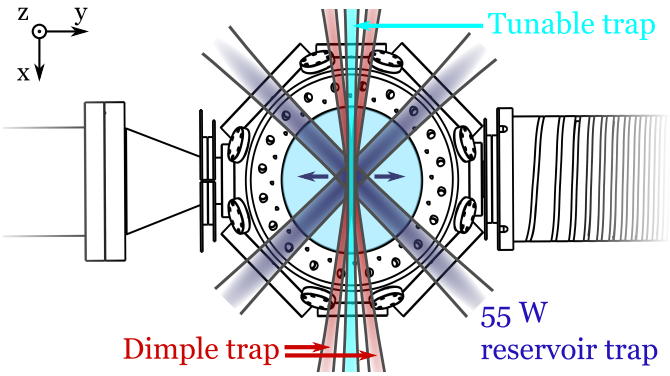

Figure 3.6: Laser beam configuration of the optical dipole traps around the main experimental chamber. The crossing region of the reservoir trap beams (blue) can be shifted along the y axis with a piezo mirror, and is employed for optical transport of Cs atoms (see Sect. 2.3.1 and 3.3.2) to the position of the dimple trap (red). The single tunable trap beam (cyan) is aligned along the longitudinal symmetry axis of the cigar shaped dimple trap, and is used for compensation of the gravitational sag of Cs atoms. The given coordinate system is used for all the calculations and graphs presented throughout this chapter. Adapted from [Repp, 2013].

in the right panel of Fig. 3.5. In analogy with the real part of the complex polarizability, the heating rate of Li changes only gradually, while for Cs it shows two pronounced maxima at the positions of the D1 and D2 atomic transitions. Since this may limit the achievable atom lifetime in the trap, for experiments close to quantum degeneracy it is beneficial, if possible, to choose the wavelength far away from any strong optical transition.

Ensuring sufficient spatial overlap of ultracold clouds of Li and Cs atoms is not straightforward due to the different trapping potentials each of the species experience. The experimental setup that was employed for the preparation of Li-Cs mixtures at 400 nK temperatures, and is discussed in Sect. 2.3.1, is using a monochromatic optical dipole trap, in which a complete spatial separation of the Li and Cs atom clouds would take place at around 200 nK. In the bichromatic trap that is presented in this section, the temperature could be reduced to 100 nK, while still retaining sufficient spatial overlap between the atom clouds.

Therefore, let us start by briefly introducing the single-wavelength optical dipole trap (ODT) approach that was used for in chapter 2 presented experiments and is extensively described in Refs. [Heck, 2012; Repp, 2013; Arias, 2014; Pires, 2014]. In short, the mixture of Li and Cs atoms is trapped in a crossed beam ODT, referred to as a dimple trap, with a wavelength of 1070 nm, $1/e^2$ waist of ≈ 62 μm, and a crossing angle of 8.5°. A schematic configuration of our complete ODT setup with respect to the experimental chamber is shown in Fig. 3.6 (the single-wavelength

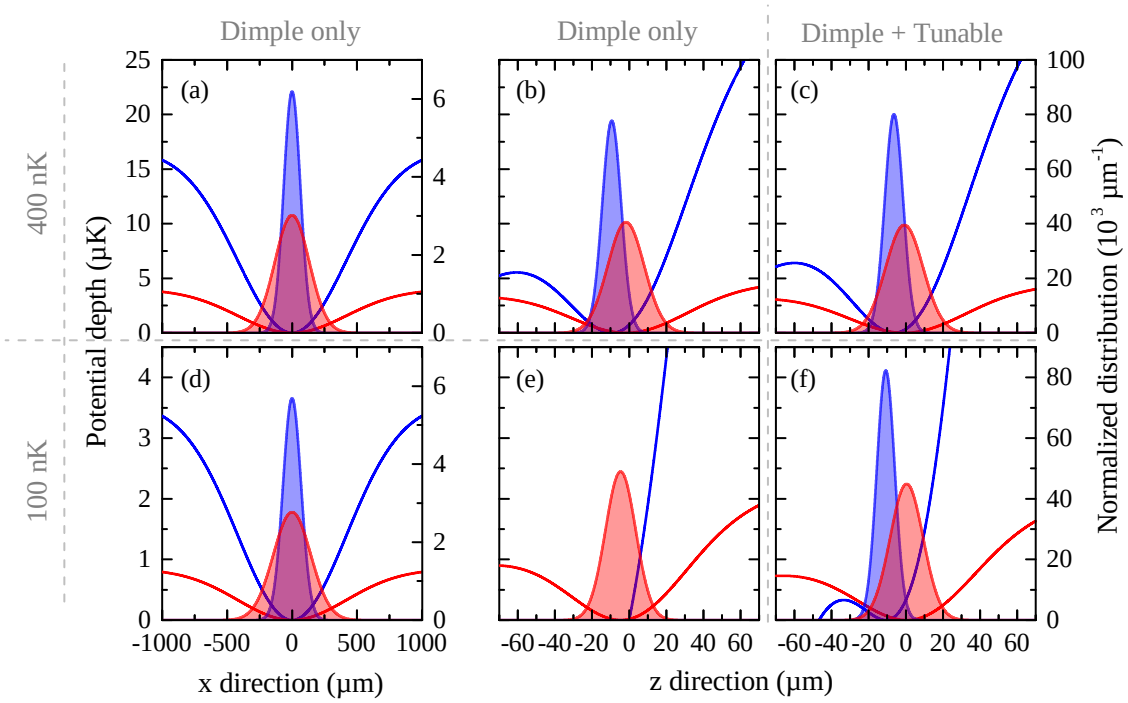

Figure 3.7: Total trapping potentials for ground state Li (red) and Cs (blue) atoms at the experimentally determined temperatures of 100 nK and 400 nK, and their corresponding distributions. (a) and (d). Along the longitudinal axis of the trapping potential in the horizontal direction (x direction in Fig. 3.6) the spatial overlap of the atom distributions is independent of the temperature. (b) and (e). Total potentials with the dimple trap. The spatial overlap at 400 nK is already reduced to $\sim 80\%$, while at 100 nK the Cs atoms are not confined anymore due to the gravitational potential. (c) and (f). Total potentials in the bichromatic configuration restores the confining potential. At a temperature of 100 nK the intensity of the dimple trap and the tunable trap is $3.5{\times}10^3$ mW/mm^2 and $3.1{\times}10^3$ mW/mm^2, respectively. The relative displacement between the centers of the Li and Cs atom distributions is 16 ± 5 μm, resulting in a spatial overlap of $\sim 33\%$.

configuration corresponds to dimple and reservoir traps only). The atomic polarizabilities at this wavelength differ by a factor of four, and, as long as the ODT generated potential is dominating over the gravitational potential, the trap depth is different by about the same factor, namely, $U_{\mathrm{dip}}^{\mathrm{Cs}} \approx 4U_{\mathrm{dip}}^{\mathrm{Li}}$. This is also reflected in the unlike temperatures that are attained in this regime during forced evaporation [Repp et al., 2013; Repp, 2013].

Once the intensity of the dimple trap is lowered, the influence of gravitational potential becomes significant. Fig. 3.7(a,b,d,e) illustrates this. The spatial overlap of the normalized Li and Cs atom distributions along the longitudinal symmetry axis of the cigar shaped trapping volume (corresponds to the x axis in Fig. 3.6)

remains independent of the ODT potential depth. However, the influence of the larger Cs mass is evident along the gravitational axis (corresponds to the z axis in Fig. 3.6), as shown in Fig. 3.6(b). For a dimple power that produces a Li-Cs mixture at about 400 nK (also used for the labeling of the different trapping situations[10]), the Li trapping potential is largely unaffected by the gravity, while Cs potential develops a steep slope, that rapidly reduces the effective trapping depth. The fact that the depths of the confining potentials are more similar in this situation, is also indicated by the experimentally determined temperatures, which are approximately equal for both of the species and yields ~ 400 nK. If the light intensity was reduced furthermore, corresponding to, for example, forced evaporation, the optical potential would become negligible in comparison to the gravitational potential, and Cs atoms would not be confined anymore, which is evident in Fig. 3.7(e). At this point, it is important to note that for a light intensity range between the Cs trapping potential is lost and the situation when the species temperatures are similar, the trap depths of the confining potentials are inverted, i.e. Li atoms are captured in a deeper trap, although the polarizability of Cs atoms is a factor of four higher than that of Li atoms.

We overcome the loss of Cs confinement potential by the addition of a single, focused laser beam along the symmetry axis of the cigar shaped trapping volume that we call the tunable trap (see Fig. 3.6). The laser beam is generated by a tunable Ti:sapphire laser. In order to retain the overall shape of the optical potential, the additional beam has an $1/e^2$ waist of 62 μm, which is comparable to the radial size of the crossed dimple trap. Since the temperature after forced evaporation is approximately related to the trapping depth, the final trap depths for Li and Cs atoms should be approximately similar. The polarizability of Cs at this wavelength should be much larger than that of Li, while keeping the heating rate to minimum. Such a situation is achieved for the wavelength of 921.2 nm, at which the atomic polarizabilities of Cs ($\alpha_{\mathrm{Cs}} \approx 4059$ a.u.) and Li ($\alpha_{\mathrm{Li}} \approx 345$ a.u.) differ by a factor of 12. The additional optical dipole potential in combination with the dimple trap restores the trapping potential for Cs atoms, as shown in Fig. 3.7(f).

An optimal choice of the tunable trap wavelength and spatial offset along the gravity axis is not trivial. Although the tunable trap provides with largely independent control over the spatial position of Cs atoms, it generates a residual optical potential for Li atoms that also increases the depth and slightly shifts the minimum position of their confining potential. In fact, for a particular choice of the tunable dipole trap wavelength and offset along the gravity axis (z axis in Fig. 3.6 and 3.7), the intensities of the dimple trap and the tunable trap can be adjusted in such a way

[10]The temperature and the trap depth of the confining potential are approximately related through the expression $U_{dip} \approx \eta k_B T$ [Ketterle and van Druten, 1996]. In our experiment we typically observe $\eta_{\mathrm{Cs}} \sim 5$ [Pires, 2014] and $\eta_{\mathrm{Li}} \sim 10$ [Heck, 2012].

that the effective trapping depths for Cs and Li atoms are equal. This is important for most of our experiments because the temperatures of the atom clouds should be similar, but at the same time the differential sag between both species needs to be minimized. According to our calculations, partial to complete compensation of the gravitational sag can be achieved at least in the range between 910 nm and 930 nm for the employed trapping geometry. The former ensures that the trap depths are equal at lower light intensities at the expense of a larger heating rate, whereas the latter results in the opposite. The wavelength of 921.2 nm is chosen and optimized experimentally[11], and represents a compromise between sufficient differential polarizability between Li and Cs atoms, and small heating rate, which creates equally deep confining potentials for both species at a trap depth of around 700 nK.

The final confining potential configuration, in which the experiments that are discussed in this work was performed, retains a residual gravitational sag of 16 ± 5 μm between the center positions of the atom density distributions along the gravity axis of the cylindrically shaped trapping potentials (see Fig. 3.7(f)). This configuration is created by displacing the laser beam of the tunable trap by 25 μm in the z direction, and yields an estimated spatial overlap of $\sim 45\%$ between the atom clouds. The spatial overlap has been reduced in favor of complete compensation of the sag in order to increase the observation time of three-body loss dynamics. In general, this is beneficial in the vicinity of an interspecies FR, since the experimentally measurable loss rate K_3 can be optimized for better observation, while L_3 is given by the temperatures and interaction strength, as shown in Eq. (3.28).

3.3.2 Experimental procedure for the sample preparation at 100 nK

The overview of the experimental sequence for the preparation of the Li-Cs mixture at temperatures down to 100 nK is given in Fig. 3.8. Initially it approximately follows the timing diagram for the sample preparation at a temperature of 450 nK that was explained in Sect. 2.3.1. It starts with a similar Cs and Li MOT loading sequences, DRSC phase and loading into the reservoir and dimple traps. The most significant differences at this point are the MOT loading times and the initial reservoir trap power, which have been experimentally optimized to yield the maximum number of Li and Cs atoms at the end of the complete preparation sequence.

In analogy to the preparation procedure at 400 nK, after the loading of the reservoir and dimple trap, we set the homogenous offset field to $B_{evap} \approx 898$ G and perform simultaneous forced evaporation in still spatially separated traps by linearly decreasing optical power in each of the traps for approximately 3 s. At this

[11] Cs_2 photoassociation lines, and two-photon transitions are also found in this wavelength range. Parasitic heating effects from them were observed during this work, but are not discussed here.

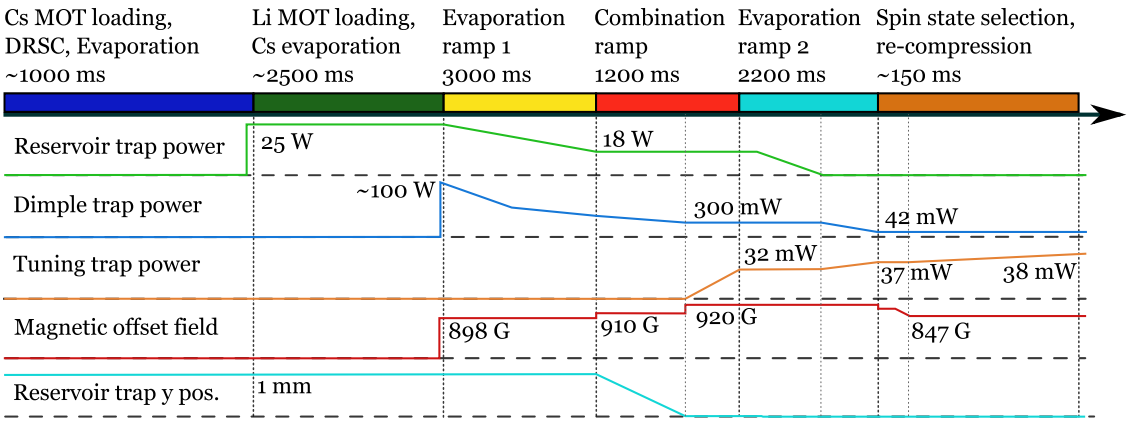

Figure 3.8: Typical experimental sequence for the preparation of a Li-Cs mixture at a temperature of 100 nK in channel $|\alpha\rangle$. Schematic representation of values and timings of selected parameters. The major part of the timing diagram it is identical for both of the employed Li-Cs scattering channels $|\alpha\rangle$ and $|\beta\rangle$ (see Eq. (2.11) for the definition). The final spin state selection takes place during the first ∼20 ms of the last timing block (see text).

point, we switch the magnetic field to 910 G, stop the evaporation ramp for Cs in the reservoir trap, and superimpose it with the dimple trap in a 800 ms long ramp. Once the traps are overlapped, we turn on the tunable trap by ramping its power from zero to about 32 mW in a 400 ms long ramp. The Li and Cs atoms that remain in the reservoir trap can now be employed as a cooling agent for the ones in the bichromatic trap. The last evaporation ramp of is performed at a magnetic field of 920 G, by initially ramping down the power of the reservoir trap down to zero in a 1000 ms long ramp, and followed by combined evaporation ramp in the bichromatic trap, during which we decrease (increase) the power of the dimple (tunable) trap laser beam to 42 mW (37 mW).

The mixed sample in the bichromatic trap now consists of Cs atoms in spin state $|3,+3\rangle$ and Li atoms in spin states $|1/2,+1,2\rangle$ and $|1/2,-1/2\rangle$. We shine in a laser light pulse that is resonant with the D2 transition of the Li$|1/2,+1/2\rangle$ spin state to remove it from the sample, and switch the magnetic field to 893 G. The mixture now populates the single scattering channel $|\beta\rangle$, and can be used for the experiments close to the 889 G Li-Cs Feshbach resonance. In order to prepare the mixture in the other Li spin state $|1/2,+1,2\rangle$, we drive a rapid adiabatic passage by ramping the magnetic field down to 847 G in a 4 ms long ramp, while applying a 2 ms long radio-frequency pulse at 76.3189 MHz. This transfers the complete population into the other scattering channel $|\beta\rangle$, which is the starting point for the measurements close to the 843 G Li-Cs Feshbach resonance. After a slight re-compression of the tunable trap in 150 ms that stops the residual evaporation, but increases the final temperature to about 100 nK, we are left with about 7×10^3 Li and 1×10^4 Cs atoms

in the necessary scattering channel. During this hold time the residual magnetic field fluctuations due to switching with large amplitude steps have stabilized (see the discussion in Sect. 2.3.2). The measured secular trapping frequencies (f_x, f_y, f_z) at these conditions yield (5.7, 125, 85) Hz and (25, 180, 160) Hz for Cs and Li atoms, respectively, where the external magnetic field is parallel to the z axis.

3.4 Observation of $LiCs_2$ Efimov resonances

The most straightforward approach to probe the Efimov scenario is atom-loss spectroscopy, identical to the one used for detecting Feshbach resonances. In this case Efimov resonances emerge as additional modulations at the side of the loss-feature of the Feshbach resonance in atom-loss spectra. While such spectra represent already strong hints for the existence of three-body Efimov resonances, and their positions can be approximately detected, it does not yield the exact composition of the number of lost particles during a recombination event. For this purpose the time evolution of the atom number of each species in the mixture can be recorded, from which extracted loss rate coefficients characterize the recombination process and can be compared to theoretical predictions. We discuss our implementation of both of these methods for the detection of LiCsCs Efimov resonances in the following sections.

3.4.1 Atom-loss spectra

We start our investigation of $LiCs_2$ Efimov resonances by atom-loss spectroscopy. We use the approach described in Sect. 2.3.1 to prepare a Li-Cs mixture in the scattering channel $|\alpha\rangle$ around 943 G. After the plain evaporation has nearly ended, we switch the magnetic field in a random order to various values close to the FR at 843 G and observe the number of remaining atoms after a predetermined hold time.

These measurements are summarized in Fig. 3.9. The three-body loss coefficient L_3 for collisions between two identical bosons and one distinguishable particle in the vicinity of a FR scales as a_{LiCs}^q, where the power q can take values from 2 to 4 depending on the number of resonant interactions and their sign [D'Incao and Esry, 2009]. This gives rise to the large loss feature associated with the increasing inelastic three-body collisional cross section. The atom losses closer to the pole of the scattering resonance occur faster, thus the hold time is decreased from 1 s to 400 ms for the measurements shown in Fig. 3.9(b) and 3.9(a), respectively. In addition to the global loss maximum slight modulations around three magnetic field values are visible, which in further atom-loss rate experiments are identified as $LiCs_2$ Efimov resonances (see Sect. 3.4.2). Their positions are determined by fit of a Gaussian profile with a linear background to each feature. It results in $B_0 = 849.12(6)(3)$ G, $B_1 = 844.89(1)(3)$ G, and $B_2 = 843.03(5)(3)$ G for the positions of the Efimov

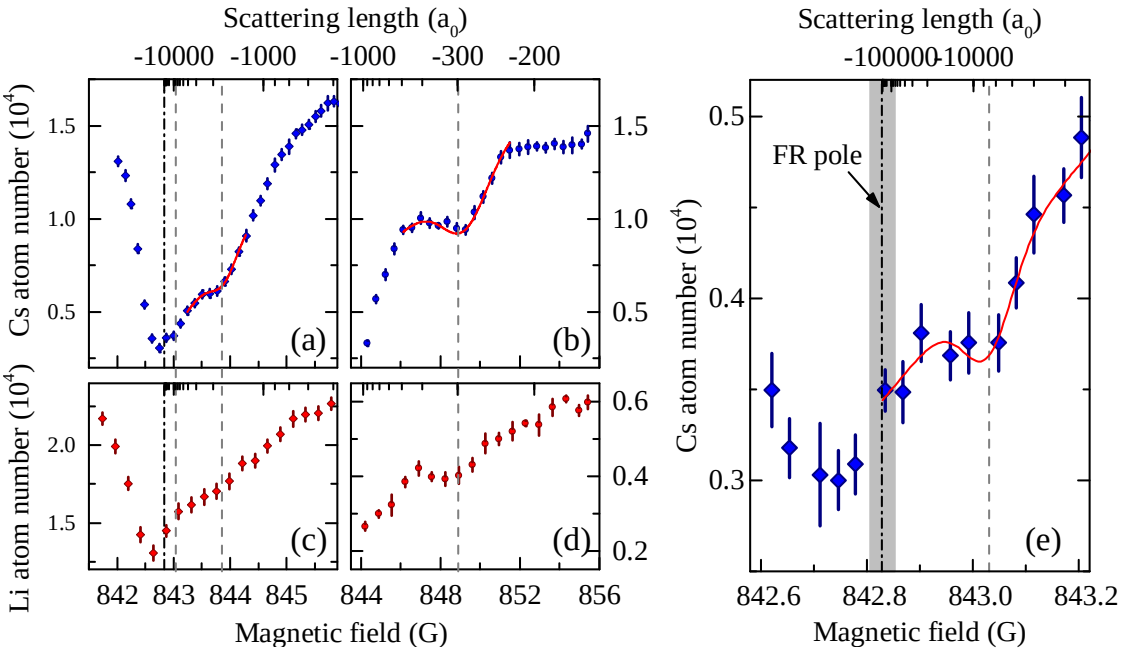

Figure 3.9: Atom-loss spectra of $LiCs_2$ Efimov resonances at a temperature of 450 nK. (a), (b), and (e) shows the remaining number of Cs atoms as a function of the magnetic field after a hold time of 400 ms and 1 s, respectively. The two pronounced modulations indicate the positions of the first and second Efimov resonances, and the third one can be seen in (e). The loss spectra of Li atoms in (c) and (d) show resonances at consistent positions after a hold time of 1.2 s, once the initial Li atom number is reduced by approximately a factor of two as compared to Cs. Each data point is the mean of at least six measurements, and the error bars represent the standard error. The positions of Efimov resonances are indicated by the dashed lines, which are extracted from a fit of Cs atom number to a Gaussian profile with linear background (red solid lines). The dash-dotted line and the gray area around it gives in Sect. 2.4 extracted pole position of the Feshbach resonance and its uncertainty, respectively.

resonances, where the value in the first parenthesis denotes standard error of the fit, and the second error is the systematic uncertainty of the absolute magnetic field. Note, that for these experiments the magnetic field uncertainty is 30 mG, larger than for both rf association of LiCs dimers, and loss rate measurements at 120 nK.

According to the Pauli principle, we expect that the dominant loss process in the mixture is the three-body recombination, in which a pair of Cs atoms and a single Li atom are lost from the trap. Therefore the same atom loss behavior is expected to manifest not only for Cs atoms, but also for Li. Under the experimental conditions of the measurements in Fig. 3.9(a) and 3.9(b) the relative loss fraction of Li atoms at the Efimov resonance positions is too small to be discerned from atom number fluctuations caused by the instabilities of the experiment. The reason is that for these experiments the number of Li atoms in the mixture is almost a factor two

larger than the Cs one. In the case of a complete loss of Cs atoms due to Li-Cs-Cs collisions, there would be three quarters of the initial number of Li atom left. Hence, we reduce the number of Li atoms by a factor of about two in comparison to the previous measurements, which recovers the modulations as demonstrated in Fig. 3.9(c) and 3.9(d) for hold times of 1.2 s. This and the much slower timescales, at which the Li losses are occurring, already hints that our argumentation about the predominant loss process being the one between a single Li atom and two Cs atoms is correct. This is also in accordance with the Pauli principle reducing the likeliness of finding two identical Li atoms at sufficiently close distances for three-body recombination to occur. These assumptions are investigated more quantitatively in the next section by three-body loss rate measurements.

3.4.2 Determination of three-body loss rates

While atom-loss spectra represent already strong hints for the observation of $LiCs_2$ Efimov resonances, it does not yield the exact composition of the lost particles during the recombination process. For this purpose the time evolution of the number of atoms in the mixture during the hold time can be recorded and analyzed. It is closely related to the time evolution of the number densities n_{Li}, and n_{Cs} of Li and Cs atoms, which is given by the coupled rate equations

$$\dot{n}_{\mathrm{Cs}} = -L_1^{\mathrm{Cs}} n_{\mathrm{Cs}} - 2L_3 n_{\mathrm{Li}} n_{\mathrm{Cs}}^2 - L_3^{\mathrm{Cs}} n_{\mathrm{Cs}}^3, \tag{3.23}$$

$$\dot{n}_{\mathrm{Li}} = -L_1^{\mathrm{Li}} n_{\mathrm{Li}} - L_3 n_{\mathrm{Li}} n_{\mathrm{Cs}}^2, \tag{3.24}$$

where $L_1^{\mathrm{Cs,Li}}$ and L_3^{Cs} denotes single-body and three-body loss rates, respectively, for samples consisting of purely Li or Cs atoms, as indicated by the upper index. The three-body loss rate L_3 corresponds to Li + Cs + Cs inelastic collisions, which also contains in Sect. 3.2.3 introduced functional form of the three-body recombination resonances. Here we have neglected inter- and intraspecies two-body losses, since the atoms are prepared in the energetically lowest scattering channel and thus only elastic binary collisions are possible. Also, we do not consider inelastic three-body losses due to Li+Li+Li collisions as this process is strongly suppressed due to Fermi statistics and the probability of finding three Li atoms at close distances is small[12]. Finally, the temperature of the mixture remains constant within the experimental uncertainties of our temperature determination ($\sim 15\%$), thus we do not include the third differential equation associated with the recombinational heating [Weber et al., 2003; Roy et al., 2013; Bloom et al., 2013]. The absence of any temperature increase might be caused by residual plain evaporation that compensates the heating. At

[12]Typical lifetimes of Li gas prepared in a single spin channel in our experiment is on the order of 1 minute in the magnetic field range between 800 G and 1000 G.

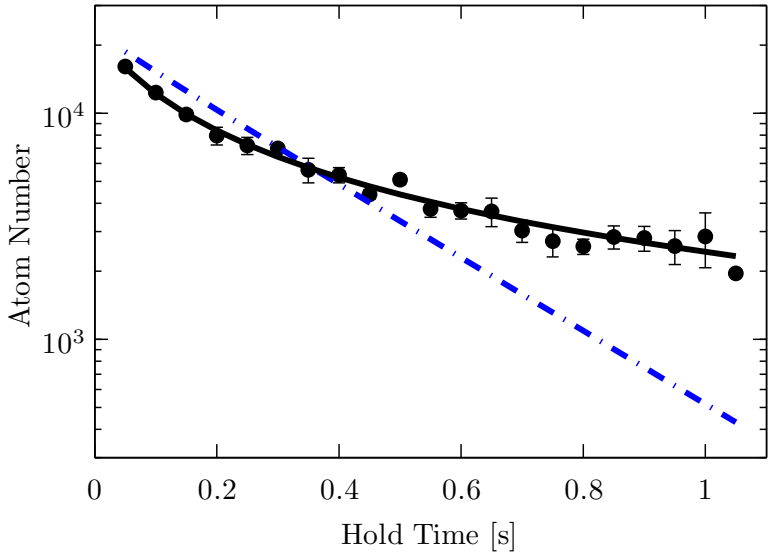

Figure 3.10: Temporal evolution of Cs atom number in a Li-Cs mixture at 843.9 G magnetic field and 450 nK temperature. Each data point represents the mean of at least five independent measurements and the error bars are given by one standard error. The black solid and blue dash-dotted lines show the results of a fit of Eq. (3.23) to data, where either Li + Cs + Cs or Li + Li + Cs interspecies three-body losses have been included, respectively. In the latter case, the second term in the rate equation is replaced by $L_3 n_{\mathrm{Li}}^2 n_{\mathrm{Cs}}$. Figure adapted from [Pires, 2014].

the same time this allows to directly link the change in the density with the change of the observed number of atoms.

The number densities $n_{\mathrm{Cs,Li}}$ are experimentally difficult accessible quantities, therefore in our measurements we record the temporal evolution of the atom numbers, as shown in Fig. 3.10. The equivalent system of differential equations describing this decay process is obtained by spatial integration of Eqs. (3.23) and (3.24), which yields

$$\dot{N}_{\mathrm{Cs}} = -L_1^{\mathrm{Cs}} N_{\mathrm{Cs}} - 2K_3 N_{\mathrm{Li}} N_{\mathrm{Cs}}^2 - K_3^{\mathrm{Cs}} N_{\mathrm{Cs}}^3, \tag{3.25}$$

$$\dot{N}_{\mathrm{Li}} = -L_1^{\mathrm{Li}} N_{\mathrm{Li}} - K_3 N_{\mathrm{Li}} N_{\mathrm{Cs}}^2. \tag{3.26}$$

Here, each of the rates K_3 and K_3^{Cs} already incorporate a numerical factor that originates from the particular shape of atom density distribution in the trapping potential. For a Gaussian distribution with a width σ_i along the coordinate axis $i = x, y, z$, they are connected to the three-body loss rates given by Eqs. (3.23)

and (3.24) via equations

$$L_3^{\mathrm{Cs}} = 24\sqrt{3}\pi^3 K_3^{\mathrm{Cs}} \prod_{i=x,y,z} \sigma_{i,\mathrm{Cs}}^2 \tag{3.27}$$

and

$$L_3 = 8\pi^3 \exp\left[\frac{z_0^2}{2\sigma_{z,\mathrm{Li}}^2 + \sigma_{z,\mathrm{Cs}}^2}\right] K_3 \prod_{i=x,y,z} \sigma_{i,\mathrm{Cs}} \sqrt{2\sigma_{i,\mathrm{Li}}^2 + \sigma_{i,\mathrm{Cs}}^2}, \tag{3.28}$$

where $\sigma_i = \sqrt{k_B T/m}/(2\pi f_i)$ is given by the sample temperature T and trapping frequencies f_i. Here, m is the mass of the atomic species and k_B denotes the Boltzmann constant. We have explicitly included a displacement z_0 between the centers of the atomic distributions of Li and Cs along the z-axis. It mimics the effect of gravitational sag, causing separation of the atom clouds, and consequently, smaller experimentally observable K_3 rates.

We extract K_3 and K_3^{Cs} rates, given by Eqs. (3.25) and (3.26), directly from our experiments by a numerical fitting procedure. The determination of L_3 and L_3^{Cs}, which are the quantities that can be compared to the theory, relies on Eqs. (3.27) and (3.28), which introduces additional systematic errors due to finite knowledge of the sample temperature, trapping frequencies, and finite overlap in the gravitational potential. For typical experimental uncertainties the systematic error of the absolute value of L_3 and L_3^{Cs} can reach 80% for the measurements at 450 nK temperatures, and a factor of three for the measurements at 120 nK temperatures.

An exemplary measurement of the atom number time evolution is depicted in Fig. 3.10 at the temperature of 450 nK. For these experiments the initial number of Li atoms in the mixture is roughly twice the Cs one. As already mentioned, this leads to much larger fraction of lost Cs atoms than Li. In fact, we loose almost 90% (30%) of the Cs (Li) atoms for typical hold times on the order of a few seconds. Thus the density of the Li atoms in the mixture can be assumed to be constant during the complete time evolution[13]. The rate equation (3.26) (Eq. (3.24)) can be neglected and the complete Cs atom loss are described by the equation (3.25) (Eq. (3.23)), which we use for the further analysis.

The fit of the rate equations allows us to verify the dominating three-body loss process in the mixture. Fig. 3.10 shows a comparison between the numerically fitted loss rates by assuming Li + Cs + Cs or Li + Li + Cs three-body recombination as the only interspecies loss processes. This is achieved by the substitution $K_3 N_{\mathrm{Li}} N_{\mathrm{Cs}}^2 \rightarrow K_3 N_{\mathrm{Li}}^2 N_{\mathrm{Cs}}$, while keeping the other terms in Eq. (3.25) constant. It is obvious that the time evolution is excellently described by the recombination of two Cs and one Li atom. The opposite process, involving two Li and one Cs atoms, fails to reproduce

[13]The number of Li atoms at any point during the hold time is larger than the one of Cs, hence the situation is analogous to Cs atoms being immersed in a large "reservoir" of Li atoms.

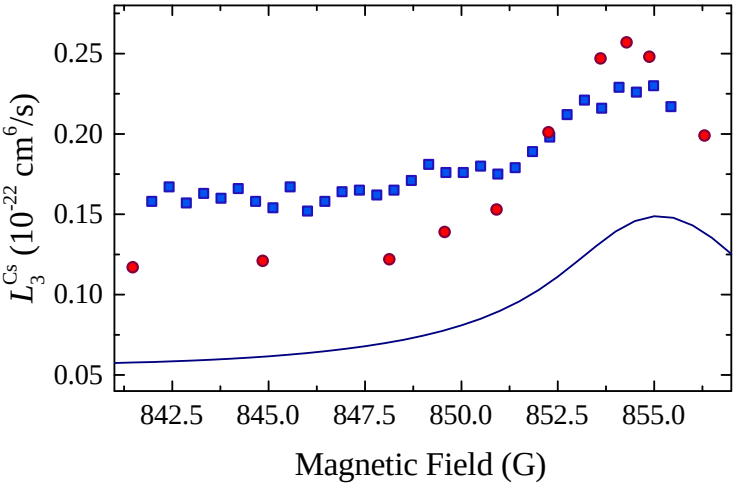

Figure 3.11: Cs intraspecies three-body loss coefficient at a temperature of 410 nK (blue squares). For comparison, data independently measured by the group in Innsbruck at 330 nK is shown [Huang and Grimm, 2014]. The solid line depicts a calculation based on the finite temperature model of Ref. [Rem et al., 2013] for 410 nK. It is within our systematic uncertainty of $\sim 80\%$. The feature around 854 G is due to Cs_3 Efimov resonance [Berninger et al., 2011, 2013].

the shape of the decay curve, thus verifying that it is strongly suppressed due to Pauli blocking. This confirms that the Efimov resonances indeed originate from the Li + Cs + Cs scattering channel, which is the only one channel for this mixture that is predicted to support universal three-body bound states [Braaten and Hammer, 2006; D'Incao and Esry, 2006]. The same conclusion is supported by the observation that the loss ratio of Li to Cs atom numbers is approximately 1:2 in the entire range of the probed magnetic fields.

The number of free fitting parameters in Eq. (3.25) is reduced further by separate measurements of the single species one-body and three-body loss rates $L_1^{\mathrm{Cs,Li}}$ and L_3^{Cs}, respectively. For these measurements a single species sample in the same spin state with similar initial temperature and trapping frequencies is prepared, and the remaining number of atoms as a function of the hold time in the optical dipole trap is recorded for a magnetic field range, in analogy with the mixed species experiments. The results for a typical magnetic field dependence of L_3^{Cs} is shown in Fig. 3.11. The loss rate is almost constant in the magnetic field range between 842 G and 852 G, and exhibits a pronounced maximum around 854 G, which is caused by Cs_3 Efimov resonance [Berninger et al., 2011, 2013]. The absolute value is consistent with the finite temperature model[14] of Ref. [Rem et al., 2013], and independent measurements performed at a temperature of 330 nK from Innsbruck [Huang and Grimm, 2014].

[14]This calculation was performed by Bo Huang, Universiy of Innsbruck, Austria [Huang and Grimm, 2014].

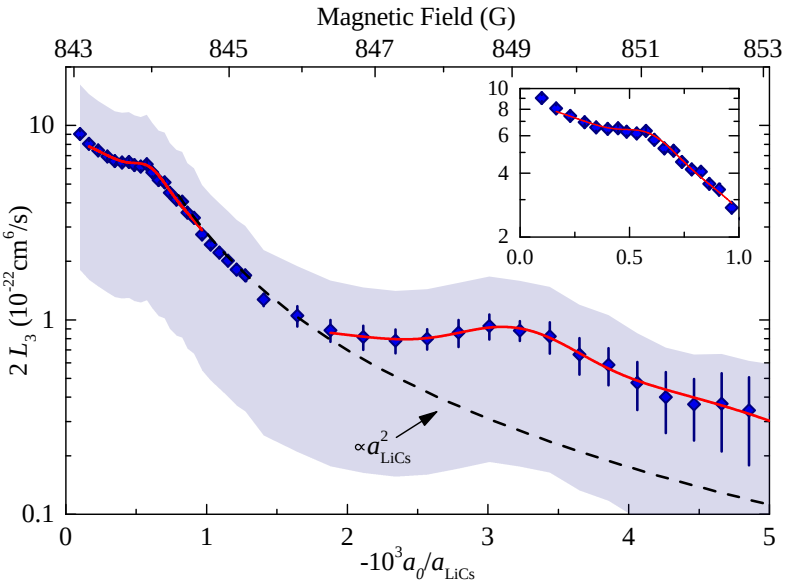

Figure 3.12: Li-Cs three-body recombination spectrum close to the 843 G Feshbach resonance. Each data point is the mean of three independent L_3 determinations, and the error bars represent one standard error of the mean. The Efimov resonance positions are extracted by a fit (solid lines) of a Gaussian profile with a linear background to the data. The shaded area illustrates the systematic error of the absolute value of L_3. The first excited Efimov resonance is shown in the inset. The $\propto a^2_{\mathrm{LiCs}}$ scaling is drawn as a guide to the eye (dashed line).

The differences between the three datasets are well within our systematic uncertainties, originating due to extraction of the absolute value of L_3^{Cs} via Eq. (3.27). For the analysis and fitting of interspecies three-body loss rate L_3 we use the average $\tilde{L}_3^{\mathrm{Cs}} = 1.67 \times 10^{-23}$ cm^6/s in the magnetic field range between 842 G and 852 G as a fixed parameter. The one-body loss rate of Cs atoms is also extracted from the same measurements and yields $L_1^{\mathrm{Cs}} = 0.04$ s^{-1}.

As a result, the determination of the Li-Cs three-body loss rate is reduced to a single parameter fit of Eq. (3.25) to data, demonstrated already in Fig. 3.10, and subsequent calculation of L_3 via Eq. (3.28). In this way obtained magnetic field dependence is shown in Fig. 3.12, and reveals two pronounced features that we identify as $LiCs_2$ Efimov resonances, according to the employed rate equation model. For large values of the Li-Cs scattering length the absolute value of L_3 approaches an order of magnitude estimation of the unitarity limit, given by [D'Incao and Greene, 2014; Petrov and Werner, 2015]

$$L_3^{\mathrm{un}} = \frac{4\pi^2\hbar^5}{\mu_3^3\,(k_B T)^2}, \tag{3.29}$$

where μ_3 is the three-body reduced mass from Eq. (3.6). For the temperature of $T = 450$ nK it yields $L_3^{\mathrm{un,450nK}} = 3.8 \times 10^{-22}$ cm^6/s, in excellent agreement with the data.

The overall scaling of the loss rates with the scattering length approximately follows $\propto a_{\mathrm{LiCs}}^2$ dependence, as expected for a heavy-heavy-light mixture with large background scattering length, such that $|a_{\mathrm{LiCs}}| \ll |a_{\mathrm{Cs}}|$ [D'Incao and Esry, 2009]. In this magnetic field range $a_{\mathrm{Cs}} \sim -1400a_0$, thus the proportionality is expected to hold to about $-10^3 a_0/a_{\mathrm{LiCs}} \sim 1$. As can be seen in Fig. 3.12, the agreement in this range is excellent. The relation is weakened as a_{LiCs} approaches the pole of the FR because of the unitarity limit, and also because now a_{LiCs} becomes much larger than a_{Cs}. The scaling laws are discussed in more detail in Sect. 4.3.2.

3.4.3 Simplified analysis of Efimov resonance positions

As a simplified determination of the Efimov resonance positions, we fit a Gaussian profile with a linear background to the resonant features in the L_3 spectrum (Fig. 3.12). The fit yields $B_0 = 848.90(6)(3)$ G and $B_1 = 843.85(1)(3)$ G, to which the scattering lengths are assigned from the FR parametrization obtained in Sect. 2.4.3 by the Eq. (2.21). One obtains $a_-^{(0)} = -311(3)(1)(1)\ a_0$ and $a_-^{(1)} = -1710(20)(50)(40)\ a_0$, where the error in the third parenthesis represents the uncertainty arising from the FR parameter determination. The position of the second excited Efimov resonance from the atom loss-data (Fig. 3.9), which yields $a_-^{(2)} = -8540(2120)(1270)(970)\ a_0$. All errors are obtained by Gaussian error propagation.

The summary of the results obtained in this work and a comparison to independent measurements by Chicago group [Tung et al., 2014] gives consistent results, and is presented in Table 3.1. We list the determined magnetic field values and corresponding scattering lengths $a_-^{(n)}$, at which the $n-$th three-body Efimov state merges with the scattering threshold, and the corresponding scaling factors $\lambda_n = a_-^{(n)}/a_-^{(n-1)}$. The obtained scaling factors of 5.48(7)(16)(10) (this work) and 5.35(24)(16)(10) [Tung et al., 2014] for the first Efimov period are close to the expected value of 4.88 for a zero-temperature gas in the scaling limit ($|a| \gg \bar{a}$) [Braaten and Hammer, 2006; D'Incao and Esry, 2006], however they slightly deviate from the universal prediction. The scaling factor of the second Efimov period lies well within the universal predictions. This is not surprising, since the assumption of the scaling limit is not strictly justified for the ground state Efimov resonance. It emerges at $a_-^{(0)}$ that is only a factor of ~ 7 (~ 3) larger than the LiCs (CsCs) van der Waals length (see Table 4.1). Several theoretical studies have demonstrated that the ground Efimov state can be subject to large modifications due to short range physics [Wang et al., 2012a; Schmidt et al., 2012; Sørensen et al., 2012, 2013a; Thøgersen et al., 2008;

Table 3.1: Positions and scaling factors of $LiCs_2$ Efimov resonances near the 843 G Feshbach resonance. The values in the first and second parenthesis always represent the statistical and systematic error of the Efimov resonance position determination, respectively. For $a_-^{(n)}$ and the scaling factors $a_-^{(n)}/a_-^{(n-1)}$ the error in the third parenthesis denotes the uncertainty arising from the $a(B)$ mapping through the Feshbach resonance parameters given in Sect. 2.4.3.

n	Magnetic field (G)	$a_-^{(n)}$ (10^3 a_0)	$a_-^{(n)}/a_-^{(n-1)}$
0 (ground)	848.90 (6)(3)†	−0.311 (3)(1)(1)	-
1	843.85 (1)(3)†	−1.71 (2)(5)(4)	5.48 (7)(16)(10)
2	843.03 (5)(3)†‡	−8.54 (2.12)(1.27)(97)	5.00 (1.24)(76)(46)
0	848.55 (12)(3)*	−0.329 (6)(2)(1)	-
1	843.82 (4)(3)*	−1.76 (7)(5)(4)	5.35 (24)(16)(10)
2	842.97 (3)(3)*	−12.2 (2.6)(2.6)(1.9)	6.93 (1.50)(1.48)(97)

† This work; ‡ the magnetic field value was determined from atom-loss spectroscopy.
* Ref. [Tung et al., 2014]

Platter et al., 2009; Naidon and Ueda, 2011; Kievsky and Gattobigio, 2013] and even three-body forces [D'Incao et al., 2009a]. Furthermore, the recent experiments of the first excited-state resonance in Cs [Huang et al., 2014b; Wang and Julienne, 2014] and ^{4}He [Kunitski et al., 2015] and the new analysis of ^{6}Li [Huang et al., 2014a] and ^{7}Li [Gattobigio and Kievsky, 2014] data not only hint at deviations from the universal scaling, but also to shifts of the ground-state resonances due to finite range effects. While the origin of these deviations is still an open question for the formerly mentioned systems, for the Li-Cs-Cs system the inclusion of Cs-Cs short range van der Waals interactions already gives much better agreement with the observed scaling ratios, as we demonstrate by a simplified short-range model that is presented in chapter 4.

In contrast to the recent studies in the homonuclear gases of Cs and Li atoms [Huang et al., 2014b,a; Rem et al., 2013], which have shown that temperature effects need to be taken into account in order to accurately determinate the Efimov resonance positions, the present analysis does not consider resonance shifts arising from such effects. The third Efimov feature is located deeply into the unitarity limited regime, and the second one may already be strongly affected. In fact, at the time when this analysis was performed, no finite temperature models describing three-body recombination spectra of heavy-heavy-light collisions were available, thus the extracted resonance positions may be systematically influenced by the oversimplified fitting model that was used in their analysis. A significantly better description of the temperature averaged three-body recombination spectra is presented in Sect. 3.4.4.

Finally, although the scaling ratio in a heavy-heavy-light system depends on the mass ratio, for its exact value the number of resonant interactions is important (see Sect. 3.2.2). For a system with mass ratio of $m_{\mathrm{Cs}}/m_{\mathrm{Li}} = 22.1$ the exact value of the scaling factor λ can change from 4.88 to 4.80 for $a_{\mathrm{CsCs}} = 0$ to $a_{\mathrm{CsCs}} \to \infty$, respectively [Efimov, 1973; Braaten and Hammer, 2006; Yamashita et al., 2013; Petrov and Werner, 2015]. While the variation of the Cs background scattering length from $\approx -1200\ a_0$ to $\approx -1500\ a_0$ in the explored magnetic field range would translate into only a slight adjustment of the scaling factor, it still needs to be accounted for in a complete theoretical description. These variations are also included in the analysis that is presented in Sect. 3.4.4.

3.4.4 Recombination spectra at finite temperatures

The measured three-body loss rates are strongly influenced by finite temperature effects, especially in the vicinity of the pole of a FR. The most prominent of them is the unitarity limit, at which the three-body collision rate, and hence the atom losses, saturates, according to Eq. (3.29). The second and third $LiCs_2$ Efimov feature are located in this regime. Additionally, the resonant features may be broadened and shifted due to collisional energy distribution of the scattering atoms, and because of the residual energy dependence of the virtual Efimov state that is immersed in the scattering continuum [Wang et al., 2010; Wang and Esry, 2011; Wang et al., 2013; Huang et al., 2015]. Therefore, in order to properly describe the recombination spectra, it is necessary to correctly treat the nontrivial connection between the unitarity regime and the appropriate scaling law far away from the unitarity [D'Incao and Esry, 2009; Petrov and Werner, 2015; Mikkelsen et al., 2015].

To investigate the influence of the finite energy distribution and unitarity limit furthermore, we measure the three-body recombination spectrum at a lower temperature. We use the bichromatic optical-dipole trap configuration to prepare the mixture in the energetically lowest scattering channel $|\alpha\rangle$ at a temperature of 120 nK, as explained in Sect. 3.3. In analogy to the measurements at 450 nK temperatures, we record the temporal evolution of Li and Cs atom numbers as a function of the external magnetic field. A typical time dependence is given in Fig. 3.13(a). The initial number of Li atoms is about a factor of 2 smaller than the Cs one, and during the hold time both of them significantly decrease. Thus, in contrast to the analysis of 450 nK data in Sect. 3.4.2, the approximation of a constant Li density is not valid anymore. Therefore, we simultaneously fit both rate equations (3.25) and (3.26) to the data, where the initial number of atoms $N_{\mathrm{Cs},0}$ and $N_{\mathrm{Li},0}$, and the three-body loss rate K_3 are the only free fitting parameters. We determine the single-body and the Cs intraspecies three-body loss rate K_3^{Cs} in independent measurements, in analogy with the procedure employed for the experiments at 450 nK (see Sect. 3.4.2). The

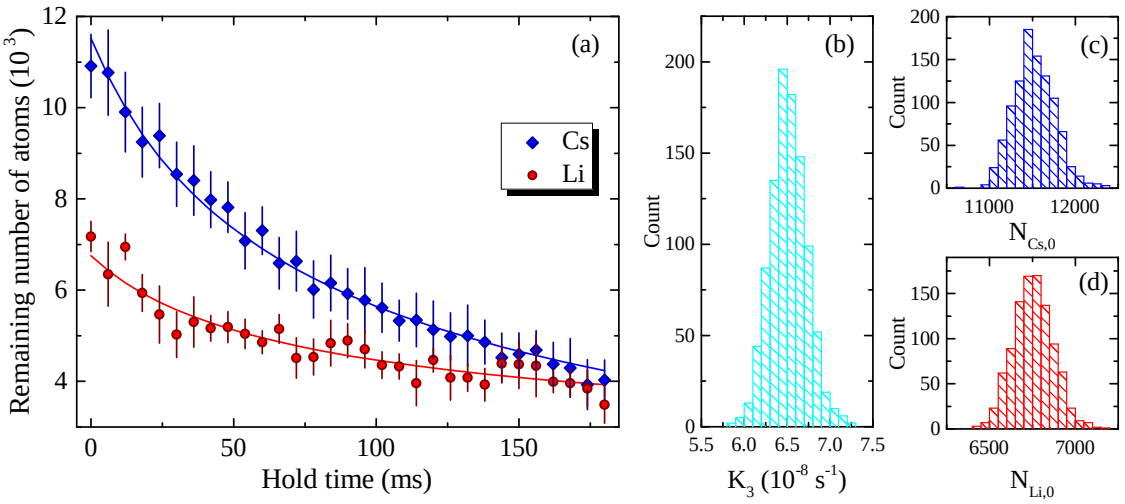

Figure 3.13: Temporal evolution of atom numbers in a Li-Cs mixture at 843.049 G magnetic field and 120 nK temperature. (a) Remaining number of Cs (blue diamonds) and Li (red circles) atoms as a function of hold time in the optical dipole trap. Each data point gives the mean of at least three independent measurements and the error bars represent one standard error. Blue and red solid lines show the result of a simultaneous fit of the coupled rate equations (3.25) and (3.26) to data. (b), (c), and (d) illustrates the final distributions of the three-body loss rate, initial Cs, and Li atom numbers, respectively, that are obtained by bootstrapping (see text).

excellent agreement between the model and data verifies once again that the coupled rate equations include all of the dominant loss processes.

In order to obtain an error estimation of the fitted K_3 value, we employ standard bootstrap techniques [Wu, 1986; Efron and Tibshirani, 1993]. In short, a population of sample estimators is created by repeating a weighted fit of data with randomly resampled residuals for a statistically significant number of times. The mean and variance of the obtained estimator population distributions then represent the estimation of the mean value and uncertainty of the respective parameters. In this way obtained population distributions of the fitting parameters for a typical time evolution of the Li-Cs mixture are given in Fig. 3.13(b), (c), and (d). For the resampling of residuals we have used the standard normal distribution, as appropriate for behavior exhibiting heteroskedasticity [Wu, 1986], and performed the fitting procedure for 1000 repetitions. We assume that the mean and standard deviation of the obtained distributions are the best estimates characterizing the time evolution of atom numbers in the mixture, and give them as the extracted K_3 and its error, respectively. For example, for the three-body loss rate that is depicted in Fig. 3.13(b) this yields $K_3 = 6.51(21)\times10^{-8}$ s^{-1}, where the value in the brackets denotes one standard deviation.

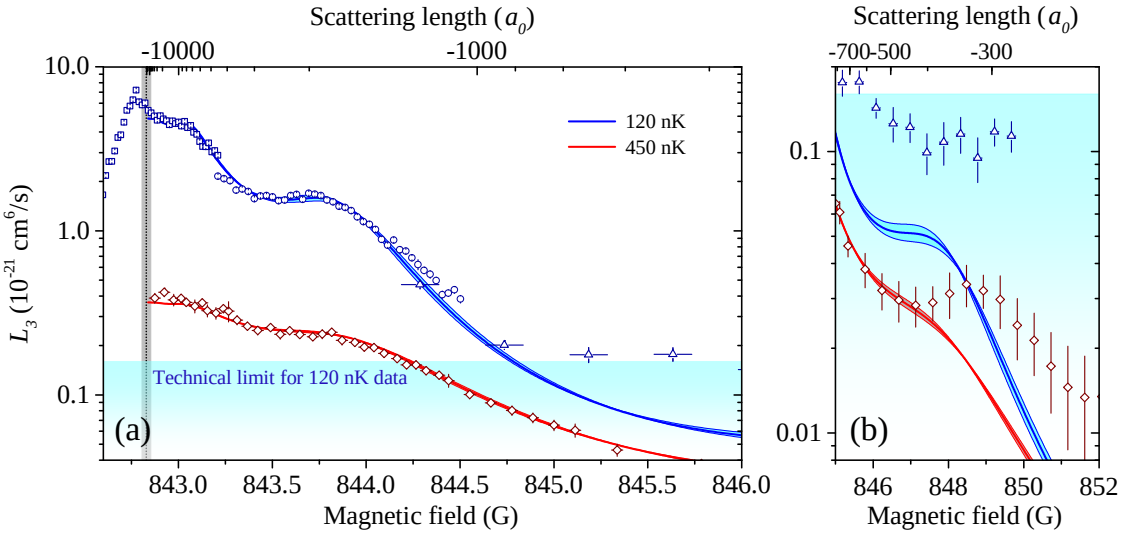

Figure 3.14: Li-Cs three-body recombination at a temperature of 120 nK (blue squares, circles, and triangles) and 450 nK (red diamonds) in two magnetic field ranges (a) and (b). Different symbols denote data sets that are taken with various maximum hold times and in different magnetic field ranges. For the 120 nK and 450 nK data set the error bars represent one standard deviation obtained from the bootstrapping procedure (see text) and one standard error of the mean (see Sect. 3.4.2), respectively. The fit of the analytic, finite temperature zero-range model is given by the solid lines, where the shaded region around it represents the uncertainty of the FR parametrization. The cyan shaded region depicts the technical limit L_3^{lim} of the experimentally measurable L_3 rate for the 120 nK data (see Eq. (3.30)). The FR pole and its uncertainty are given by the dashed line and gray area around it, respectively.

By repeating the measurement of time evolution and analysis procedure we record in Fig. 3.14 shown magnetic field dependence of the three-body loss rate. We subdivide the relevant magnetic field region in three subsets, for each of which we experimentally optimize the maximum hold time. It ranges from 190 ms for the data set the closest to the resonance, to 310 ms and 790 ms for the intermediate and the furthest one, respectively. For comparison, we also show the three-body recombination spectrum taken at a temperature of 450 nK that was discussed in Sect. 3.4.2. We have used Eq. (3.28) with the experimentally employed parameters to calculate L_3 from the fits, and scaled the data within the experimental uncertainties by factors $\gamma_T^{(i)}$ (see below) to reproduce the theoretical $L_3^{(th)}$ rates. The factors $\gamma_T^{(i)}$, independent of the fitting procedure, are located well within our systematic errors. Both spectra have one common feature at roughly $B_1 \approx 843.76$ G or $a_-^{(1)} \approx -1860\ a_0$, which corresponds to the first excited $LiCs_2$ Efimov resonance. For the data taken at 120 nK another feature emerges at around $B_2 \approx 843.03$ G, for an even larger scattering length $a_-^{(2)} \approx -8540\ a_0$, now clearly demonstrating the

second excited Efimov resonance also in recombination spectrum.

The minimal experimentally measurable interspecies three-body loss rate L_3^{lim} is limited by intraspecies losses. Away from the pole of a FR the intraspecies losses dominates, i.e. $L_1^{\mathrm{Cs}} + L_3^{\mathrm{Cs}} n_{\mathrm{Cs}}^2 \gg 2L_3 n_{\mathrm{Cs}} n_{\mathrm{Li}}$, or equivalently $L_1^{\mathrm{Cs}} + K_3^{\mathrm{Cs}} N_{\mathrm{Cs}}^2 \gg 2K_3 N_{\mathrm{Cs}} N_{\mathrm{Li}}$. We empirically determine that for our experiment and data analysis this is on the order of 1/10 of the summed intraspecies loss rates, or

$$L_3^{lim} \sim \frac{1}{20}\left(L_1^{\mathrm{Cs}} \frac{1}{n_{\mathrm{Cs}} n_{\mathrm{Li}}} + L_3^{\mathrm{Cs}} \frac{n_{\mathrm{Cs}}}{n_{\mathrm{Li}}}\right). \tag{3.30}$$

This expression yields the lower limit for the experimentally accessible L_3 rates, since reliable extraction of interspecies loss rates for data points lying below is not possible due to shot-to-shot induced atom number fluctuations, as shown in Fig. 3.14 for magnetic fields larger than 845 G at a temperature of 120 nK. In this range the extracted L_3 rate becomes approximately constant, and the data points can only represent the upper bound of the actual L_3 rate. For the dataset at 450 nK this limit is $L_3^{lim,450\mathrm{nK}} \sim 1.3{\times}10^{-25}$ cm^6/s, and therefore much smaller than any of the experimentally measured L_3 rates, while for the one at a temperature of 120 nK $L_3^{lim,120\mathrm{nK}} \sim 1.6{\times}10^{-22}$ cm^6/s. We note that this restraint is of a purely technical nature and could be overcome by improving the shot-to-shot stability of the atom numbers, by decreasing n_{Cs} and $L_1^{\mathrm{Cs,Li}}$, or by increasing n_{Li} and overlap (see Sect. 3.3.1).

The three-body recombination spectra of $LiCs_2$ can be described by a zero-range S-matrix formalism for two identical bosons interacting with a third distinguishable particle in a system where all interactions are characterized by a negative scattering length [Petrov and Werner, 2015; Mikkelsen et al., 2015], as explained in Sect. 3.2.3. In this case the loss is entirely dominated by recombination into deeply bound states, since neither of the pairs can support a weakly bound dimer state. The kinetic energy that results from a recombination event of three free particles into a deeply bound state is much larger than the potential depth in which the mixture is trapped, thus each such event leads to trap loss. The recombination event rate is equal to the three-body loss rate L_3, which after thermal averaging can be expressed as [Petrov and Werner, 2015]

$$L_3^{(th)} = 4\pi^2 \cos^3\phi \frac{\hbar^7 \left(1 - e^{-4\eta}\right)}{\mu^4 \left(k_b T\right)^3} \int_0^\infty \frac{1 - |s_{11}|^2}{\left|1 + (kR_0)^{-2is_0} e^{-2\eta} s_{11}\right|^2} \exp\left[\frac{-\hbar^2 k^2}{2\mu k_B T}\right] k dk, \tag{3.31}$$

where angle $\phi = 1.275$ rad is given by the mass ratio $\sin\phi = m_{\mathrm{Cs}}/\left(m_{\mathrm{Cs}} + m_{\mathrm{Li}}\right)$, μ is the two-body reduced mass of Li-Cs, η is the inelasticity parameter, and R_0 parametrizes the short-range range boundary condition by fixing a node of the hyperradial three-body wavefunction at small distances, as discussed in Sect. 3.2.3.

The function s_{11} depends only on ka_{LiCs}, ka_{Cs}, and the mass ratio. In fact, the a_{LiCs} and a_{Cs} scattering lengths are not independent, as both of them are functions of the external magnetic field. Thus, for a particular system in a single scattering channel the four free parameters can be reduced to three.

For the Li-Cs system the function s_{11} and an optimized code for the calculation of Eq. (3.31) have been computed and cordially provided to us by D. Petrov from Université Paris-Sud, Orsay, France. It employs the magnetic field dependence of Cs-Cs interactions obtained in Ref. [Berninger et al., 2013], and Li-Cs FR parametrization from Ref. [Pires et al., 2014b], which is a slightly older version from in Sect. 2.4 presented result that was obtained as the final outcome in this work. The small differences between the two versions can be neglected, because a_{Cs} is smooth in the considered magnetic field region and therefore the dependence $a_{\mathrm{Cs}}\left(a_{\mathrm{LiCs}}\right)$ is practically unchanged.

We compare our measurements with the thermally averaged S-matrix model by simultaneously fitting Eq. (3.31) to the data. The fit employs a factor γ to correct for the absolute three-body loss rate, inelasticity and three-body parameter η and R_0, respectively, as free fitting parameters. Since the temperature of each species is measured independently in a time-of-flight experiment, we use the experimentally measured temperatures as fixed parameters at 120 nK and 450 nK. We introduce on total four different factors $\gamma_{120}^{(a)}$, $\gamma_{120}^{(b)}$, $\gamma_{120}^{(c)}$, and γ_{450} for data sets taken in different magnetic field ranges, and two parameters η_{120} and η_{450}. The fit uses a global R_0. After a weighted minimization of chi-squared, the following set of parameters is obtained: $\gamma_{120}^{(a)} = 2.26$, $\gamma_{120}^{(b)} = 1.44$, $\gamma_{120}^{(c)} = 0.83$, $\gamma_{450} = 0.73$, $\eta_{120} = 0.60$, $\eta_{450} = 0.87$, and $R_0 = 126\ a_0$. We refrain from giving any errors here; the extraction of uncertainties and cross-correlations would require more involved treatment of the experimental uncertainties and error propagation, since the parameters may be connected in a nontrivial way. For the data set at a temperature of 120 nK, we exclude the points below the pole of the FR and below L_3^{lim} (see Eq. (3.30)) from the fit. For the measurements at 450 nK, the fit starts to deviate for magnetic fields above 847 G, which we also exclude from the analysis. The fitting procedure is repeated for two additional FR pole positions, 842.829 ± 0.023 G, to estimate the influence of the FR parametrization uncertainty, which changes R_0 by around 3%. The factors $\gamma_T^{(i)}$ are well within the experimental uncertainties of the absolute three-body loss rate L_3, which are a factor 1.8 and 3 for the 450 nK and 120 nK data, respectively. We note that identical fitting procedure with the temperatures of the colder and hotter data sets as free fitting parameters gives a better fit result and overall agreement. In this way we obtain $T_{450} = 410$ nK and $T_{120} = 170$ nK, for the hotter and colder data set respectively, where the latter fitted temperature is beyond the systematic error of our measurements. We discuss possible reasons for this in Sect. 4.3.1.

The result of the fitting procedure is plotted in Fig. 3.14. The thermally averaged zero-range theory simultaneously recaptures the spectra for both data sets. It consistently describes the absolute loss rates, Efimov resonance positions and, consequently, scaling factors, and apparent shifts due to the finite collisional energy distribution and resulting thermal averaging in the magnetic field range between the pole of the FR at around 843 G and $\approx$ 847 G. The good agreement between the model and data indicates that the initial assumptions of the three-body recombination favoring deeply bound states is valid. More importantly, this verifies that in the direct vicinity of the FR pole ($|a_{\mathrm{LiCs}}| \gg r_0$), the behavior of the $LiCs_2$ Efimov resonances is universal, since the thermally averaged zero-range theory [Petrov and Werner, 2015] describes well the experimental results. In contrast, the ground state Efimov resonance at B_0 is not described by the zero range theory, as can be seen in Fig. 3.14(b). The variations of the Cs background scattering length in this magnetic field range and temperature effects are included in this model. The modifications of the three-body parameter with respect to the changing a_{CsCs} are on the order of a few percent (see Sect. 4.3.4), and therefore negligible. Thus, the most probable cause for these deviations is finite-range corrections, as already mentioned in Sect. 3.4.3. In the next chapter a complete treatment of the tree-body scattering problem with realistic short-range potentials will be presented. This approach recaptures the three-body recombination spectrum much better.

In order to quantify the positions of the Efimov resonances we determine the magnetic field values at which the calculated L_3 rate displays local maxima in the limit $\eta \to 0$ and $T \to 0$. The Eq. (3.31) with the previously obtained fit parameters yields $B_0 = 848.12$ G, $B_1 = 843.80$ G, and $B_2 = 843.015$ G for the three observed Efimov features, with the corresponding scattering lengths $a_-^{(0)} = -353\ a_0$, $a_-^{(1)} = -1792\ a_0$, and $a_-^{(2)} = -9230\ a_0$, which, except for the ground state, are in good agreement with the resonance positions determined by the simplified fitting model in Sect. 3.4.3. The fourth feature is expected to emerge around $B_3 = 842.866$ G ($a_-^{(3)} = -46283\ a_0$), deep into the unitarity dominated regime. Surprisingly, the Efimov scaling factors $\lambda_{n=1} \approx \lambda_{n=2} \approx 5.1$ of the first two periods are larger than 4.88, which is the value that the resonant limit of the zero-range theory deliver for the Li-Cs system (see Sect. 3.2.2). The third period gives $\lambda_{n=3} \approx 5.0$, matching the expectations better. This behavior demonstrates that even in the zero-range theory for heteronuclear systems the scaling factor for a series of Efimov resonances is not necessarily a constant, and may change depending on the specific value of the intraspecies scattering length. This shows also one of the main disadvantages in comparing the extracted Efimov resonance positions with the universal theory. Additionally, the determined feature positions and scaling factors strongly on the model that was used to obtain their values and therefore not necessarily the quantity they were intended to represent. Thus, a quantitative comparison between experi-

ment and data should be preferably made via juxtaposition of directly measurable quantities and their theoretical counterparts, such as L_3, and not through derived entities, as B_n, $a_-^{(n)}$, or λ_n in this case. An excellent example of such direct comparison is already mentioned and shown in Fig. 3.14, which is, however, not always possible, often due to lack of an appropriate and accessible theoretical model. In these cases one can still resort to qualitative comparison, which, depending on the model and its degree of simplification, may as well deliver an intuitive picture of the underlying physical mechanisms.

Chapter 4

Short-range effects in $LiCs_2$ Efimov resonances

Parts of this chapter are based on the following manuscript:

Finite-range effects in universal three-body recombination of ultracold Li and Cs atoms
J. Ulmanis, S. Häfner, R. Pires, E.D. Kuhnle, M. Weidemüller, Y. Wang, C.H. Greene
Manuscript in preparation

All calculations with the hyperspherical formalism and Lennard-Jones potentials that are presented in this chapter were performed by Y. Wang, Kansas State University, USA, and C.H. Greene, Purdue University, USA.

In this chapter we investigate departures from the universal behavior of weakly-bound $LiCs_2$ three-body states due to short-range effects in the heteronuclear Efimov scenario. As they are intrinsically connected to the so called three-body parameter, we introduce and briefly discuss its origin in ultracold atom systems in Sect. 4.1. The important role of short-range physics in the heavy-heavy-light Efimov effect can be illuminated most transparently with the Born-Oppenheimer (BO) approach. We recall the basic construction of this formalism for an ultracold three-body collision in Sect. 4.2.1. In analogy to the textbook example of the H_2^+ ion, we show how the Schördinger equation separates into a pair of coupled equations that govern the motion of the light and heavy particles. In this approach the synergy between the Efimov effect and individual pairwise interactions becomes exceptionally clear. Since low-energy binary atom collisions are predominantly governed by the van der Waals (vdW) tails of interatomic potentials, we concisely discuss their characteristic two-body length and energy scales, and demonstrate a simplified way of how they

can be incorporated into the three-body problem in Sect. 4.2.2. We exemplify this approach for the Li-Cs-Cs system, where length and energy scales separate, thus enabling us to obtain evermore illustrative picture of the inner workings of the short- and long-range regimes in the heteronuclear Efimov problem.

We continue by considering the observed deviations between the zero-range model and the recombination spectra at the 843 G Li-Cs Feshbach resonance, also presented in chapter 3, in Sect. 4.3.1. They are resolved numerically by the hyperspherical formalism that is employing pairwise Lennard-Jones potentials to essentially simulate the Li-Cs-Cs problem. We find good agreement between this on van der Waals physics based calculation and our measurements. To test the newly found agreement we experimentally realize the Li-Cs-Cs Efimov scenario close to the second broad Li-Cs Feshbach resonance at 889 G. It is characterized with a different Cs-Cs intraspecies interaction strength. We describe the resulting additional sequence of observed consecutive heteronuclear recombination resonances and its analysis with the hypershperical approach in Sect. 4.3.2. The experimentally and theoretically determined behavior of the ground Efimov resonance at each of the Li-Cs Feshbach resonances is different. We elucidate the origin of this qualitatively distinctive nature by the minimalistic Born-Oppenheimer picture in Sect. 4.3.4. It demonstrates a gradual crossover between the Cs_2 van der Waals potential and the Efimov scenario dominated regimes by a continuous tuning of the Cs-Cs scattering length.

4.1 The three-body parameter and short-range interactions

The zero-range Efimov scenario predicts the existence of an infinite number of bound three-body states that follows the discrete scaling symmetry [Braaten and Hammer, 2006]. This is a consequence of the underlying attractive $\propto -1/R^2$ potential with the average separation R between the particles, for which at the unitarity limit of the binary interaction with scattering length $a \to \infty$ neither short- nor long-range length scales can be defined. As the interaction strength is reduced, the Efimov potential extends to distances $R \sim |a|$ that provides with a natural upper limit. The shape of the effective short-range potential at separations $R \to 0$, however, remains unchanged. It leads to the peculiar result where no ground state of the three-body energy spectrum can be defined [Thomas, 1935; Coon and Holstein, 2002; Essin and Griffiths, 2006]. Of course, this is a purely mathematical problem, since in nature no true zero-range potentials exist[1]. Therefore one typically introduces a short-range

[1]There exist extremely good approximations to them, which is the exact source of the universality in few-body physics [Braaten and Hammer, 2006].

boundary condition, a three-body parameter, that in either of its various forms equally well defines the energy at which the first Efimov trimer state emerges.

In realistic three-body systems the short-range length scale is inevitably present. However, it is not always possible to easily relate it to the two-body properties, for example, if the binary interactions are not known to high accuracy. While in nuclear physics the short-range parts of pairwise interaction potentials are, indeed, hardly known and accessible, molecular potentials for experimentally used ultracold atom mixtures are typically available, or at least measurable. In this sense, the three-body parameter is determined by the exact form of the short-range interaction. Nevertheless, due to the computational complexity of accurately treating the complete potential, the problem is still often treated with the simplified use of the three-body parameter and zero-range theory. It is an excellent approximations in most of the cases.

The exact dependence of the three-body parameter on the details of the individual short-range pairwise potentials was a longstanding, open question. The internal structure of two particles that give rise to a particular two-body scattering resonance, in general, is different. This should inevitably lead to a three-body parameter that varied by a factor within the complete Efimov period e^{π/s_0}, even within the same system at different scattering resonances [D'Incao et al., 2009a]. In contrary, recent ultracold gas experiments with homonuclear systems, interacting via pairwise molecular potentials with long-range van der Waals tails, have revealed that the three-body parameter is approximately constant, if expressed in the units of the corresponding characteristic length scale r_{vdW} (see Eq. (4.14)) [Berninger et al., 2011; Knoop et al., 2012; Roy et al., 2013; Huang et al., 2014a]. In fact, no significant deviations from this universal behavior have been observed in any in the Sect. 3.1 mentioned experiments, indicating that the three-body parameter is governed by van der Waals physics and is insensitive to the specific short-range details of the pairwise interaction potential. Several theoretical studies have explained this behavior by showing that in the three-boson problem a nearly universal potential barrier appears at distances that are on the order of $R \sim 2r_{\mathrm{vdW}}$ [Wang et al., 2012a; Naidon et al., 2014b,a]. This leads to a three-body repulsion that prevents the system from exploring shorter distances. The same conclusion of an approximately constant three-body parameter has been obtained by various other methods [Chin, 2011; Naidon et al., 2012; Wang et al., 2012a; Sørensen et al., 2012, 2013b; Schmidt et al., 2012]. Thus, a more general explanation is potentially true [Naidon et al., 2014b]. It suggests that in the short-range region emerging pair correlations, which lead to suppressed probability of finding two particles with separation smaller than r_{vdW}, give rise to the universal three-body parameter. Similar results have been demonstrated for the heteronuclear [Wang et al., 2012d] and even for three-body systems interacting via d-wave scattering resonances [Wang et al., 2012b]. The

success of the van der Waals theory in explaining the three-body parameter for ultracold atom systems has lead to the introduction of a new class of van der Waals universality for a more general selection of low-energy three-body observables close to two-body Feshbach resonances [Wang and Julienne, 2014; Wang et al., 2014].

The Efimov and van der Waals physics in ultracold gases are deeply interconnected. In these systems modifications to the original Efimov scenario under the influence of a short-range potential is one of the experimentally accessible signatures, which enables the exploration of this topic. Several theoretical studies have demonstrated that the ground Efimov state can be subject to such corrections [Wang et al., 2012a; Schmidt et al., 2012; Sørensen et al., 2012, 2013a; Thøgersen et al., 2008; Platter et al., 2009; Naidon and Ueda, 2011; Kievsky and Gattobigio, 2013] and even three-body forces [D'Incao et al., 2009a; Hammer et al., 2013]. Furthermore, the recent experiments of the first excited-state resonance in Cs [Huang et al., 2014b; Wang and Julienne, 2014] and ^{4}He [Kunitski et al., 2015], and the new analysis of ^{6}Li [Huang et al., 2014a] and ^{7}Li data [Gattobigio and Kievsky, 2014] not only hint at deviations from the universal scaling, but also to shifts of the ground-state resonances due to finite range effects. As discussed in Sect. 3.2.2, the universal zero-range approach is exact only in the limit $a/r_{\mathrm{vdW}} \to \infty$, which is only approximately fulfilled for many of the experiments with homonuclear systems [Berninger et al., 2011; Wild et al., 2012; Roy et al., 2013; Huang et al., 2014a]. It is fulfilled much less so for the heteronuclear ones [Pires et al., 2014b; Tung et al., 2014], which is exactly why these systems are the ideal candidates to study the intrinsic link between the van der Waals and Efimov physics dominated regimes.

The Li-Cs mixture is an excellent system to investigate and answer these questions. The Li+Cs+Cs three-body recombination spectra, that we analyzed with the thermally averaged zero-range theory in chapter 3, clearly illustrated both, the remarkably universal behavior of the heteronuclear Efimov series close to the pole of the Feshbach resonance, and the deviations of the ground Efimov resonance further away from it. The unique combination of the dense spectrum of consecutive recombination features in the Efimov regime and the tunability of inter- and intraspecies scattering lengths will turn out to be well suited for the observation of the transition between the short- and long-range, and two- and three-body dominated regimes.

4.2 Minimalistic model for the three-body problem with short-range interactions

The Born-Oppenheimer (BO) approximation delivers one of the most transparent pictures of the three-body problem between interacting two heavy and one light particle [Braaten and Hammer, 2006; Petrov, 2010; Bhaduri et al., 2011]. It recovers

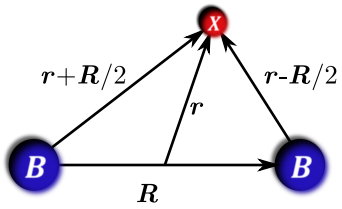

Figure 4.1: Three-body coordinates that are used in the Born-Oppenheimer approximation.

the essential physics leading not only to the Efimov effect, but also modifications due to short-range potentials in the case where the length and energy scales between the interactions in the problem can be separated. With respect to the Efimov physics the BO approximation was initially discussed by Fonseca et al. [1979], and later applied in various different scenarios, for example, zero-range molecule-molecule [Petrov et al., 2005; Marcelis et al., 2008] and atom-molecule [Efremov et al., 2009] collisions, three-component Fermi gases [Nishida and Tan, 2008], three-body problem in higher partial waves [Zhu and Tan, 2013], and in systems with reduced dimensionality [Nishida and Tan, 2009; Bellotti et al., 2013]. Recently, it has been used to study the effects of short-range interactions on the three-body parameter [Sørensen et al., 2012; Wang et al., 2012d]. In Sect. 4.2.1 we briefly recall its basic structure that leads to the emergence of the Efimov effect in the heavy-heavy-light system by closely following Ref. [Petrov, 2010]. In Sect. 4.2.2 we discuss the procedure of how to incorporate the short-range van der Waals interaction between the two heavy atoms.

4.2.1 The Born-Oppenheimer approximation

We start with the three-body problem BBX according to the coordinates given by Fig. 4.1. The two heavy atoms B with mass M are separated by the vector $\boldsymbol{R}$, and one light atom X with mass m is located at the position $\boldsymbol{r}$ with respect to the center of mass of the two atoms B. The Schödinger equation for the three-body wavefunction $\Psi(\boldsymbol{r}, \boldsymbol{R})$ can be expressed as

$$H\Psi(\boldsymbol{r}, \boldsymbol{R}) = E\Psi(\boldsymbol{r}, \boldsymbol{R}), \tag{4.1}$$

with the full Hamiltonian is given by

$$H = -\frac{\hbar^2}{M}\nabla^2_{\boldsymbol{R}} - \frac{\hbar^2}{2\mu_X}\nabla^2_{\boldsymbol{r}} + V_{BB}(\boldsymbol{R}) + V_{BX}\left(\left|\boldsymbol{r} + \frac{\boldsymbol{R}}{2}\right|\right) + V_{BX}\left(\left|\boldsymbol{r} - \frac{\boldsymbol{R}}{2}\right|\right), \tag{4.2}$$

where V_{IJ} denotes the interaction potential between the atoms I and J, and $\mu_X = 2Mm/(2M+m)$ is the reduced mass of the light particle. The BO approximation

takes advantage of the large mass imbalance by assuming that the motion of the light particle adjusts almost immediately to changes in the distance $\boldsymbol{R}$ between the heavy particles. If this is the case, the three-body wavefunction can be written in a separable form as

$$\Psi(\boldsymbol{r}, \boldsymbol{R}) = \psi_{\boldsymbol{R}}(\boldsymbol{r})\phi(\boldsymbol{R}), \tag{4.3}$$

where the wavefunction for the light particle $\psi_{\boldsymbol{R}}(\boldsymbol{r})$ depends parametrically on $\boldsymbol{R}$, and $\phi(\boldsymbol{R})$ is the wavefunction of the two heavy particles. This assumption is exact in the limit $m/M \to 0$, and allows to separate the initial three-body Schrödinger equation (4.1) in a system of two coupled equations

$$\left[-\frac{\hbar^2}{2\mu_X}\nabla^2_{\boldsymbol{r}} + V_{BX}\left(\left|\boldsymbol{r} + \frac{\boldsymbol{R}}{2}\right|\right) + V_{BX}\left(\left|\boldsymbol{r} - \frac{\boldsymbol{R}}{2}\right|\right)\right]\psi_{\boldsymbol{R}}(\boldsymbol{r}) = E_{\boldsymbol{R}}\psi_{\boldsymbol{R}}(\boldsymbol{r}) \tag{4.4}$$

$$\left[-\frac{\hbar^2}{M}\nabla^2_{\boldsymbol{R}} + V_{BB}(\boldsymbol{R}) + E_{\boldsymbol{R}}\right]\phi(\boldsymbol{R}) = E\phi(\boldsymbol{R}), \tag{4.5}$$

where the first equation describes the motion of the light particle with energy $E_{\boldsymbol{R}}$ in a potential created by the heavy ones. The energy $E_{\boldsymbol{R}}$ is a function of the separation $\boldsymbol{R}$ and adjusts instantly to any changes in the location of particles B. The second equation governs the relative motion of the two heavy particles in the effective potential surface $E_{\boldsymbol{R}}$ created by the light particle.

Equations (4.4) and (4.5) demonstrate the essence of the Born-Oppenheimer approximation for the three-body problem, analogous not only to the simplest molecule H_2^+ [Atkins and Friedman, 2000], but also to the hyperspherical formalism that was discussed in Sect. 3.2.1. The solution of the three-body problem is reduced to finding wavefunctions $\psi_{\boldsymbol{R}}(\boldsymbol{r})$ and the potential surface $E_{\boldsymbol{R}}$ for the relative motion of the two heavy particles by solving equation (4.4) for the light particle with fixed internuclear distance $\boldsymbol{R}$. These solutions are then used to construct and extract the total energy E of the system and wavefunctions $\phi(\boldsymbol{R})$ from equation (4.5) for the heavy particles.

The success of the Born-Oppenheimer approximation in molecular physics is based on the extremely well separable mass scales of the electron and nuclei, exceeding already a factor of 3500 for the simplest three-body molecule H_2^+. As the mass ratio is reduced, the motion of light and heavy particles is being increasingly stronger coupled, and the prescription of Eq. (4.3) for the separation of the three-body wavefunction becomes increasingly inaccurate. However, if the mass ratio is not yet too small or, in other words, if the light and heavy motions are not coupled too strong, we may investigate the corrections to the BO approximation. To produce the separated system of BO equations (4.4) and (4.5) we have neglected the

coupling term

$$H_c\psi_{\boldsymbol{R}}(\boldsymbol{r})\phi(\boldsymbol{R}) = -\frac{\hbar^2}{M}\left[2\left(\nabla_{\boldsymbol{R}}\phi(\boldsymbol{R})\right)\cdot\left(\nabla_{\boldsymbol{R}}\psi_{\boldsymbol{R}}(\boldsymbol{r})\right) + \phi(\boldsymbol{R})\nabla^2_{\boldsymbol{R}}\psi_{\boldsymbol{R}}(\boldsymbol{r})\right] \tag{4.6}$$

between the wavefunctions of the light and heavy atoms[2]. Thus, depending on the required accuracy, for example, if H_c is small in comparison to H, the corrections to the simple BO picture can be calculated from the perturbation theory, otherwise one has to resort to the hyperspherical formalism. In fact, a good agreement between the BO and hyperspherical calculation has been numerically found also for ultracold atom collisions with heavy-to-light mass ratios in the range from 14 to 29 [Wang et al., 2012d]. Since for our experiments with Li and Cs atoms the mass ratio is $m_{\mathrm{Cs}}/m_{\mathrm{Li}} \approx 22$, in the following discussion we omit the correction term.

Solution for the light particle

The wavefunction of the light particle $\psi_{\boldsymbol{R}}(\boldsymbol{r})$ can be calculated by assuming that the interaction between the heavy and light particle V_{BX} is described by the zero-range potential that was introduced in Eq. (3.12), and by considering only the case of angular momentum $l = 0$, which allows to neglect the spherical harmonics. This is equivalent to a double delta potential in three dimensions, for which the approximate solution can be written down analytically by following the approach from Sect. 3.2.2, namely, by requesting that the Bethe-Peierls boundary condition at vanishing $\boldsymbol{r} \pm \boldsymbol{R}/2$ is fulfilled. One obtains the symmetric and antisymmetric solutions $\psi^{(\pm)}_{\boldsymbol{R}}(\boldsymbol{r})$ that read [Efremov et al., 2009; Petrov, 2010]

$$\psi^{(\pm)}_{\boldsymbol{R}}(\boldsymbol{r}) = \frac{1}{2\sqrt{\pi}}\left(\frac{\kappa_\pm}{1 \pm e^{-\kappa_\pm R}}\right)^{1/2}\left(\frac{e^{-\kappa_\pm|\boldsymbol{r}-\boldsymbol{R}/2|}}{|\boldsymbol{r}-\boldsymbol{R}/2|} \pm \frac{e^{-\kappa_\pm|\boldsymbol{r}+\boldsymbol{R}/2|}}{|\boldsymbol{r}+\boldsymbol{R}/2|}\right), \tag{4.7}$$

where the wave vector $\kappa_\pm$ dependence on R and interspecies scattering length a is given by the transcendental equation

$$\pm e^{-\kappa_\pm R} = \kappa_\pm R - R/a, \tag{4.8}$$

and the energy of the light particle is $E^\pm_R = \kappa^2_\pm/(2\mu_X)$. In Sect. 4.2.2 we will show that this is a reasonable approximation for the Li-Cs interaction since the relevant length scales roughly separate.

The resulting energies and wavefunctions are depicted in Fig. 4.2. The wavefunction of the antisymmetric solution has a node on the symmetry axis between

[2]This is analogous to the hyperspherical formalism, where the couplings between different scattering channels were neglected in order to obtain the single channel representation (see Sect. 3.2.1, Eqs. (3.9) and (3.10)).

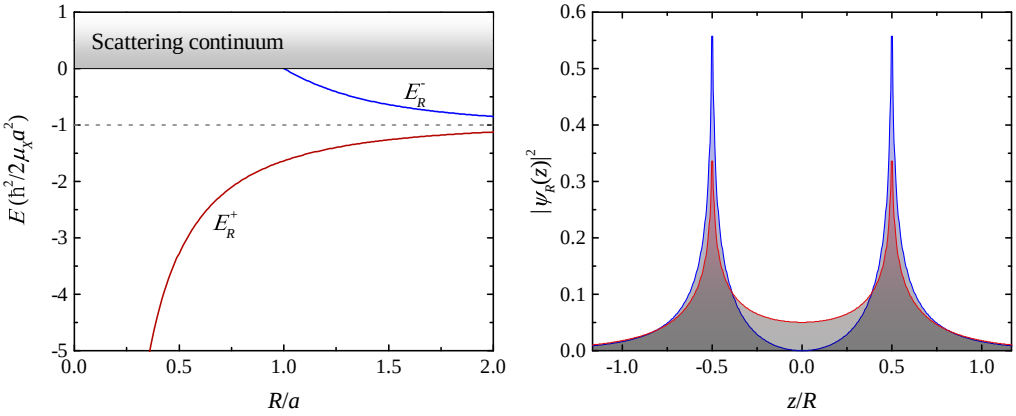

Figure 4.2: Left panel: Born-Oppenheimer energies $E_R^{\pm}$ of the light particle. Right panel: the probability distribution of finding the light particle X at a distance z on the internuclear axis between the heavy particles B for the symmetric (red line and shaded area) and antisymmetric (blue line and shaded area) wavefunction at $a \to \infty$.

the two heavy atoms, whereas the symmetric one also spreads in the interparticle region. There is a much larger probability of finding the light particle in-between the heavy ones if the three-body system is in the symmetric state than in the antisymmetric. Thus in the symmetric (antisymmetric) state the light atom generates an effectively attractive (repulsive) interaction between the heavy ones, which leads to lower (higher) energy E_R^+ (E_R^-). In the asymptotic region $R \gg a$ both potentials approaches the molecular binding energy $-\hbar^2/(2\mu_X a^2)$. In this simplified picture, the symmetric potential is the only one that can support bound states. The particles B are bound together by the attraction that is mediated via the interactions with the light one. In contrast, the antisymmetric state is purely repulsive and merges with the continuum at $R = a$.

Solution for the heavy particle and the Efimov effect in the zero-range limit

Since we are interested in three-body bound states, the quantity of the most relevance is the attractive potential of the light particle E_R^+. In the long-distance asymptotic regime, $R \gg a$, the potential energy E_R^+ can be obtained by the expansion of Eq. (4.8) in power series of the small parameter $e^{-R/a}$, and leads to Yukawa-type force between the heavy atoms [Fonseca et al., 1979; Petrov, 2010]. On the pole of the scattering resonance $a = \infty$ Eq. (4.8) simplifies and yields the short-distance asymptote

$$E_R^+ = -\frac{\hbar^2 W(1)^2}{2\mu_X R^2}, \tag{4.9}$$

where $W(z)$ is the Lambert-W function, defined by the solution to the equation $z = W(z)e^{W(z)}$. This again gives rise to the $\propto -1/R^2$ potential and, consequently, the Efimov effect, as was already discussed in Sect. 3.1 and 3.2.2. The scaling factor $\lambda = e^{\pi/s_0}$ is connected to the effective form of the potential E_R^+ by

$$s_0^{(\mathrm{BO})} = \sqrt{\frac{MW(1)^2}{2\mu_X} - \frac{1}{4}}, \tag{4.10}$$

which is depicted in Fig. 3.2 as a function of the heavy-to-light mass ratio. In accordance with the more general zero-range treatment in the hypershperical coordinates that was discussed in Sect. 3.2, the BO approximation recaptures the increase and decrease of the scaling factor with the mass ratio, and coincides with it in the asymptotic region $M \gg m$. At the same time, deviations between the two approaches become apparent as the mass ratio is decreased, also expected, since the dynamics of the heavy and light particles cannot be separated anymore, and the corrections to the BO picture become significant.

The wavefunction of the heavy particle $\phi(\boldsymbol{R})$ is obtained by solving Eq. (4.5) with the effective energy E_R^+ given by Eq. (4.9). If the interaction potential $V_{BB}(R)$ is isotropic, which is typically the case for ultracold atom experiments with alkali metals in the ground state, the Eq. (4.5) can be transformed into spherical coordinates [Landau and Lifshitz, 1991; Atkins and Friedman, 2000]. For the scale-invariant region ($r_0 \ll R \ll a$) one obtains the radial Schrödinger equation

$$-\frac{\hbar^2}{M}\left(\frac{\partial^2}{\partial R^2} - \frac{\beta_{s_0,l}}{R^2} - \frac{M}{\hbar^2}V_{BB}(R)\right)\chi_{s_0}(R) = E\chi_{s_0}(R), \tag{4.11}$$

where $\beta_{s_0,l} = l(l+1) - s_0^2 - 1/4$ describes the effective potential with angular momentum l, and the total wavefunction has been decomposed into a radial part $\chi_{s_0}(R)$ and spherical harmonics $Y_l^m(\theta,\varphi)$ by the substitution

$$\phi(\boldsymbol{R}) = \frac{\chi_{s_0}(R)}{R}Y_l^m(\theta,\varphi). \tag{4.12}$$

In the zero-range approximation for the interaction potential V_{BB} and for angular momentum $l = 0$, the radial Schrödinger equation (4.11) reduces to the original Efimov's equation (3.15) in the hyperspherical formalism[3], thus recovering the Efimov scenario, which was already extensively discussed in Sect. 3.2.2.

The BO approximation also allows a simple introduction of quantum statistics of the heavy atoms [Petrov, 2010]. In case of identical bosons (fermions) the total three-

[3]Note that the length variable R used in the hyperspherical and BO approach denotes the hyperradius and the distance between the heavy particles, respectively. This implies a different definition of the reduced mass, as discussed in Sect. 3.2.1.

body wavefunction $\Psi(\boldsymbol{r}, \boldsymbol{R}) = \psi_{\boldsymbol{R}}(\boldsymbol{r})\phi(\boldsymbol{R})$ has to be symmetric (antisymmetric) with respect to the exchange of the heavy particles, which corresponds to the symmetric (antisymmetric) solution of the light atom wavefunction. Thus, the Efimov effect manifests itself in s-wave or p-wave collisions if the heavy particles are bosons or fermions, respectively. Since in our experiments we employ the bosonic Cs atoms, we expect to observe it for the s-wave channels.

4.2.2 Weakly bound $LiCs_2$ Efimov trimers with van der Waals interactions

The BO approximation yields an exceptionally transparent interpretation not only of the Efimov effect, but also of the finite-range modifications to it. According to Eq. (4.11) the total BO potential for the heavy particles is a sum of two contributions. One part is the attractive $\propto -1/R^2$ potential that is induced by the resonant heavy-light particle interaction, responsible also for the emergence of the Efimov effect. The other part is the two-body interaction potential $V_{BB}(R)$ between the two heavy particles that introduces a natural short-range length scale. This clearly illustrates that the ground state for the geometrical progression of bound three-body states, and more importantly, the three-body parameter, is a consequence of the BO interaction potential for the heavy particles. In what follows we exemplify this for the Li-Cs system, which is one of the prototypical combinations with large mass imbalance, and of the most importance for our experiments.

Therefore, let us consider the interactions between a pair of two alkali-metal atoms i and j, which are controlled by the electronic molecular potential, similar to those discussed in Sect. 2.2.2 and shown in Fig. 2.3. Many properties of the weakly-bound Efimov states can be understood from the van der Waals part of the potential because its characteristic energy scale is similar to those of trimer and low-energy scattering states. The deeply bound states, while still present in the molecular potential, for close to threshold collisions are of minor importance, as discussed in Sect. 2.2. For distances that exceed the size of the individual electron clouds of each atom the potential is attractive and displays the vdW form

$$V_{ij}(r) = -\frac{C_6^{ij}}{r^6}, \tag{4.13}$$

where the coefficient C_6^{ij} depends on the details of the electronic configurations and is often obtained from either *ab initio* calculations (see, for example, [Derevianko et al., 2001; Porsev and Derevianko, 2003; Porsev et al., 2014]), photoassociation [Jones et al., 2006] or Feshbach spectroscopy [Köhler et al., 2006; Chin et al., 2010]. This allows one to introduce the characteristic length and energy scales r_{vdW}^{ij} and

Table 4.1: Characteristic van der Waals length and energy scales for pairwise interactions in the Li-Cs system. Using parameters from Derevianko et al. [2001].

$i-j$	Li-Li	Cs-Cs	Li-Cs
r_{vdW}/a_0	31	101	45
E_{vdW}/h (MHz)	28	2.7	156

E^{ij}_{vdW}, respectively, which read [Chin et al., 2010]

$$r^{ij}_{\mathrm{vdW}} = \frac{1}{2}\left(\frac{2\mu C^{ij}_6}{\hbar^2}\right)^{1/4} \tag{4.14}$$

and

$$E^{ij}_{\mathrm{vdW}} = \frac{\hbar^2}{2\mu_{ij}\left(r^{ij}_{\mathrm{vdW}}\right)^2}, \tag{4.15}$$

where μ_{ij} is the two-body reduced mass. For ultracold binary collisions the vdW scales determine the threshold between the short-range ($r < r_{\mathrm{vdW}}$) and long-range ($r > r_{\mathrm{vdW}}$) behavior of the two-body potential. The short-range region is dominated by fast oscillations of the wavefunction because the local wavenumber becomes large in comparison to the asymptotic one. In the long-range region a scattering wavefunction approaches its asymptotic form that is governed by the de Broglie wavelength of the ultracold collision, while a bound wavefunction decays exponentially. Any bound two-body state will exhibit spatial extension on the order of or smaller than r_{vdW}, with the only exception of the last s-wave bound state for the case of the universal halo dimer, for which $a \gg r_{\mathrm{vdW}}$ [Chin et al., 2010] (see also Fig. 4.3).

We list the characteristic length scales for the interactions within the Li-Cs system in Table 4.1. The vdW length scale for the Cs-Cs interaction is by roughly a factor of two larger than the Li-Cs one[4]. This indicates that the BO approach that was discussed in Sect. 4.2.1, may be approximately applicable to the Li-Cs system as well. Therefore in the following discussion we model the Li-Cs and Cs-Cs interactions by the zero-range contact and vdW model potentials, respectively. This approximation would hold better for systems where the characteristic length scales for intra- and interspecies short-range interactions were separated by an even larger factor.

This approach is reinforced furthermore by noticing that also the characteristic two- and three-body energy scales in the resonant limit can be separated. Remarkably, the energies ε^{ij}_{-n} of near threshold bound two-body states in a vdW potential are approximately determined by the E^{ij}_{vdW} [Gao, 1998; Chin et al., 2010; Wang et al.,

[4]We do not consider the Li-Li vdW interactions, since in our experiments the fermionic Li is prepared in a single spin state, which does not undergo s-wave scattering.

2014]. Thus, if there is a bound s-wave dimer at the threshold with $\varepsilon_{-1}/E_{\mathrm{vdW}} = 0$, the next one is found with the energy $\varepsilon_{-2}/E_{\mathrm{vdW}} = -39.5$, which only slightly depends on the exact shape of the short-range interaction potential. This is the exact setting of s-wave scattering resonances, which in our experiments are used for the creation of Efimov scenario. Since Efimov trimers are expected to emerge at energies $|E| \lesssim \min\left\{\left|E^{ij}_{\mathrm{vdW}}\right|\right\}_{ij}$, the smallest vdW energy scale predominantly creates modifications to the three-body bound state spectrum, while the others represent only slight perturbations. This is especially well fulfilled in the Li-Cs system, close to a Li-Cs Feshbach resonance (see Table 4.1). In this case the weakly bound LiCs dimer on the threshold gives rise to the Efimov series, while the next one is bound by energy $\varepsilon^{\mathrm{LiCs}}_{-2} \approx -39.5 E^{\mathrm{LiCs}}_{\mathrm{vdW}}$. Because $\left|\varepsilon^{\mathrm{LiCs}}_{-2}\right| \gg E^{\mathrm{CsCs}}_{\mathrm{vdW}}$ and, consequently, $\left|\varepsilon^{\mathrm{LiCs}}_{-2}\right| \gg |E|$, we expect that the deepest bound states of the Efimov spectrum at the interspecies resonance ($a_{\mathrm{LiCs}} \to \infty$) are largely dominated by the Cs-Cs vdW potential alone. If required, the Li-Cs interaction can be reintroduced via, for example, the second- and higher-order perturbation theory.

We apply the BO concept to the Li-Cs system by simulating the Cs-Cs interaction with one of the simplest vdW model potentials [Gribakin and Flambaum, 1993; Flambaum et al., 1999]. It is a hard-core vdW potential that reads

$$V_{\mathrm{CsCs}}(R) = \begin{cases} \infty, & R < R_0, \\ -C_6^{\mathrm{CsCs}}/R^6, & R > R_0, \end{cases} \tag{4.16}$$

where the cut-off distance R_0 is analytically connected to the Cs-Cs intraspecies scattering length a_{CsCs} via expression[5] [Gribakin and Flambaum, 1993; Flambaum et al., 1999]

$$\frac{N_{1/4}\left(2r^2_{\mathrm{vdW}}/R_0^2\right)}{J_{1/4}\left(2r^2_{\mathrm{vdW}}/R_0^2\right)} = 1 - \sqrt{2}\frac{a_{\mathrm{CsCs}}}{r_{\mathrm{vdW}}}\frac{\Gamma\left(5/4\right)}{\Gamma\left(3/4\right)}. \tag{4.17}$$

The advantage of this specific vdW model potential is not only the simplicity, with which the equation (4.11) for the heavy particle wavefunction can be solved numerically using, for example, the grid Numerov method [Pillai et al., 2012], but also the simple analytic relation between the parameters R_0 and a_{CsCs} that allows to test the numerical implementations.

The parameter R_0 determines not only a_{CsCs}, but also the number and energies of bound s-wave states. To illuminate the origin of the short-range deviations especially clearly we typically choose its value in such a range that the potential $V_{\mathrm{CsCs}}(R)$ supports only a single bound state. The exact number is largely irrelevant, as it results in almost identical long-range wavefunctions, and the increasing probability amplitude of the wavefunction in the range $R < r_{\mathrm{vdW}}$ with decreasing value of R_0 is small [Wang et al., 2012d]. As will be demonstrated in Sect. 4.3.4, already this sim-

[5] In this expression the CsCs superscript is omitted for clearer presentation, i.e. $r_{\mathrm{vdW}} = r^{\mathrm{CsCs}}_{\mathrm{vdW}}$.

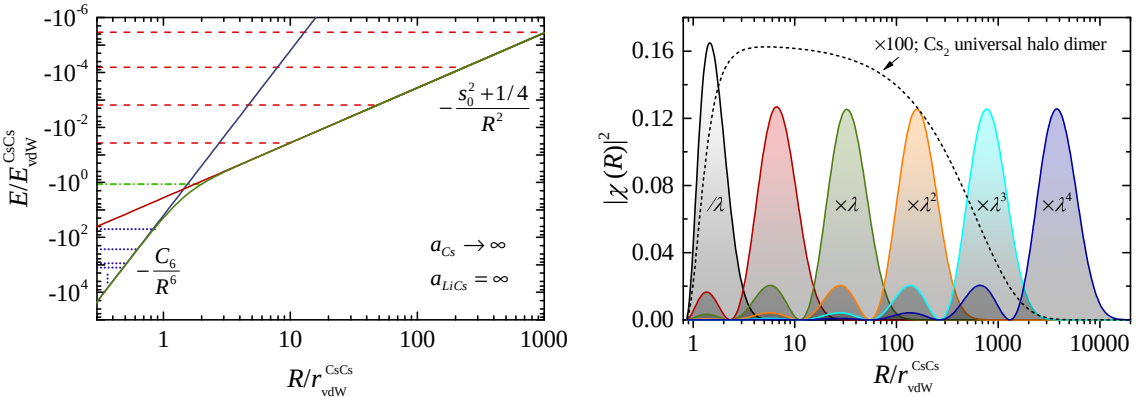

Figure 4.3: Left panel: The Cs-Cs Born-Oppenheimer potential (green solid line) of the radial Schrödinger equation for Cs atoms is composed of the long-range Li-mediated $-(s_0^2+1/4)/R^2$ (red solid line) and short-range Cs-Cs vdW (solid blue line) potentials. The resulting energies of the bound states are shown as horizontal lines in the vdW dominated (blue dotted), Efimovian dominated (red dashed) and transition (green dot-dashed) regime. Here, R_0 is tuned to yield a single bound Cs_2 dimer state and $a_{\mathrm{CsCs}} = 1.2{\times}10^5\ a_0$, limited by the size of the numerical grid. Four of the deeper bound universal vdW s-wave states are also shown (see text). Right panel: Scaled radial probability distributions of a few of the deepest trimer states with the same R_0 and $\lambda = e^{\pi/s_0} = 4.88$. The dashed line demonstrates the distribution of the universal Cs_2 halo dimer with binding energy $\varepsilon_{-1}^{\mathrm{CsCs}}/E_{\mathrm{vdW}}^{\mathrm{CsCs}} = 6.7{\times}10^{-7}$ in the case when the Li-mediated interaction is absent, which is the single state supported by the hard-core vdW Cs_2 potential. Once the Li-mediated interaction is added, the size and energy (green dash-dotted line in the left panel) of the universal dimer dramatically decreases.

plified approach delivers realistic energy spectra of three-body bound states in the resonant limit, while having the added benefit of transparent interpretation. Essentially similar results have been obtained by the complete adiabatic hyperspherical formalism and Lenard-Jones type potentials for heteronuclear [Wang et al., 2012d] and homonuclear [Wang et al., 2012a; Sørensen et al., 2012; Naidon et al., 2014b] systems.

The radial Schrödinger equation for the Li-Cs-Cs three-body problem is obtained by inserting Eq. (4.16) into Eq. (4.11), which for $a_{\mathrm{LiCs}} \to \infty$ and $R > R_0$ yields

$$-\frac{\hbar^2}{M_{\mathrm{Cs}}}\left(\frac{\partial^2}{\partial R^2} + \frac{s_0^2+1/4}{R^2} + \frac{\left(2r_{\mathrm{vdW}}^{\mathrm{CsCs}}\right)^4}{R^6}\right)\chi_{s_0}(R) = E\chi_{s_0}(R). \tag{4.18}$$

This equation can be solved numerically by standard methods [Giannozzi, 2014], while requesting that the wavefunction is normalizable; in other words, the probability amplitude $\chi_{s_0}(R)$ must vanish for $R \to \infty$ and $R < R_0$. For the here presented

results we solve Eq. (4.18) by transforming it in van der Waals units and utilizing a slightly modified version of the matrix Numerov method [Pillai et al., 2012] that is adapted for the use on a logarithmic grid following Ref. [Giannozzi, 2014].

In this way calculated energy spectrum and wavefunctions at the inter- and intraspecies unitarity are depicted in Fig. 4.3, where we have used the exact value of $s_0 = 1.98277$ for the Li-Cs mass ratio, and set $R_0 = 0.847936\, r_{\mathrm{vdW}}^{\mathrm{CsCs}}$, which according to Eq. (4.17) yields[6] $a_{\mathrm{CsCs}} = 1216.923\, r_{\mathrm{vdW}}^{\mathrm{CsCs}}$. It illustrates the basic mechanism behind the scaling modifications of the geometrical Efimov spectrum in a BO system with separable energy scales. In the scale-invariant region the potential is dominated by the Li-mediated interaction that gives rise to the geometrical progression of Efimov states with the expected scaling factor $e^{2\pi/s_0} = 23.8$ between consecutive energy levels. The deviation from the ideal $\propto -1/R^2$ potential at distances $R \sim r_{\mathrm{vdW}}^{\mathrm{CsCs}}$ is caused by the vdW tail of the Cs_2 molecular potential and the coupling to the most weakly-bound dimer state. Interestingly, the addition of the Li-mediated potential leads to a significant increase of the universal Cs_2 halo dimer binding energy, and, consequently, smaller extension of its wavefunction, which now also acquires a strong Efimovian character, evident by its similarity to the $LiCs_2$ Efimov states. This behavior for a_{CsCs} away from the intraspecies resonance is investigated in Sect. 4.3.4.

4.3 Observation of $LiCs_2$ Efimov resonances with tunable Cs background scattering length

Having found both, the universal Efimov scenario and deviations from it in Sect. 3.4.4, the next natural step is to investigate if this behavior can be explained with the inclusion of the vdW pairwise interactions that better reproduce the short-range behavior of the three-body system (see Sect. 4.2). This scenario can be tested at different interspecies Feshbach resonances, at which the intraspecies background scattering length has various values. In this section we explore these questions in the Li-Cs system. We start by comparing the previously discussed recombination spectra with a hyperspherical calculation that is based on Lennard-Jones (LJ) potentials, and recovers the deviations from the ideal scaling in Sect. 4.3.1. Then we present new measurements at the 889 G Li-Cs Feshbach resonance that are characterized with a different Cs-Cs background scattering length in Sect. 4.3.2. Finally, the differences between both series of measurements and their connection to the short-range Cs-Cs vdW potential are discussed in Sect. 4.3.3 and 4.3.4.

[6] Larger values are limited by the finite grid size of the utilized numerical method.

4.3.1 Recombination spectra at negative a_{CsCs}

We start our investigation of $LiCs_2$ Efimov resonance shifts due to finite-range effects by the three-body recombination spectroscopy, as already discussed in chapter 3. We employ the interspecies Feshbach resonance at 843 G, at which the Cs-Cs background scattering length $a_{\mathrm{CsCs}} \approx -1500\ a_0$ is large and negative. More specifically, at the positions of the $LiCs_2$ Efimov resonances the respective values of a_{CsCs} are $-1550\ a_0$, $-1490\ a_0$, and $-1180\ a_0$ [Berninger et al., 2013], in the order of increasing $LiCs_2$ trimer binding energy.

In contrast to the universal zero-range theory that was employed in Sect. 3.4.4, here we analyze the loss-rate spectrum with the adiabatic hyperspherical formalism (see Sect. 3.2.1) that employs Lennard-Jones (LJ) type potentials to describe binary interaction between each pair of atoms [Wang et al., 2012d; Wang and Greene, 2015]. These model potentials are constructed in such a way that they support a single two-body bound state and reproduce the respective scattering lengths a_{LiCs} and a_{CsCs}. Since for a single Efimov series the Cs-Cs background scattering length changes only slightly, in the model calculations it is used as a constant. As will be also discussed in Sect. 4.3.4 this is a reasonable approximation because in the relevant scattering length range its influence on the Efimov energy spectrum is minimal.

In contrast to the thermally averaged zero-range model, the calculations with the LJ potentials are much more involved, because of the additional degrees of freedom. Thus a fitting procedure, similar to the approach in Sect. 3.4.4 is exceptionally challenging. Therefore these calculations utilizes a predetermined set of parameters that is reasonably optimized to reproduce the measurements. The only free parameters are the temperature of the relative energy distribution and the coupling strength to an additional hyperradial channel that is used to adjust the width of the resonant features. The Cs-Cs vdW potential is tuned to yield $a_{\mathrm{CsCs}} = -1500\ a_0$, in accordance with the magnetic field range where the experimentally employed Li-Cs Feshbach resonance is found.

These results are summarized in Fig. 4.4 that uses the same data points[7] and experimental approach, as in Sect. 3.4.4 presented Fig. 3.14. Both, the numerically obtained recombination spectra and the Efimov resonance positions (see Sect. 4.3.3) describe the experimental findings well. Remarkably, the model with pairwise LJ potentials recovers not only the excited state, but also the ground state positions of $LiCs_2$ Efimov resonances, in stark contrast to the zero-range model that was employed in Sect. 3.4.4. This illustrates the important role the finite-range physics is playing for the deepest bound trimer state formation. The energy spectrum of the ground Efimov state is strongly influenced by the vdW potential, which results

[7] We use the fitted absolute rates for the different data sets $\gamma_{120}^{(a)} = 2.26$, $\gamma_{120}^{(b)} = 1.44$, $\gamma_{450} = 0.73$ so that the LJ and zero-range models can be directly compared. See Sect. 3.4.4.

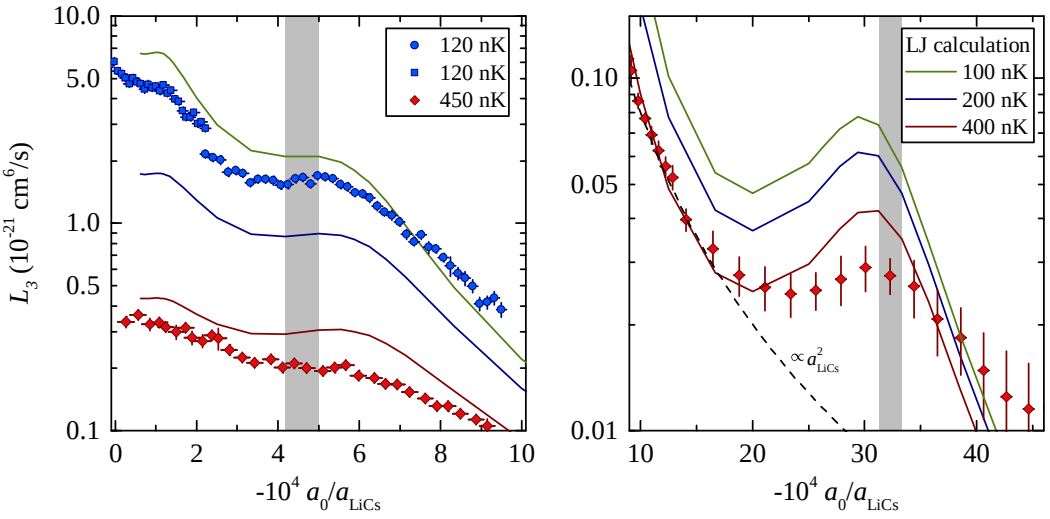

Figure 4.4: Li-Cs-Cs three-body loss rate spectra at a temperature of 120 nK (blue squares and circles) and 450 nK (red diamonds) close to the 843 G Li-Cs Feshbach resonance in scattering channel $|\alpha\rangle$ and Cs-Cs background scattering length $a_{\mathrm{CsCs}} \approx -1500\ a_0$. The error bars represent the statistical errors that are obtained from bootstrapping (see Sect. 3.4.4), magnetic field uncertainty, and the mapping of the magnetic field to the scattering length. Solid lines show the numerically obtained result with the Lennard-Jones potentials at a temperature of 100 nK (green lines), 200 nK (blue lines), and 400 nK (red lines) [Wang and Greene, 2015]. The Efimov resonance positions are given as gray areas that are extracted from the calculated trimer energy spectra (see Fig. 4.6 and Sect. 4.3.3). The scaling law $\propto a_{\mathrm{LiCs}}^2$ (dashed line) is drawn as a guide to the eye (see Sect. 4.3.2).

in a shift of the three-body recombination resonance. The excited states, within the experimental uncertainties, are not affected.

The theory and data reasonably agree in the unitarity limit, close to the pole of the Feshbach resonance, however, there is a slight discontinuity between the two 120 nK data sets. This difference is not significant, since the systematic error of the experimental three-body loss rates is a factor of three (see Sect. 3.4.2), thus it is well within the experimental uncertainties. The long-term drifts[8] of the laser-beam pointing that generate the bichromatic dipole trap may introduce additional changes in the optical potential depth and, consequently, sample temperature that is on the order of 30%. Furthermore, such effects mostly contribute to the absolute loss rate, while the slopes for both, the 120 nK and 450 nK data sets are not entirely reproduced by the calculation. This may result in higher fitted temperatures, and indicates that at these scattering lengths additional loss processes

[8]The recording of a single three-body recombination spectrum can take a few days of continuous operation.

may contribute, for example, four-body recombination. As discussed in Sect. 4.3.2, $LiCs_3$ tetramer resonances are expected to emerge at scattering lengths that are universally connected to the trimer resonance positions [Blume and Yan, 2014]. Depending on their width, this may lead to enhanced loss rates between consecutive Efimov resonances that are faster than the ones in a pure three-body scenario. Currently, however, we cannot verify this assumption, since our fitting procedure does not distinguish between three- and four-body recombination in the present data (see Sect. 4.3.2). Additionally, we estimate [Mudrich et al., 2002; Silber et al., 2005] that for our experimental parameters the thermalization rate of Li atoms at scattering lengths on the order of $a_-^{(1)}$ is only a factor of ~ 2 higher than the loss rate. This may lead to a complicated, non-thermal energy distribution, for which the present functional dependence of the three-body loss curve would be weakened.

4.3.2 Recombination spectra at positive a_{CsCs}

One of the major advantages of a heteronuclear three-body system consisting of two like and one distinguishable atom is the ability to almost independently change the inter- and intraspecies scattering length. Thus, after having observed the short-range induced modifications the Li-Cs-Cs three-body problem at a single and negative a_{CsCs} value, the next question that arises is how the interspecies Efimov spectrum depends on the intraspecies background scattering length a_{CsCs}. We imagine a situation, in which a_{CsCs} is fixed to different constant values, while a_{LiCs} is tuned to generate the Efimov scenario.

Therefore we turn our attention to the broad Li-Cs s-wave Feshbach resonance at 889 G in the two-body scattering channel $|\beta\rangle$ (see Sect. 2.4). At these magnetic field values the Cs-Cs background scattering length $a_{\mathrm{CsCs}} \approx 190\ a_0$ is positive and only about a factor of two larger than $r_{\mathrm{vdW}}^{\mathrm{CsCs}}$, while a_{LiCs} can be easily tuned from large negative to large positive values. We use the approach described in Sect. 3.3.2 and 2.3.1 to prepare the mixture at a temperature of 120 nK and 320 nK, respectively. For the latter case we measure different Li and Cs gas temperatures $T_{\mathrm{Li}} = 360$ nK and $T_{\mathrm{Cs}} = 280$ nK, however, we refer to this data set as 320 nK for simplicity. After the preparation we record the temporal evolution of Li and Cs atoms numbers as a function of the external magnetic field. As in all previous measurements, we choose the next magnetic field value at which to perform the experiment randomly. We extract the three-body loss rates and their uncertainties in a procedure, which is identical to the one that is described in Sect. 3.4.4. In analogy to the experiments close to the 843 G FR in Li-Cs scattering channel $|\alpha\rangle$, we determine the intraspecies one- and three-body loss rates K_1^{Li}, K_1^{Cs}, and K_3^{Cs} independently (see Sect. 3.4.2), with conditions that are identical to the interspecies measurements. This reduces the number of free fitting parameters to three: the initial number of atoms $N_{\mathrm{Cs},0}$, $N_{\mathrm{Li},0}$,

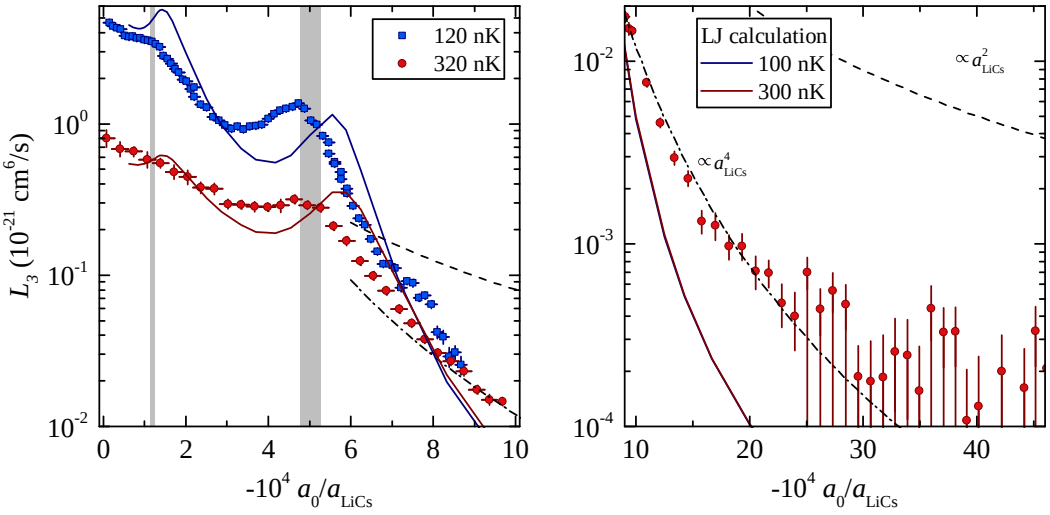

Figure 4.5: Li-Cs-Cs three-body loss rate spectra at a temperature of 120 nK (blue squares) and 320 nK (red circles) close to the 889 G Li-Cs Feshbach resonance in scattering channel $|\beta\rangle$ and Cs-Cs background scattering length $a_{CsCs} \approx 190\ a_0$. The error bars represent the statistical errors arising from bootstrapping (see Sect. 3.4.4), magnetic field uncertainty, and the mapping of the magnetic field to the scattering length. Solid lines show a numerically obtained result with the Lennard-Jones potentials at a temperature of 100 nK (blue lines) and 300 nK (red lines) [Wang and Greene, 2015]. The Efimov resonance positions are given as gray areas that are extracted from the calculated trimer energy spectra (see Fig. 4.6 and Sect. 4.3.3). The scaling laws $\propto a_{LiCs}^2$ (dashed line) and $\propto a_{LiCs}^4$ (dashed-dotted line) are drawn as a guide to the eye.

and the three-body loss rate K_3, form which L_3 is calculated (see Eq. (3.28) and Sect. 3.4.2). Also in this case the numerical fit (analogous to Fig. 3.13) excellently reproduces the temporal evolution of atom numbers, which verifies that within our experimental uncertainties the employed model of coupled rate equations includes all of the dominating recombination processes.

The resulting scattering length dependence of the three-body loss rate is shown in Fig. 4.5, where we have used the values from Table 2.1 to convert from magnetic field into scattering length. The spectra at 320 nK and 120 nK temperatures reveal one and two pronounced resonance features, respectively, which we identify as $LiCs_2$ excited state Efimov resonances, according to the employed rate equation model. Intriguingly, the first Efimov resonance emerges at a scattering length that is about a factor of five larger than the ground state Efimov resonance that was observed close to the Li-Cs Feshbach resonance at 843 G. This is another manifestation of the short-range vdW physics that will be discussed in Sect. 4.3.3 and 4.3.4. For large values of a_{LiCs}, i.e. $(a_0/a_{LiCs} \to 0)$, the three-body loss rate approaches the unitarity limit, similar to the observations at the 843 G Feshbach resonance. The maximal loss rate is consistent with the estimation given by Eq. (3.29), which yields

$L_3^{\mathrm{un,320nK}} = 7.5 \times 10^{-22}$ cm^6/s and $L_3^{\mathrm{un,120nK}} = 5.3 \times 10^{-21}$ cm^6/s. We determine the lower, reliable limit for the L_3 extraction (see Eq. (3.30)) to be $L_3^{lim,120\mathrm{nK}} \sim 2{\times}10^{-23}$ cm^6/s and $L_3^{lim,320\mathrm{nK}} \sim 2.5{\times}10^{-25}$ cm^6/s for the data sets at 120 and 320 nK, respectively. Thus, the data points for values $-10^4 a_0/a_{\mathrm{LiCs}} > 25$ represent the upper bound of the actual L_3 rate, as given by the error bars that extend till zero.

The general L_3 dependence on the Cs background scattering length a_{Cs} reasonably agrees not only with the hyperspherical calculation (see below), but also with the scaling laws of the three-body collision rates near overlapping FRs [D'Incao and Esry, 2009] that are shown in Fig. 4.5 and 4.4 as guides to the eye. In both of the figures we have used the same numerical prefactors, such that they can be directly compared. Each loss rate spectrum corresponds to one of two distinctive cases of three-body scattering. The one near the 889 G FR (Fig. 4.5) can be characterized by $|a_{\mathrm{LiCs}}| \gtrsim a_{\mathrm{Cs}}$, for which $L_3 \propto a_{\mathrm{LiCs}}^4$, whereas the one near the 843 G FR (Fig. 4.4) for small a_{LiCs} corresponds to $|a_{\mathrm{LiCs}}| \lesssim |a_{\mathrm{Cs}}|$, and therefore $L_3 \propto a_{\mathrm{LiCs}}^2$. Since the experimental scattering lengths only approximately recapture the limits imposed in theory, especially in the latter case, these scaling laws can only represent a limiting behavior. Nevertheless, qualitative agreement is evident. Close to the pole of the FR the theoretical scaling does not apply anymore because of the unitarity limit. Similar behavior that depends on different values of a_{CsCs} has been observed in more elaborate theoretical models based on optical potentials [Mikkelsen et al., 2015] and S-matrix formalism [Petrov and Werner, 2015].

Within the limitations of the theoretical description, Fig. 4.5 displays good agreement between the observed and calculated Li-Cs-Cs recombination rates. Here, the same model calculation as already introduced in Sect. 4.3.1 is used, where the only free parameter is the relative temperature between the colliding atoms. Analogous to the case at a negative a_{CsCs}, the scaling factor and the overall amplitude of the three-body rates are well reproduced. The positions of the measured recombination features agree well with the ones at which the Efimov states cross the three-body dissociation threshold, given as gray areas (see Sect. 4.3.3). The slight shift, on the order of $\sim 20\%$ of $a_-^{(1)}$, between the numerically and experimentally determined recombination resonances may be a possible indication of the multichannel nature of the Li-Cs Feshbach resonance that is employed to tune a_{LiCs}, however, a more thorough investigation is required to verify its exact origin. It has recently been shown for homonuclear systems that the inclusion of a second and even third two-body spin channel can be necessary to quantitatively reproduce experimental findings [Wang et al., 2014]. At the present moment, however, equivalent approaches for the heteronuclear case, which would treat the short-range pairwise interactions more realistically, are missing and pose a challenge for the theory that is well beyond the scope of this thesis.

Therefore, let us resort to the simplified determination of the $LiCs_2$ Efimov reso-

Table 4.2: Estimation of $LiCs_2$ Efimov resonance positions close to the 889 G interspecies Feshbach resonance in the scattering channel $|\beta\rangle$ at a temperature of 120 nK. The values in the first and second parenthesis always represent the statistical and systematic error from the fit, respectively. For $a_-^{(n)}$ and scaling factors $a_-^{(n)}/a_-^{(n-1)}$ the error in the third parenthesis denotes the uncertainty arising from the $a(B)$ mapping through the Feshbach resonance parameters given in Sect. 2.4.3. a_{CsCs} is obtained from the parametrization given in Ref. [Berninger et al., 2013].

n	Magnetic field (G)	$a_-^{(n)}$ (10^3 a_0)	$a_-^{(n)}/a_-^{(n-1)}$	a_{CsCs} (a_0)
1	889.386(10)(16)	-2.13(3)(4)(7)	-	195
2	888.781(10)(16)	-8.41(41)(66)(97)	3.94(20)(32)(34)	183

nance positions to quantify the experimental findings, as already done in Sect. 3.4.3. We fit the spectrum in magnetic field units with a Gaussian profile with a linear background. Only the 120 nK data are employed in order to minimize position shifts due to finite temperature effects. The results of this fitting procedure are presented in Table 4.2. We list the corresponding scattering lengths $a_-^{(n)}$, at which the $n-$th three-body Efimov state merges with the scattering threshold, the corresponding scaling factors $\lambda_n = a_-^{(n)}/a_-^{(n-1)}$, and the magnitude of the background scattering length a_{CsCs}. We start the numbering of the Efimov resonances with $n = 1$, and reserve the index $n = 0$ for the ground Efimov state. It will become clear in Sect. 4.3.3 and 4.3.4 that the ground Efimov state is still present, however it does not appear in the three-body scattering channel, but instead, as an atom-dimer recombination resonance at the $\mathrm{Li} + \mathrm{Cs}_2$ dissociation threshold. Clearly, the extracted scaling factor of $\lambda_2 = 3.94$ for the second Efimov period can be strongly influenced by finite temperature effects and the oversimplified fitting model that is used to extract the resonance positions, and can be used only as an order of magnitude estimate of the actual one. Nevertheless, a significantly better approach of characterizing the Efimov spectrum that is discussed in Sect. 4.3.3, delivers a scaling factor of 4.25, which is also reduced in comparison to the universal value of ≈ 4.9. This is another indication of the finite-range influence on the properties of the deepest bound Efimov states.

Finally, it is interesting to note that the slim increase of the three-body loss rates around $-10^4 a_0/a_{\mathrm{LiCs}} \approx 7.8$, i.e. $a_{\mathrm{LiCs}} \approx 0.6\ a_-^{(1)}$, at a temperature of 120 nK (see left panel of Fig. 4.5) may indicate a recombination resonance of a $LiCs_3$ tetramer state merging with the four-body scattering threshold. The position is in good agreement with the theoretical prediction of $0.55\ a_-^{(1)}$ [Blume and Yan, 2014]. The second tetramer, which is expected to appear at $0.91\ a_-^{(1)}$, would already overlap with the trimer recombination resonance and thus the observed loss features might include

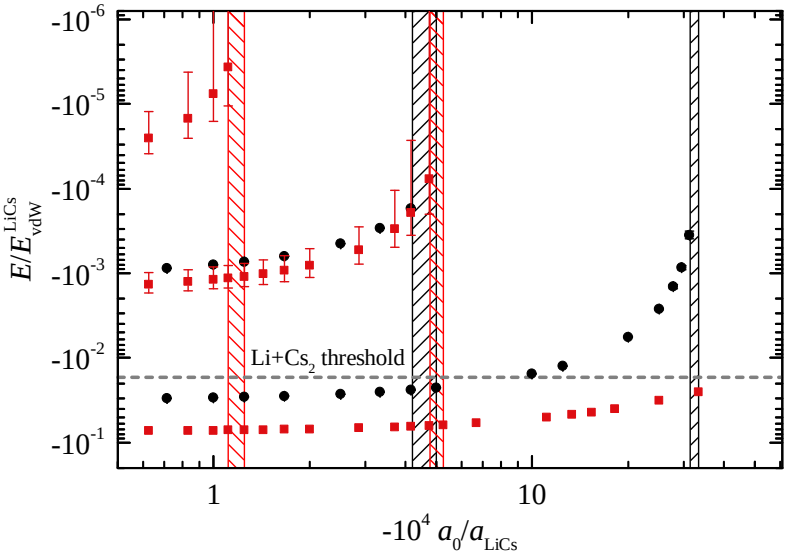

Figure 4.6: $LiCs_2$ trimer binding energy spectra as a function of a_{LiCs} for $a_{\mathrm{CsCs}} = -1500\ a_0$ (black circles) and $a_{\mathrm{CsCs}} = 200\ a_0$ (red squares) that correspond to the 843 G and 889 G Li-Cs Feshbach resonance, respectively. The error bars indicate the width of the respective Efimov state. The hatched areas give the range in which each Efimov state crosses the three-body dissociation threshold and becomes unbound. The atom-dimer dissociation threshold Li+Cs2 for $a_{\mathrm{CsCs}} = 200\ a_0$ is shown as dashed line. The trimer binding energies courtesy of Y. Wang and C. Greene [Wang and Greene, 2015].

contributions from four-body process. This, however, we cannot unambiguously validate at this point since an analogous fitting model to the one given by Eqs. (3.23) and (3.24) with additional four-body loss terms does not improve the overall quality of the fit and yields no pronounced features in the four-body loss-rate spectrum.

4.3.3 Efimov resonance positions from the hyperspherical formalism

A significantly better approach in the determination of the Efimov resonance positions is the use of the points at which the calculated trimer binding energies cross the three-body dissociation threshold. In this way the influence of finite temperature shifts is reduced to the minimum. Corresponding $LiCs_2$ trimer spectra as a function of a_{LiCs} for $a_{\mathrm{CsCs}} = 200\ a_0$ and $a_{\mathrm{CsCs}} = -1500\ a_0$ are shown in Fig. 4.6 [Wang and Greene, 2015], from which we extract the recombination resonance positions as the average values of the two numerical grid points between which the three-body states become unbound. This procedure yields $a^{(1)}_{-,200} = (-2000 \pm 100)\ a_0$, $a^{(2)}_{-,200} = (-8500 \pm 500)\ a_0$, $a^{(0)}_{-,-1500} = (-310 \pm 10)\ a_0$, and $a^{(1)}_{-,-1500} = (-2200 \pm 200)\ a_0$ for Li-Cs interspecies scattering length, where the value after the $\pm$ sign represents

half the step size of the local grid and the second index gives the a_{CsCs} that were used in the calculation. These positions are illustrated in Fig. 4.5 and 4.4 as the vertical gray areas and show excellent agreement with the measured recombination resonances.

Encouraged by the consistent picture, we use the calculated Efimov resonance positions to extract the corresponding scaling factors, which yields $\lambda_{2,200} = 4.25^{+0.49}_{-0.44}$, and $\lambda_{1,-1500} = 7.10^{+0.90}_{-0.85}$, where we have used the convention $\lambda_{n,a_{\mathrm{CsCs}}} = a^{(n)}_{-,a_{\mathrm{CsCs}}}/a^{(n-1)}_{-,a_{\mathrm{CsCs}}}$. They are close to the predictions of the universal theory, which gives $\lambda = 4.9$ for $LiCs_2$ Efimov trimers with two resonant interactions [Braaten and Hammer, 2006; D'Incao and Esry, 2006] (see also Sect. 3.2.2). The deviations in $\lambda_{1,-1500}$ and $\lambda_{2,200}$ from the ideal scaling factor ≈ 4.9 can be attributed to the van der Waals interaction potential giving rise to a finite probability amplitude of the three-body wavefunction in the short-range region. At the same time, $\lambda_{1,-1500}$ differs from the results obtained by the simplified fitting procedure in Sect. 3.4.3, however, these variations are not significant, since different approaches are used to extract them.

The short-range physics in the current setting manifests in another, surprising way. As shown in Fig. 4.6, the ground state Efimov resonance for $a_{\mathrm{CsCs}} = 200\ a_0$ dissolves in the scattering continuum after crossing the Li+Cs_2 breakup threshold at $-10^4 a_0/a_{\mathrm{LiCs}} \approx 35$. This is in strong contrast to the case of $a_{\mathrm{CsCs}} = -1500\ a_0$, which does not support a weakly bound Cs_2 state. Here, the energy of the bound trimer state reaches the three-body dissociation threshold. Thus, consistent with the experimental findings, the atom-dimer dissociation threshold prevents the observation of the ground Efimov resonance near to the 889 G Feshbach resonance.

This behavior is a result of an avoided crossing originating from the coupling between the attractive three-body potential and a repulsive atom-dimer channel [Wang and Greene, 2015]. The adiabatic three-body potential is effectively repulsive and displays a barrier around $\sim 2r^{\mathrm{CsCs}}_{\mathrm{vdW}}$, which prevents the scattering wavefunction from probing short-range parts of the potential and, consequently, recombination. Such an avoided crossing is not present for $a_{\mathrm{Cs}} = -1500\ a_0$, thus providing with a consistent picture with the experimental recombination rate spectra and the calculated Efimov trimer energies. According to the model calculations with the LJ potentials the ground state trimer resonance for $a_{\mathrm{CsCs}} = 200\ a_0$ can be observed in the atom-dimer scattering channel [Wang and Greene, 2015].

4.3.4 Crossover between the vdW and Efimov regimes

The heteronuclear Efimov scenario in ultracold Li-Cs-Cs system displays a qualitatively different nature depending on the intraspecies background scattering length. The behavior of the ground Efimov state is an illustration of this. At $a_{\mathrm{CsCs}} = 200\ a_0$ the ground trimer state merges with the atom-dimer dissociation threshold Li+Cs_2

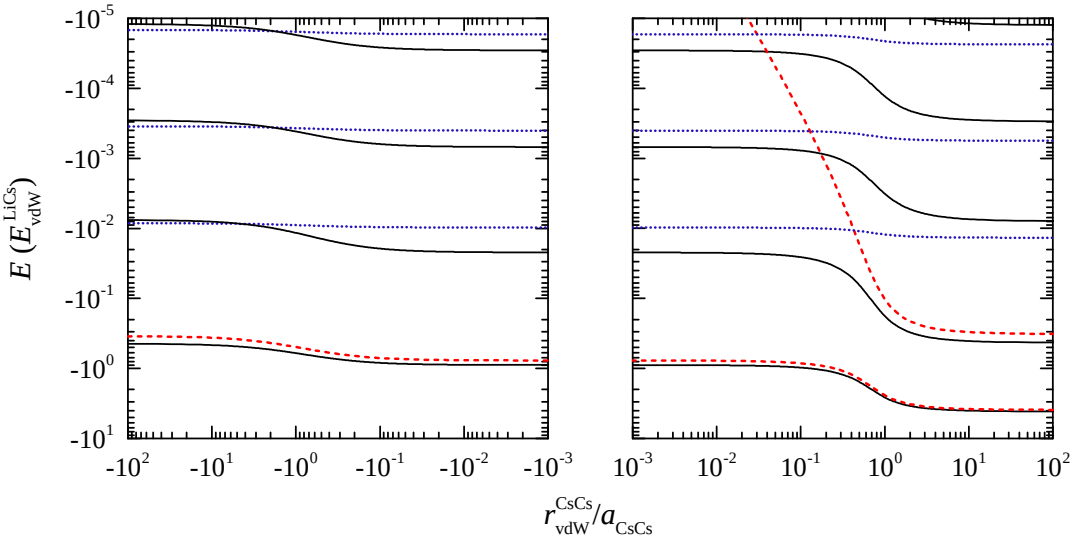

Figure 4.7: Born-Oppenheimer energy spectrum of the total potential (case (iii), black solid lines), and the comparison to the energy spectra of individual van der Waals (case (i), red dashed lines) and Efimov (case (ii), blue dotted lines) potentials for the Li-Cs-Cs system at the heteronuclear unitarity.

and disappears in the scattering continuum. In this case the three-body recombination resonance in the scattering channel $|\beta\rangle$ was absent. In contrast, at $a_{\mathrm{CsCs}} = -1500\ a_0$ there are no such thresholds, since all the scattering lengths are large and negative. Therefore the ground Efimov state could be observed as a recombination resonance at the three-body dissociation threshold in scattering channel $|\alpha\rangle$.

The exact mechanism of how these two qualitatively different behaviors are connected via the Cs-Cs background scattering length for the Li-Cs-Cs three-body system can be illuminated by the minimalistic BO model that was introduced in Sect. 4.2.2. Therefore, we numerically solve Eq. (4.18) in three distinct cases:

(i) with the Cs_2 van der Waals potential $-C_6^{\mathrm{CsCs}}/R^6$ only,

(ii) with the Li-mediated Efimov potential $-(s_0 + 1/4)/R^2$ only,

(iii) with the total BO potential consisting of both, the Efimov and vdW parts.

In order to obtain a direct comparison we always choose the same value of the cut-off parameter R_0 that we associate with the particular value of a_{CsCs} by Eq. (4.17), and use the exact value of $s_0 = 1.98277$ for the Li-Cs mass ratio. By repeating this procedure for different values of R_0 we calculate the energy spectra as a function of a_{CsCs} for each of the cases (i)-(iii).

These calculations are summarized in Fig. 4.7. The case (i) represents a pure Cs_2 two-body problem. For large and positive a_{CsCs}, as approaching the pole of the Cs-Cs scattering resonance, the binding energy E_b of the most weakly bound

dimer follows the universal relation $E_b \propto -1/a_{\mathrm{CsCs}}^2$, which was also discussed in Sect. 2.2.3. The second Cs_2 bound state crosses the resonance and becomes the most weakly bound state at negative a_{CsCs}. The gradual step in its binding energy around the values $a_{\mathrm{CsCs}} \approx r_{\mathrm{vdW}}^{\mathrm{CsCs}}$ demonstrates the qualitative change of the nature of the least bound Cs_2 dimer, which develops from a vdW-dominated into a halo state for $a_{\mathrm{CsCs}} < r_{\mathrm{vdW}}^{\mathrm{CsCs}}$ and $a_{\mathrm{CsCs}} > r_{\mathrm{vdW}}^{\mathrm{CsCs}}$, respectively.

The case (ii) represents a pure Efimov scenario in the zero-range BO approach that was discussed in Sect. 4.2.1. Here, however, the divergence of the $\propto -1/R^2$ potential at short-distance region has been alleviated with the hard-wall cut-off at distance R_0, thus the energies of the quantized levels are well defined. The scaling between consecutive energy levels follows the expected factor $e^{2\pi/s_0} = 23.8$. Remarkably, the absolute values of the energies show only minor dependence on the exact position of the parameter R_0.

The case (iii) corresponds to the short-range BO scenario for heavy-heavy-light three-body systems that was discussed in Sect. 4.2.2. The energy spectrum clearly illustrates the transition between the two limiting cases (i) and (ii). As $r_{\mathrm{vdW}}^{\mathrm{CsCs}}/a_{\mathrm{CsCs}}$ is decreased from large positive values, over the pole of the Cs-Cs scattering resonance, to large negative values, the energy of the deepest bound state closely follows the one from the Cs_2 two-body problem for all a_{CsCs}. Therefore we assign it to the second bound vdW s-wave dimer (see Sect. 4.2.2). The next bound state, however, starts as an approximate Cs_2 dimer state, but due to the additional Li-mediated interaction stays bound also for negative a_{CsCs}. This is a signature of the Li-Cs-Cs Efimov effect, because in the absence of the Li-mediated part of the potential this state would merge with the scattering continuum at $a_{\mathrm{CsCs}} = \infty$, as in case (ii). For large, negative values of a_{CsCs} it approaches the ground state energy of the pure Efimov scenario. Since this indicates a qualitative change in the character from the vdW dimer into a three-body Efimov state we call it the crossover state. The even less bound states that are present in the combined potential correspond to the three-body Efimov states. In comparison to case (ii) their energy dependence on a_{CsCs} develops a smooth step around $a_{\mathrm{CsCs}} \sim r_{\mathrm{vdW}}^{\mathrm{CsCs}}$. Since the only modification is the inclusion of Cs_2 vdW potential, we attribute this change to the Cs_2 halo dimer, which now due to the large wavefunction overlap is strongly coupled to the Efimov states.

The crossover between the vdW and Efimov physics dominated regimes is one of the most intriguing aspects of the simplified BO picture. It indicates that the nature of the three-body system undergoes a transition from a short-range into a long-range state[9]. A quantitative characterization of this gradual change is given in Fig. 4.8. We use two criteria to quantify it:

[9]Even more provocative and pictorial comparison, although not strictly correct, is a continuous transition from a two-body into a three-body bound state.

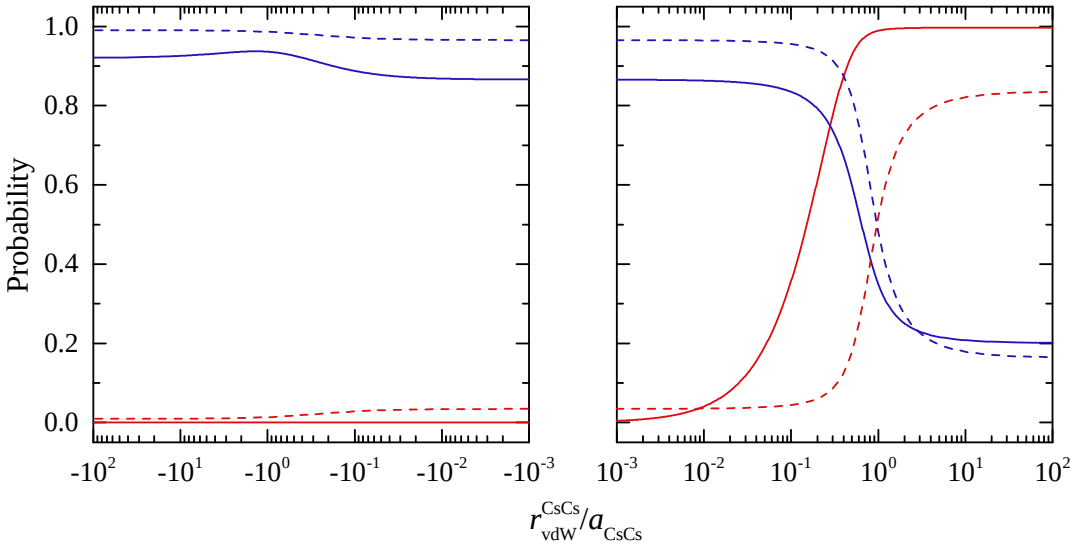

Figure 4.8: The crossover between Efimov (blue) and vdW (red) characters as a function of a_{CsCs}. The solid and dashed lines shows the type a) and b) criteria, respectively (see text). Here the same parameters as in Fig. 4.7 are used to tune a_{CsCs}.

a) The probability of finding the two heavy particles at distances closer or further than $r_{\mathrm{vdW}}^{\mathrm{CsCs}}$. The spatial extension of an Efimov trimer or an vdW s-wave dimer state, with the exception of the halo state, is typically much larger or smaller than the vdW length scale, respectively. We integrate the radial BO wavefunction $\chi_0(R)$ (see Sect. 4.2.2) of the crossover state within these limits, which yields integrals

$$I_{\mathrm{vdW}} = \int_{R_0}^{r_{\mathrm{vdW}}^{\mathrm{CsCs}}} \chi_0^2(R)dR \quad \text{and} \quad I_{\mathrm{Efimov}} = \int_{r_{\mathrm{vdW}}^{\mathrm{CsCs}}}^{\infty} \chi_0^2(R)dR, \tag{4.19}$$

that we attribute to the respective vdW and Efimov characters[10].

b) The similarity between the radial wavefunction of the crossover state and the respective basis wavefunctions $\chi_{i,\mathrm{Efimov}}(R)$ or $\chi_{i,\mathrm{vdW}}(R)$ of the pure Efimov or vdW scenario, where the subscript i indexes the bound state in the corresponding potential. We calculate the sum of overlap integrals between $\chi_0(R)$ and each of the basis sets from the expression

$$S_{\varpi} = \sum_i |\langle \chi_{i,\varpi}(R) | \, \chi_0(R) \rangle|^2 , \tag{4.20}$$

where ϖ denotes either Efimov or vdW case (i) or (ii), respectively.

[10] We thank C. Greene for suggesting this idea to us.

Both of these criteria deliver consistent pictures. At small and negative a_{CsCs} the character of the three-body crossover state is governed by the Efimov part of the total BO potential. The Li-mediated potential, and hence the interaction between the Li and Cs atoms is dominating. The state preserves this character as the intraspecies scattering length is tuned over the pole of the resonance and for large positive values of a_{CsCs}. When a_{CsCs} approaches $r_{\mathrm{vdW}}^{\mathrm{CsCs}}$ the contributions of the vdW part of the BO potential become significant. In this regime the trimer state is mostly dominated by the vdW tail of the Cs_2 molecular potential.

It is important to note that the three-body spectrum obtained in case (iii) closely resembles the characteristic vdW-universal behavior of a heteronuclear heavy-heavy-light Efimov scenario [Wang et al., 2012d]. Although Wang et al. [2012d] do not discuss the crossover process, their calculations, which were performed with LJ potentials based BO approximation and adiabatic hyperspherical formalism, reveal qualitatively similar behavior of the weakly bound Efimov state spectrum [Wang and Greene, 2015]. This verifies that our simplified BO approach recovers the main features of the vdW and Efimov physics. Nevertheless, at the point of writing this thesis, there are slight discrepancies between the absolute values of energies that the two model calculations deliver (see Fig. 4.9). The BO spectrum is reproduced by the hyperspherical calculation for positive a_{CsCs}, while for negative a_{CsCs} deviations on the order of $\sim 30\%$ can be observed. This may originate from the employed different vdW model potentials, neglected couplings to additional hyperspherical channels, and the exclusion of the Li-Cs short-range vdW interaction, which is replaced by the zero-range contact potentials in the simplified BO model. The characteristic vdW length scale is $r_{\mathrm{vdW}}^{\mathrm{LiCs}} = 45\ a_0$, only a factor of ≈ 2 smaller than the Cs-Cs one. The latter approach yields the energy spectrum on the pole of the heteronuclear scattering resonance, while the experimental observations in our experiment are performed at the three-body scattering threshold. Therefore, for a quantitative comparison with the experiment the hyperspherical approach should be used, as already demonstrated in Sect. 3.4.4, 4.3.1 and 4.3.2.

Despite this, let us compare the results from the short-range BO model with our experimental findings and the LJ model calculation to quantify this approximation. In Fig. 4.9 we show the calculated BO three-body energy spectrum at the heteronuclear scattering resonance for the trimer states with significant Efimov character. The scaling factor $\lambda_{n>1}^2 \approx 24.0$ between consecutive trimer energy levels approaches the expected universal value $\lambda_{n\to\infty}^2 = e^{2\pi/s_0} = 23.8$ already for the second Efimov period. Notably, the deepest bound state deviates from the ideal scaling series and acquires larger $\lambda_{n=1}^2 = 32.2$ at the intraspecies resonance, but rapidly approaches the universal value as soon as the ratio $r_{\mathrm{vdW}}^{\mathrm{CsCs}}/a_{\mathrm{CsCs}}$ is decreased below -10. This is consistent with the experimentally found simplified scaling factors at the three-body scattering threshold, which give $\lambda_{n=1}^2 = 30.0(2.2)$ and $\lambda_{n=2}^2 = 25.0(15.3)$ for

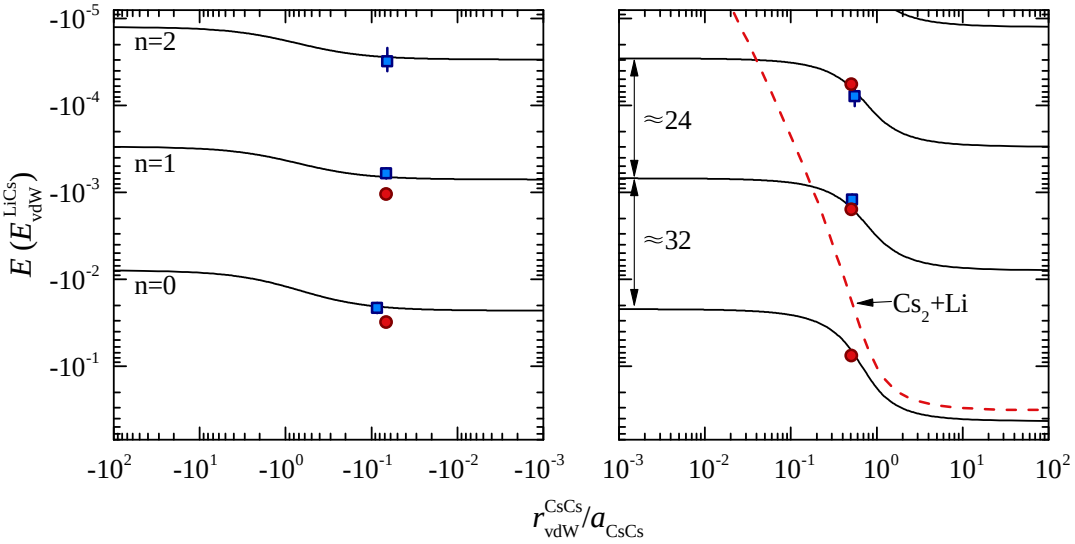

Figure 4.9: The LiCsCs three-body energy spectrum at the heteronuclear scattering resonance ($a_{\mathrm{LiCs}} = \infty$) as a function of a_{CsCs}. The solid lines are solutions of Eq. (4.18) for case (iii) and the points (blue squares) are mapped from the Li+Cs+Cs recombination measurements via Eq. (4.21) (see text) and the corresponding background value of a_{CsCs}. The red circles show the result from a hyperspherical calculation with Lennard-Jones potentials at $a_{\mathrm{CsCs}} = -1500\ a_0$ and $a_{\mathrm{CsCs}} = 200\ a_0$ [Wang and Greene, 2015]. The red-dashed line shows the Cs_2 + Li dissociation threshold, obtained from case (ii). The labels n in the left panel denotes the indexing that is used for the Efimov trimer states.

$a_{\mathrm{CsCs}} \approx -1500\ a_0$. As discussed previously, this energy shift is a consequence of the Cs-Cs vdW interaction.

Direct observation of this shift would require the ability to produce and measure trimer binding energies as a function of the interspecies scattering length, similar to the rf-association experiments in three-body Li systems [Lompe et al., 2010b; Nakajima et al., 2011; Machtey et al., 2012b]. Such capabilities at the present stage of our experiment are not available. However, we may use the analogy with the universal zero-range theory for homonuclear systems, in which the trimer energy spectrum is described by a universal function of the scattering length [Braaten and Hammer, 2006]. The position of the Efimov resonance $a_-^{(n)}$ is connected to the binding energy E_n^∞ at the scattering pole by a universal constant $\gamma \approx 1.56$ according to the expression $E_n^\infty = -\gamma^2\hbar^2/\left(2m\left(a_-^{(n)}\right)^2\right)$ [Braaten and Hammer, 2006]. Hence, we may estimate the approximate binding energies of the bound heteronuclear $LiCs_2$ trimers from the analogous relation [Wang, 2015]

$$E_n^\infty = -\frac{1}{2\mu_3}\left(\frac{\hbar\gamma^{(n)}}{a_-^{(n)}}\right)^2, \tag{4.21}$$

where $\gamma^{(n)}$ is a constant for the particular atomic three-body system and $a_-^{(n)}$ denotes the positions of the heteronuclear Efimov resonances. This yields $\gamma_- = 1.88$ and $\gamma_+ = 3.08$ from a weighted fit of in Sect. 4.3.1 and 4.3.2 observed Efimov resonance progressions, where the subscript indicates positive or negative a_{CsCs}, as appropriate for each of the series. Even with this very crude approach the obtained binding energies are reasonably well reproduced by the trimer energy spectrum, as shown in Fig. 4.9. The change in the Efimov scaling factor along the progression of the trimer states is also recaptured.

This approach is only strictly valid in the limit where a_{LiCs} is the only relevant length scale in the system. However, the influence of the previously discussed non-adiabatic couplings to other hyperspherical channels and additional short-range effects can be tested with the LJ model calculations [Wang and Greene, 2015]. For example, the neglected Li-Cs interaction potential may lead to non-universal modifications to the functional dependence of the heteronuclear trimer energy spectrum, and consequently invalidation of Eq. (4.21). Therefore, similar to the simplified BO approach, we extract the constant γ from the three-body energy spectra that are shown in Fig. 4.6. This yields coefficients $\gamma_-^{(0)} = 2.27$, $\gamma_-^{(1)} = 2.94$, $\gamma_+^{(1)} = 3.28$, and $\gamma_+^{(2)} = 2.65$, which are in reasonable agreement with the simplified BO model.

Chapter 5

Conclusion and outlook

In this thesis we studied the heteronuclear Efimov scenario in ultracold Bose-Fermi mixtures of ^{133}Cs and ^{6}Li atoms. Therefore, the binary Li-Cs scattering properties were established by radio-frequency spectroscopy of weakly-bound molecular states and additional atom-loss spectroscopy. They were used to investigate the three-body Efimov resonances in the $LiCs_2$ system, where we found both, remarkably universal behaviour and departures from it. We demonstrated that the observed deviations can originate as a direct consequence of the pairwise interatomic potentials, and proposed that a crossover between the long-range Efimov and the short-range van der Waals physics dominated regimes can be realized.

A major part of the experimental apparatus that was used for addressing these questions was constructed during this thesis. With it separate Bose-Einstein condensation of Cs atoms and Li_2 molecules was achieved. One of the highlights of the setup is the bichromatic dipole trap that was employed to minimize the gravitational sag and maximize the overlap between the ultracold clouds of Li and Cs atoms. It allowed to mix these gases at yet unprecedented temperatures that were a factor of three lower than any result reported for this mixture so far. With this concept production of double-quantum-degenerate Bose-Fermi mixtures will be feasible.

The first experiments focused on a precise determination and characterization of Li-Cs collisional and, especially, Feshbach resonance properties in the two energetically lowest scattering channels. We refined the previous atom-loss measurements [Repp et al., 2013; Tung et al., 2013; Pires et al., 2014a] and improved the knowledge of the interspecies scattering length parametrization by almost an order of magnitude. It was achieved by atom-loss spectroscopy of narrow Feshbach resonances and radio-frequency association of colliding Li-Cs atom pairs into weakly-bound dimers close to the broad Feshbach resonances. In this way we were able to probe the long-range part of the molecular potential, which in combination with the earlier measurements from Fourier-transform spectroscopy [Staanum et al., 2007] delivered improved singlet and triplet potential curves of the LiCs electronic ground state

from a coupled-channels calculation. The potentials were used to map the Li-Cs scattering length on the external magnetic field, which illustrated that, in contrast to assumptions from Tung et al. [2014], for the broad Li-Cs Feshbach resonances the pole position is shifted with respect to the atom-loss maximum. The newly acquired parametrization was critical for the following investigation and appropriate analysis of the Efimov physics with $LiCs_2$ trimers. Its applications extend well beyond the studies of universal few-body physics, where it can serve as a starting point for controlled preparation and control of ultracold polar molecules [Carr et al., 2009; Dulieu and Gabbanini, 2009; Jin and Ye, 2012] and strongly interacting mixtures and polarons [Koschorreck et al., 2012; Ferrier-Barbut et al., 2014; Schirotzek et al., 2009].

Then we turned our attention to the heteronuclear Efimov scenario close to a broad Li-Cs Feshbach resonance that was characterized with a large and negative Cs-Cs background scattering length. By tuning the Li-Cs scattering length via the external magnetic field we observed a series of three consecutive Efimov resonances, for the first time in any system studied so far. Following atom-loss and three-body recombination rate measurements delivered a consistent picture about the resonance positions. We extracted a scaling factor of 5.0(1.5) between the second and third Efimov feature, confirming the predictions of 4.9 from the universal theory for the particular mass ratio of Li and Cs atoms. The obtained scaling factor of 5.5(2) between the first two Efimov resonance positions, however, slightly deviated from the universal law and interpretation from Ref. [Tung et al., 2014]. Therefore, we analyzed the recombination spectra with a zero-range theory for heteronuclear mixtures at finite temperatures [Petrov and Werner, 2015], which appropriately treated the varying Cs-Cs background scattering length and thermal averaging. The model demonstrated excellent agreement with the two excited state Efimov resonances. Nevertheless, the position of the ground state resonance still deviated from the theoretically predicted universal scaling progression. Since this trimer resonance was found at a Li-Cs scattering length that is only a factor of 7 or 3 larger than the Li-Cs or Cs-Cs van der Waals ranges, respectively, we speculated that this departure may originate from the individual details of the pairwise interaction potentials.

This discrepancy was resolved by demonstrating that the use of more realistic pairwise model potentials recovers the essential features of the experimentally measured three-body recombination spectra. We compared the observations with a finite-temperature model that was based on Lennard-Jones potentials [Wang et al., 2012d; Wang and Greene, 2015] and found good agreement with the increased scaling. This approach was tested close to another broad Feshbach resonance with a different and positive Cs-Cs background scattering length. Analogous to the previous case, we found a series of two consecutive Efimov resonances. These measurements provided the first experimental test of the influence of the intraparticle scattering

length on the heteronuclear Efimov scenario. The obtained scaling factor of 3.9(5) was in good agreement with the theoretical predictions of 4.3 from the Lennard-Jones model, however the resonance positions were slightly shifted. The exact mechanism behind this is still an open question. One of possible solutions might be a two-channel formalism, which has been used for the description of three-body scattering observables near narrow Feshbach resonances in homonuclear systems [Mehta et al., 2008; Wang et al., 2011a; Wang and Esry, 2011; Sørensen et al., 2013; Wang and Julienne, 2014; Wang et al., 2014]. Therefore, an extension of the presently employed single-channel picture by a second channel also for heteronuclear systems is an important challenge for the theory. Equivalent plea can be made to the universal zero-range models [Helfrich et al., 2010; Rem et al., 2013; Petrov and Werner, 2015; Mikkelsen et al., 2015], where no current description of heteronuclear three-body recombination rates for finite and positive intraspecies scattering length is available.

We discovered that the short-range and long-range regimes, which are dominated by the pairwise van der Waals and three-body Efimov physics, respectively, in the Born-Oppenheimer picture are connected with a continuous transition, during which the nature of a three-body state gradually transforms between the two regimes. Experimental investigation of this crossover would yield deep insights of the intrinsic mechanisms that are governing the link between the two- and three-body physics. It could be realized in a situation where both, the respective intra- and interspecies scattering lengths between B-B and B-X atom pairs of a BBX system, are independently tuned from large negative to large positive values. Potentially, such situation could be experimentally implemented by the simultaneous use of two different kinds of Feshbach resonances, for example, the magnetic ones, as done in our experiments, and optically- [Bohn and Julienne, 1997, 1999; Borkowski et al., 2009] or rf-field- [Kaufman et al., 2009; Tscherbul et al., 2010; Hanna et al., 2010; Xie et al., 2012] induced ones.

Finally, we found indications of a possible $LiCs_3$ tetramer recombination resonance. Although we could not verify the exact constituents of the recombination process, the position of the resonance feature was consistent with the theoretical predictions from Blume and Yan [2014]. Unambiguous demonstration will require significant improvements of our experimental imaging system, which due to the low signal-to-noise ratio is presently limiting the minimum number of atoms that can be detected by it. Furthermore, the confirmation of the four-body universality, where the energies of the tetramer states are completely determined by the three-body state [Hammer and Platter, 2007; D'Incao et al., 2009b; von Stecher et al., 2009; Blume and Yan, 2014], requires observation of at least two tetramer features that are separated by a trimer resonance. Experiments with homonuclear species are already heading in this direction [Ferlaino et al., 2008, 2009; Zenesini et al., 2013; Pollack et al., 2009; Dyke et al., 2013]. In this work we could make the first, still very hum-

ble step with a mixed-species system. Without doubt, further studies of universal tetramers and N-body clusters in heteronuclear systems are highly promising.

Additional to the investigation of universal few-body aggregates two more research avenues seem highly promising and experimentally feasible already with the present technology. The heteronuclear Efimov scenario at positive interspecies scattering lengths is one of them. The weakly-bound halo dimer state has the potential to substantially modify the behavior of low-energy three-body scattering observables. It manifests as either recombination maxima or interference minima at the atom-dimer and three-atom dissociation thresholds [Nielsen and Macek, 1999; Esry et al., 1999; Bedaque et al., 2000; Braaten and Hammer, 2001]. While these signatures of Efimov physics have often been used in experiments with homonuclear atoms to study the link between the trimer state at positive and negative scattering lengths, there is only little known about their behavior in mixed-species systems. Only the KRb combination has been investigated so far [Barontini et al., 2009, 2010; Bloom et al., 2013]. Thus, tests of universal few-body physics with $LiCs_2$ trimers and positive a_{LiCs} are very desirable.

Studies of three-body energy spectra via radio-frequency association has the capability to establish a new paradigm for few-body physics with ultracold atoms [Lompe et al., 2010b; Nakajima et al., 2011; Machtey et al., 2012b; Tscherbul and Rittenhouse, 2011]. Its various implementations result in the creation of Efimov trimers out of colliding atom-dimer pairs or three free atoms at the scattering threshold. In this way, instead of probing Efimov level crossings that are guised as recombination resonances, direct information about the trimer energies at the given pairwise scattering length can be accessed. This is especially interesting in cases where deviations from the universality are expected, or have already been observed in the recombination spectra. By probing the binding energies detailed information about the short-range effects and the influence of the internal atomic structure on the few-body system can be elucidated. Having found these effects in the $LiCs_2$ Efimov scenario, their direct exploration via radio-frequency spectroscopy of $LiCs_2$ trimers is a natural next step. These are just a few of the possibilities, as this approach can potentially reveal a much broader spectra of exciting few-body phenomena.

All of these developments will benefit from a further reduction of the sample temperature. The least-bound trimer features were found in the unitarity-limited regime, dominated by the thermal energy and not the one of mutual interaction. Therefore, even lower relative collision energies will pave the way for the demonstration of three consecutive resonances in the universality-governed regime, and enable access to strongly correlated many-body systems with large mass imbalance. Undoubtedly, this will open the doors for a new and exiting era for the investigation of few- and many-body phenomena and expand our understanding of these systems and their properties in heteronuclear quantum mixtures.

Bibliography

Acharya, B., Ji, C., and Phillips, D. (2013). Implications of a matter-radius measurement for the structure of carbon-22. *Physics Letters B*, 723(1–3):196–200.

Aikawa, K., Frisch, A., Mark, M., Baier, S., Grimm, R., and Ferlaino, F. (2014). Reaching Fermi degeneracy via universal dipolar scattering. *Phys. Rev. Lett.*, 112:010404.

Aikawa, K., Frisch, A., Mark, M., Baier, S., Rietzler, A., Grimm, R., and Ferlaino, F. (2012). Bose-Einstein condensation of Erbium. *Phys. Rev. Lett.*, 108:210401.

Amado, R. D. and Noble, J. V. (1972). Efimov's effect: A new pathology of three-particle systems. II. *Phys. Rev. D*, 5:1992–2002.

Arias, A. (2014). A reservoir optical dipole trap for creating a Bose-Einstein condensate of ^{133}Cs. Master's thesis, Ruperto-Carola-University of Heidelberg.

Atkins, P. W. and Friedman, R. S. (2000). *Molecular Quantum Mechanics*. Oxford University Press.

Barontini, G., Weber, C., Rabatti, F., Catani, J., Thalhammer, G., Inguscio, M., and Minardi, F. (2009). Observation of heteronuclear atomic Efimov resonances. *Phys. Rev. Lett.*, 103:043201.

Barontini, G., Weber, C., Rabatti, F., Catani, J., Thalhammer, G., Inguscio, M., and Minardi, F. (2010). Erratum: Observation of heteronuclear atomic Efimov resonances [Phys. Rev. Lett. 103, 043201 (2009)]. *Phys. Rev. Lett.*, 104:059901.

Bartenstein, M., Altmeyer, A., Riedl, S., Geursen, R., Jochim, S., Chin, C., Denschlag, J. H., Grimm, R., Simoni, A., Tiesinga, E., Williams, C. J., and Julienne, P. S. (2005). Precise determination of ^{6}Li cold collision parameters by radio-frequency spectroscopy on weakly bound molecules. *Phys. Rev. Lett.*, 94:103201.

Bedaque, P. F., Braaten, E., and Hammer, H.-W. (2000). Three-body recombination in Bose gases with large scattering length. *Phys. Rev. Lett.*, 85:908–911.

Bedaque, P. F. and van Kolck, U. (2002). Effective field theory for few-nucleon systems. *Annual Review of Nuclear and Particle Science*, 52(1):339–396.

Bellotti, F. F., Frederico, T., Yamashita, M. T., Fedorov, D. V., Jensen, A. S., and Zinner, N. T. (2013). Mass-imbalanced three-body systems in two dimensions. *Journal of Physics B: Atomic, Molecular and Optical Physics*, 46(5):055301.

Bendkowsky, V., Butscher, B., Nipper, J., Balewski, J. B., Shaffer, J. P., Löw, R., Pfau, T., Li, W., Stanojevic, J., Pohl, T., and Rost, J. M. (2010). Rydberg trimers and excited dimers bound by internal quantum reflection. *Phys. Rev. Lett.*, 105:163201.

Berninger, M., Zenesini, A., Huang, B., Harm, W., Nägerl, H.-C., Ferlaino, F., Grimm, R., Julienne, P. S., and Hutson, J. M. (2011). Universality of the three-body parameter for Efimov states in ultracold cesium. *Phys. Rev. Lett.*, 107:120401.

Berninger, M., Zenesini, A., Huang, B., Harm, W., Nägerl, H.-C., Ferlaino, F., Grimm, R., Julienne, P. S., and Hutson, J. M. (2013). Feshbach resonances, weakly bound molecular states, and coupled-channel potentials for cesium at high magnetic fields. *Phys. Rev. A*, 87:032517.

Bertelsen, J. F. and Mølmer, K. (2007). Association of heteronuclear molecules in a harmonic oscillator well. *Phys. Rev. A*, 76:043615.

Bhaduri, R. K., Chatterjee, A., and van Zyl, B. P. (2011). An elementary exposition of the Efimov effect. *American Journal of Physics*, 79(3):274–281.

Bloch, I., Dalibard, J., and Zwerger, W. (2008). Many-body physics with ultracold gases. *Rev. Mod. Phys.*, 80:885–964.

Bloom, R. S., Hu, M.-G., Cumby, T. D., and Jin, D. S. (2013). Tests of universal three-body physics in an ultracold Bose-Fermi mixture. *Phys. Rev. Lett.*, 111:105301.

Blume, D. (2012). Universal four-body states in heavy-light mixtures with a positive scattering length. *Phys. Rev. Lett.*, 109:230404.

Blume, D. and Greene, C. H. (2000). Monte Carlo hyperspherical description of helium cluster excited states. *The Journal of Chemical Physics*, 112(18):8053–8067.

Blume, D., Greene, C. H., and Esry, B. D. (2000). Comparative study of He_3, Ne_3, and Ar_3 using hyperspherical coordinates. *The Journal of Chemical Physics*, 113(6):2145–2158.

Blume, D., Greene, C. H., and Esry, B. D. (2014). Erratum: "comparative study of He_3, Ne_3, and Ar_3 using hyperspherical coordinates" [J. Chem. Phys.113, 2145 (2000)]. *The Journal of Chemical Physics*, 141(6).

Blume, D. and Yan, Y. (2014). Generalized Efimov scenario for heavy-light mixtures. *Phys. Rev. Lett.*, 113:213201.

Bohn, J. L. and Julienne, P. S. (1997). Prospects for influencing scattering lengths with far-off-resonant light. *Phys. Rev. A*, 56:1486–1491.

Bohn, J. L. and Julienne, P. S. (1999). Semianalytic theory of laser-assisted resonant cold collisions. *Phys. Rev. A*, 60:414–425.

Borkowski, M., Ciuryło, R., Julienne, P. S., Tojo, S., Enomoto, K., and Takahashi, Y. (2009). Line shapes of optical Feshbach resonances near the intercombination transition of bosonic ytterbium. *Phys. Rev. A*, 80:012715.

Bourdel, T., Cubizolles, J., Khaykovich, L., Magalhães, K. M. F., Kokkelmans, S. J. J. M. F., Shlyapnikov, G. V., and Salomon, C. (2003). Measurement of the interaction energy near a Feshbach resonance in a ^{6}Li Fermi gas. *Phys. Rev. Lett.*, 91:020402.

Braaten, E. and Hammer, H.-W. (2001). Three-body recombination into deep bound states in a Bose gas with large scattering length. *Phys. Rev. Lett.*, 87:160407.

Braaten, E. and Hammer, H.-W. (2006). Universality in few-body systems with large scattering length. *Physics Reports*, 428(5–6):259–390.

Braaten, E. and Hammer, H.-W. (2007). Efimov physics in cold atoms. *Annals of Physics*, 322(1):120–163.

Braaten, E., Hammer, H.-W., Kang, D., and Platter, L. (2008). Three-body recombination of identical bosons with a large positive scattering length at nonzero temperature. *Phys. Rev. A*, 78:043605.

Bruch, L. W., Schöllkopf, W., and Toennies, J. P. (2002). The formation of dimers and trimers in free jet ^{4}He cryogenic expansions. *The Journal of Chemical Physics*, 117(4):1544–1566.

Brühl, R., Kalinin, A., Kornilov, O., Toennies, J. P., Hegerfeldt, G. C., and Stoll, M. (2005). Matter wave diffraction from an inclined transmission grating: Searching for the elusive ^{4}He trimer efimov state. *Phys. Rev. Lett.*, 95:063002.

Busch, T., Englert, B.-G., Rzażewski, K., and Wilkens, M. (1998). Two cold atoms in a harmonic trap. *Foundations of Physics*, 28(4):549–559.

Camblong, H. E., Epele, L. N., Fanchiotti, H., and García Canal, C. A. (2001). Quantum anomaly in molecular physics. *Phys. Rev. Lett.*, 87:220402.

Carlson, J. and Schiavilla, R. (1998). Structure and dynamics of few-nucleon systems. *Rev. Mod. Phys.*, 70:743–841.

Carr, L. D., DeMille, D., Krems, R. V., and Ye, J. (2009). Cold and ultracold molecules: science, technology and applications. *New Journal of Physics*, 11(5):055049.

Catani, J., Barontini, G., Lamporesi, G., Rabatti, F., Thalhammer, G., Minardi, F., Stringari, S., and Inguscio, M. (2009). Entropy exchange in a mixture of ultracold atoms. *Phys. Rev. Lett.*, 103:140401.

Cencek, W., Przybytek, M., Komasa, J., Mehl, J. B., Jeziorski, B., and Szalewicz, K. (2012). Effects of adiabatic, relativistic, and quantum electrodynamics interactions on the pair potential and thermophysical properties of helium. *The Journal of Chemical Physics*, 136(22):224303.

Chin, C. (2011). Universal scaling of Efimov resonance positions in cold atom systems. *arXiv:1111.1484*.

Chin, C., Grimm, R., Julienne, P., and Tiesinga, E. (2010). Feshbach resonances in ultracold gases. *Rev. Mod. Phys.*, 82:1225–1286.

Chin, C. and Julienne, P. S. (2005). Radio-frequency transitions on weakly bound ultracold molecules. *Phys. Rev. A*, 71:012713.

Chu, S. (1998). Nobel lecture: The manipulation of neutral particles. *Rev. Mod. Phys.*, 70:685–706.

Cohen-Tannoudji, C. N. (1998). Nobel lecture: Manipulating atoms with photons. *Rev. Mod. Phys.*, 70:707–719.

Coon, S. A. and Holstein, B. R. (2002). Anomalies in quantum mechanics: The $1/r^2$ potential. *American Journal of Physics*, 70(5):513–519.

Cornell, E. A. and Wieman, C. E. (2002). Nobel lecture: Bose-Einstein condensation in a dilute gas, the first 70 years and some recent experiments. *Rev. Mod. Phys.*, 74:875–893.

Crawford, O. H. (1967). Bound states of a charged particle in a dipole field. *Proceedings of the Physical Society*, 91(2):279.

Dalfovo, F., Giorgini, S., Pitaevskii, L. P., and Stringari, S. (1999). Theory of Bose-Einstein condensation in trapped gases. *Rev. Mod. Phys.*, 71:463–512.

Dalibard, J. (1999). Collisional dynamics of ultra-cold atomic gases. In Inguscio, M., Stringari, S., and Wieman, C. E., editors, *Proceedings of the International School of Physics Enrico Fermi*, volume Course CXL, page 321. IOS Press, Amsterdam.

Deiglmayr, J., Grochola, A., Repp, M., Mörtlbauer, K., Glück, C., Lange, J., Dulieu, O., Wester, R., and Weidemüller, M. (2008). Formation of ultracold polar molecules in the rovibrational ground state. *Phys. Rev. Lett.*, 101:133004.

Delves, L. (1960). Tertiary and general-order collisions (ii). *Nuclear Physics*, 20(0):275 – 308.

Derevianko, A., Babb, J. F., and Dalgarno, A. (2001). High-precision calculations of van der Waals coefficients for heteronuclear alkali-metal dimers. *Phys. Rev. A*, 63:052704.

Desfrançois, C., Abdoul-Carime, H., and Schermann, J. P. (1996). Ground-state dipole bound anions. *International Journal of Modern Physics B*, 10(12):1339–1395.

Deuretzbacher, F., Becker, D., Bjerlin, J., Reimann, S. M., and Santos, L. (2014). Quantum magnetism without lattices in strongly interacting one-dimensional spinor gases. *Phys. Rev. A*, 90:013611.

Deuretzbacher, F., Plassmeier, K., Pfannkuche, D., Werner, F., Ospelkaus, C., Ospelkaus, S., Sengstock, K., and Bongs, K. (2008). Heteronuclear molecules in an optical lattice: Theory and experiment. *Phys. Rev. A*, 77:032726.

Dieckmann, K., Stan, C. A., Gupta, S., Hadzibabic, Z., Schunck, C. H., and Ketterle, W. (2002). Decay of an ultracold fermionic lithium gas near a Feshbach resonance. *Phys. Rev. Lett.*, 89:203201.

D'Incao, J. P. and Esry, B. D. (2005). Scattering length scaling laws for ultracold three-body collisions. *Phys. Rev. Lett.*, 94:213201.

D'Incao, J. P. and Esry, B. D. (2006). Enhancing the observability of the Efimov effect in ultracold atomic gas mixtures. *Phys. Rev. A*, 73:030703.

D'Incao, J. P. and Esry, B. D. (2009). Ultracold three-body collisions near overlapping Feshbach resonances. *Phys. Rev. Lett.*, 103:083202.

D'Incao, J. P. and Greene, C. (2014). Private communication.

D'Incao, J. P., Greene, C. H., and Esry, B. D. (2009a). The short-range three-body phase and other issues impacting the observation of Efimov physics in ultracold quantum gases. *Journal of Physics B: Atomic, Molecular and Optical Physics*, 42(4):044016.

D'Incao, J. P., von Stecher, J., and Greene, C. H. (2009b). Universal four-boson states in ultracold molecular gases: Resonant effects in dimer-dimer collisions. *Phys. Rev. Lett.*, 103:033004.

Domcke, W. and Cederbaum, L. S. (1981). On the interpretation of low-energy electron-HCl scattering phenomena. *Journal of Physics B: Atomic and Molecular Physics*, 14(1):149.

Dulieu, O. and Gabbanini, C. (2009). The formation and interactions of cold and ultracold molecules: new challenges for interdisciplinary physics. *Reports on Progress in Physics*, 72(8):086401.

Dyke, P., Pollack, S. E., and Hulet, R. G. (2013). Finite-range corrections near a Feshbach resonance and their role in the Efimov effect. *Phys. Rev. A*, 88:023625.

Efimov, V. (1970). Energy levels arising from resonant two-body forces in a three-body system. *Physics Letters B*, 33(8):563–564.

Efimov, V. (1971). Weakly bound states of three resonantly-interacting particles. *Sov. J. Nuc. Phys.*, 12:589.

Efimov, V. (1973). Energy levels of three resonantly interacting particles. *Nuclear Physics A*, 210(1):157–188.

Efimov, V. (1979). Low-energy properties of three resonantly interacting particles. *Sov. J. Nuc. Phys.*, 29:546.

Efremov, M. A., Plimak, L., Berg, B., Ivanov, M. Y., and Schleich, W. P. (2009). Efimov states in atom-molecule collisions. *Phys. Rev. A*, 80:022714.

Efron, B. and Tibshirani, R. (1993). *An Introduction to the Bootstrap*. Chapman and Hall/CRC.

Esry, B. D. and D'Incao, J. P. (2007). Efimov physics in ultracold three-body collisions. *Journal of Physics: Conference Series*, 88(1):012040.

Esry, B. D., Greene, C. H., and Burke, J. P. (1999). Recombination of three atoms in the ultracold limit. *Phys. Rev. Lett.*, 83:1751–1754.

Esry, B. D., Lin, C. D., and Greene, C. H. (1996). Adiabatic hyperspherical study of the Helium trimer. *Phys. Rev. A*, 54:394–401.

Essin, A. M. and Griffiths, D. J. (2006). Quantum mechanics of the $1/x^2$ potential. *American Journal of Physics*, 74(2):109–117.

Fano, U. (1961). Effects of configuration interaction on intensities and phase shifts. *Phys. Rev.*, 124:1866–1878.

Fedichev, P. O., Reynolds, M. W., and Shlyapnikov, G. V. (1996). Three-body recombination of ultracold atoms to a weakly bound s level. *Phys. Rev. Lett.*, 77:2921–2924.

Fedorov, D. V. and Jensen, A. S. (1993). Efimov effect in coordinate space Faddeev equations. *Phys. Rev. Lett.*, 71:4103–4106.

Fedorov, D. V., Jensen, A. S., and Riisager, K. (1994). Efimov states in halo nuclei. *Phys. Rev. Lett.*, 73:2817–2820.

Ferlaino, F., Knoop, S., Berninger, M., Harm, W., D'Incao, J. P., Nägerl, H.-C., and Grimm, R. (2009). Evidence for universal four-body states tied to an Efimov trimer. *Phys. Rev. Lett.*, 102:140401.

Ferlaino, F., Knoop, S., Mark, M., Berninger, M., Schöbel, H., Nägerl, H.-C., and Grimm, R. (2008). Collisions between tunable halo dimers: Exploring an elementary four-body process with identical bosons. *Phys. Rev. Lett.*, 101:023201.

Ferlaino, F., Zenesini, A., Berninger, M., Huang, B., Nägerl, H.-C., and Grimm, R. (2011). Efimov resonances in ultracold quantum gases. *Few-Body Systems*, 51:113–133.

Ferrier-Barbut, I., Delehaye, M., Laurent, S., Grier, A. T., Pierce, M., Rem, B. S., Chevy, F., and Salomon, C. (2014). A mixture of Bose and Fermi superfluids. *Science*, 345(6200):1035.

Feshbach, H. (1958). Unified theory of nuclear reactions. *Annals of Physics*, 5(4):357–390.

Feshbach, H. (1962). A unified theory of nuclear reactions. II. *Annals of Physics*, 19(2):287–313.

Fisher, M. E. (1998). Renormalization group theory: Its basis and formulation in statistical physics. *Rev. Mod. Phys.*, 70:653–681.

Flambaum, V. V., Gribakin, G. F., and Harabati, C. (1999). Analytical calculation of cold-atom scattering. *Phys. Rev. A*, 59:1998–2005.

Fleming, D. G., Manz, J., Sato, K., and Takayanagi, T. (2014). Fundamental change in the nature of chemical bonding by isotopic substitution. *Angew. Chem. Int. Ed.*, 53(50):13706–13709.

Fonseca, A. C., Redish, E. F., and Shanley, P. (1979). Efimov effect in an analytically solvable model. *Nuclear Physics A*, 320(2):273 – 288.

Frederico, T., Delfino, A., Hadizadeh, M., Tomio, L., and Yamashita, M. (2013). Universality in four-boson systems. *Few-Body Systems*, 54(5-6):559–568.

Frederico, T., Delfino, A., Tomio, L., and Yamashita, M. (2012). Universal aspects of light halo nuclei. *Progress in Particle and Nuclear Physics*, 67(4):939–994.

Fuchs, J., Ticknor, C., Dyke, P., Veeravalli, G., Kuhnle, E., Rowlands, W., Hannaford, P., and Vale, C. J. (2008). Binding energies of ^{6}Li p-wave Feshbach molecules. *Phys. Rev. A*, 77:053616.

Gao, B. (1998). Solutions of the Schrödinger equation for an attractive $1/r^6$ potential. *Phys. Rev. A*, 58:1728–1734.

Gao, B. (2000). Zero-energy bound or quasibound states and their implications for diatomic systems with an asymptotic van der Waals interaction. *Phys. Rev. A*, 62:050702.

Gao, B. (2001). Angular-momentum-insensitive quantum-defect theory for diatomic systems. *Phys. Rev. A*, 64:010701.

Gao, B. (2003). Effective potentials for atom–atom interactions at low temperatures. *Journal of Physics B: Atomic, Molecular and Optical Physics*, 36(10):2111.

Gattobigio, M. and Kievsky, A. (2014). Universality and scaling in the n-body sector of Efimov physics. *Phys. Rev. A*, 90:012502.

Giannozzi, P. (2014). Numerical methods in quantum mechanics. *Lecture notes*.

Giorgini, S., Pitaevskii, L. P., and Stringari, S. (2008). Theory of ultracold atomic Fermi gases. *Rev. Mod. Phys.*, 80:1215–1274.

Giovanazzi, S., Görlitz, A., and Pfau, T. (2002). Tuning the dipolar interaction in quantum gases. *Phys. Rev. Lett.*, 89:130401.

Giri, P. R., Gupta, K. S., Meljanac, S., and Samsarov, A. (2008). Electron capture and scaling anomaly in polar molecules. *Physics Letters A*, 372(17):2967–2970.

Góral, K., Kähler, T., Gardiner, S. A., Tiesinga, E., and Julienne, P. S. (2004). Adiabatic association of ultracold molecules via magnetic-field tunable interactions. *Journal of Physics B: Atomic, Molecular and Optical Physics*, 37(17):3457.

Greene, C. H. (2010). Universal insights from few-body land. *Physics Today*, 63(3):40–45.

Gribakin, G. F. and Flambaum, V. V. (1993). Calculation of the scattering length in atomic collisions using the semiclassical approximation. *Phys. Rev. A*, 48:546–553.

Gribakin, G. F., Young, J. A., and Surko, C. M. (2010). Positron-molecule interactions: Resonant attachment, annihilation, and bound states. *Rev. Mod. Phys.*, 82:2557–2607.

Grimm, R., Weidemüller, M., and Ovchinnikov, Y. B. (2000). Optical dipole traps for neutral atoms. volume 42 of *Advances In Atomic, Molecular, and Optical Physics*, pages 95 – 170. Academic Press.

Gross, N., Shotan, Z., Kokkelmans, S., and Khaykovich, L. (2009). Observation of universality in ultracold ^{7}Li three-body recombination. *Phys. Rev. Lett.*, 103:163202.

Gross, N., Shotan, Z., Kokkelmans, S., and Khaykovich, L. (2010). Nuclear-spin-independent short-range three-body physics in ultracold atoms. *Phys. Rev. Lett.*, 105:103203.

Gross, N., Shotan, Z., Machtey, O., Kokkelmans, S., and Khaykovich, L. (2011). Study of Efimov physics in two nuclear-spin sublevels of ^{7}Li. *Comptes Rendus Physique*, 12:4 – 12.

Hadizadeh, M. R., Yamashita, M. T., Tomio, L., Delfino, A., and Frederico, T. (2011). Scaling properties of universal tetramers. *Phys. Rev. Lett.*, 107:135304.

Hadizadeh, M. R., Yamashita, M. T., Tomio, L., Delfino, A., and Frederico, T. (2012). Binding and structure of tetramers in the scaling limit. *Phys. Rev. A*, 85:023610.

Hagen, G., Hagen, P., Hammer, H.-W., and Platter, L. (2013). Efimov physics around the neutron-rich ^{60}Ca isotope. *Phys. Rev. Lett.*, 111:132501.

Hammer, H.-W., Nogga, A., and Schwenk, A. (2013). *Colloquium* : Three-body forces: From cold atoms to nuclei. *Rev. Mod. Phys.*, 85:197–217.

Hammer, H.-W. and Platter, L. (2007). Universal properties of the four-body system with large scattering length. *The European Physical Journal A*, 32(1):113–120.

Hammer, H.-W. and Platter, L. (2010). Efimov states in nuclear and particle physics. *Annu. Rev. Nucl. Part. Sci.*, 60:207.

Hammer, H.-W. and Platter, L. (2011). Efimov physics from a renormalization group perspective. *Philosophical Transactions of the Royal Society A: Mathematical,Physical and Engineering Sciences*, 369(1946):2679–2700.

Hammes, M., Rychtarik, D., Nägerl, H.-C., and Grimm, R. (2002). Cold-atom gas at very high densities in an optical surface microtrap. *Phys. Rev. A*, 66:051401.

Han, J. (2010). Direct evidence of three-body interactions in a cold ^{85}Rb Rydberg gas. *Phys. Rev. A*, 82:052501.

Hanna, T. M., Tiesinga, E., and Julienne, P. S. (2010). Creation and manipulation of Feshbach resonances with radiofrequency radiation. *New Journal of Physics*, 12(8):083031.

Hansen, P. G., Jensen, A. S., and Jonson, B. (1995). Nuclear halos. *Annual Review of Nuclear and Particle Science*, 45(1):591–634.

Heck, R. (2012). All-optical formation of an ultracold gas of fermionic lithium close to quantum degeneracy. Master's thesis, Ruperto-Carola-University of Heidelberg.

Hegerfeldt, G. C. and Köhler, T. (2000). How to study the elusive Efimov state of the $^4He_3$ molecule through a new atom-optical state-selection technique. *Phys. Rev. Lett.*, 84:3215–3219.

Helfrich, K. and Hammer, H.-W. (2010). The heteronuclear Efimov effect. *EPJ Web*.

Helfrich, K., Hammer, H.-W., and Petrov, D. S. (2010). Three-body problem in heteronuclear mixtures with resonant interspecies interaction. *Phys. Rev. A*, 81:042715.

Häfner, S. (2013). A tunable optical dipole trap for ^{6}Li and ^{133}Cs. Master's thesis, Ruperto-Carola-University of Heidelberg.

Hiyama, E. and Kamimura, M. (2012a). Linear correlations between ^{4}He trimer and tetramer energies calculated with various realistic ^{4}He potentials. *Phys. Rev. A*, 85:062505.

Hiyama, E. and Kamimura, M. (2012b). Variational calculation of ^{4}He tetramer ground and excited states using a realistic pair potential. *Phys. Rev. A*, 85:022502.

Hiyama, E. and Kamimura, M. (2014). Universality in Efimov-associated tetramers in ^{4}He. *Phys. Rev. A*, 90:052514.

Hu, M.-G., Bloom, R. S., Jin, D. S., and Goldwin, J. M. (2014). Avalanche-mechanism loss at an atom-molecule Efimov resonance. *Phys. Rev. A*, 90:013619.

Huang, B. and Grimm, R. (2014). Private communication.

Huang, B., O'Hara, K. M., Grimm, R., Hutson, J. M., and Petrov, D. S. (2014a). Three-body parameter for Efimov states in ^{6}Li. *Phys. Rev. A*, 90:043636.

Huang, B., Sidorenkov, L. A., and Grimm, R. (2015). Finite-temperature effects on a triatomic Efimov resonance in ultracold cesium. *ArXiv:1504.05360*.

Huang, B., Sidorenkov, L. A., Grimm, R., and Hutson, J. M. (2014b). Observation of the second triatomic resonance in Efimov's scenario. *Phys. Rev. Lett.*, 112:190401.

Huang, L., Wang, P., Ruzic, B. P., Fu, Z., Meng, Z., Peng, P., Bohn, J. L., and Zhang, J. (2015). Radio-frequency spectrum of the Feshbach molecular state to deeply bound molecular states in ultracold ^{40}K Fermi gases. *New Journal of Physics*, 17(3):033013.

Huckans, J. H., Williams, J. R., Hazlett, E. L., Stites, R. W., and O'Hara, K. M. (2009). Three-body recombination in a three-state Fermi gas with widely tunable interactions. *Phys. Rev. Lett.*, 102:165302.

Idziaszek, Z. and Calarco, T. (2006). Analytical solutions for the dynamics of two trapped interacting ultracold atoms. *Phys. Rev. A*, 74:022712.

Jachymski, K. and Julienne, P. S. (2013). Analytical model of overlapping Feshbach resonances. *Phys. Rev. A*, 88:052701.

Jag, M., Zaccanti, M., Cetina, M., Lous, R. S., Schreck, F., Grimm, R., Petrov, D. S., and Levinsen, J. (2014). Observation of a strong atom-dimer attraction in a mass-imbalanced Fermi-Fermi mixture. *Phys. Rev. Lett.*, 112:075302.

Jensen, A. S., Riisager, K., Fedorov, D. V., and Garrido, E. (2004). Structure and reactions of quantum halos. *Rev. Mod. Phys.*, 76:215–261.

Jin, D. S. and Ye, J. (2012). Introduction to ultracold molecules: New frontiers in quantum and chemical physics. *Chemical Reviews*, 112(9):4801–4802. PMID: 22967213.

Joachain, C. J. (1984). *Quantum Collision Theory*. Elsevier Science Ltd.

Jones, K. M., Tiesinga, E., Lett, P. D., and Julienne, P. S. (2006). Ultracold photoassociation spectroscopy: Long-range molecules and atomic scattering. *Rev. Mod. Phys.*, 78:483–535.

Jordan, K. D. and Wang, F. (2003). Theory of dipole-bound anions. *Annual Review of Physical Chemistry*, 54(1):367–396. PMID: 12626734.

Julienne, P. S. and Hutson, J. M. (2014). Contrasting the wide Feshbach resonances in ^{6}Li and ^{7}Li. *Phys. Rev. A*, 89:052715.

Kaplan, D. B. (2005). Five lectures on effective field theory. *arXiv:nucl-th/0510023*.

Kaufman, A. M., Anderson, R. P., Hanna, T. M., Tiesinga, E., Julienne, P. S., and Hall, D. S. (2009). Radio-frequency dressing of multiple Feshbach resonances. *Phys. Rev. A*, 80:050701.

Kaufman, A. M., Lester, B. J., Reynolds, C. M., Wall, M. L., Foss-Feig, M., Hazzard, K. R. A., Rey, A. M., and Regal, C. A. (2014). Two-particle quantum interference in tunnel-coupled optical tweezers. *Science*, 345(6194):306–309.

Kemper, K. W. and Cottle, P. D. (2010). Viewpoint: A breakthrough observation for neutron dripline physics. *Physics*, 3:13.

Kerman, A. J., Vuletić, V., Chin, C., and Chu, S. (2000). Beyond optical molasses: 3D Raman sideband cooling of atomic cesium to high phase-space density. *Phys. Rev. Lett.*, 84:439–442.

Ketterle, W. (2002). Nobel lecture: When atoms behave as waves: Bose-Einstein condensation and the atom laser. *Rev. Mod. Phys.*, 74:1131–1151.

Ketterle, W., Durfee, D. S., and Stamper-Kurn, D. M. (1999). Making, probing and understanding Bose-Einstein condensates. In Inguscio, M., Stringari, S., and Wieman, C., editors, *Proceedings of the International School of Physics "Enrico Fermi"*, Course CXL, pages 67–176. IOS Press, Amsterdam.

Ketterle, W. and van Druten, N. J. (1996). Evaporative cooling of trapped atoms. *Advances in Atomic, Molecular, and Optical Physics*, 37:181.

Khramov, A. Y., Hansen, A. H., Jamison, A. O., Dowd, W. H., and Gupta, S. (2012). Dynamics of Feshbach molecules in an ultracold three-component mixture. *Phys. Rev. A*, 86:032705.

Kievsky, A. and Gattobigio, M. (2013). Universal nature and finite-range corrections in elastic atom-dimer scattering below the dimer breakup threshold. *Phys. Rev. A*, 87:052719.

Klempt, C., Henninger, T., Topic, O., Scherer, M., Kattner, L., Tiemann, E., Ertmer, W., and Arlt, J. J. (2008). Radio-frequency association of heteronuclear Feshbach molecules. *Phys. Rev. A*, 78:061602.

Knoop, S., Borbely, J. S., Vassen, W., and Kokkelmans, S. J. J. M. F. (2012). Universal three-body parameter in ultracold ^{4}He*. *Phys. Rev. A*, 86:062705.

Knoop, S., Ferlaino, F., Berninger, M., Mark, M., Nägerl, H.-C., and Grimm, R. (2009a). Observation of an Efimov resonance in an ultracold mixture of atoms and weakly bound dimers. *Journal of Physics: Conference Series*, 194(1):012064.

Knoop, S., Ferlaino, F., Mark, M., Berninger, M., Schobel, H., Nägerl, H.-C., and Grimm, R. (2009b). Observation of an Efimov-like trimer resonance in ultracold atom-dimer scattering. *Nat Phys*, 5(3):227–230.

Köhler, T., Góral, K., and Julienne, P. S. (2006). Production of cold molecules via magnetically tunable Feshbach resonances. *Rev. Mod. Phys.*, 78:1311–1361.

Koschorreck, M., Pertot, D., Vogt, E., Fröhlich, B., Feld, M., and Köhl, M. (2012). Attractive and repulsive Fermi polarons in two dimensions. *Nature*, 485(7400):619–622.

Kraemer, T., Mark, M., Waldburger, P., Danzl, J. G., Chin, C., Engeser, B., Lange, A. D., Pilch, K., Jaakkola, A., Nägerl, H.-C., and Grimm, R. (2006). Evidence for Efimov quantum states in an ultracold gas of caesium atoms. *Nature*, 440(7082):315–318.

Kunitski, M., Zeller, S., Voigtsberger, J., Kalinin, A., Schmidt, L. P. H., Schöffler, M., Czasch, A., Schöllkopf, W., Grisenti, R. E., Jahnke, T., Blume, D., and Dörner, R. (2015). Observation of the Efimov state of the helium trimer. *Science*, 348(6234):551–555.

Lahaye, T., Menotti, C., Santos, L., Lewenstein, M., and Pfau, T. (2009). The physics of dipolar bosonic quantum gases. *Reports on Progress in Physics*, 72(12):126401.

Lamporesi, G., Catani, J., Barontini, G., Nishida, Y., Inguscio, M., and Minardi, F. (2010). Scattering in mixed dimensions with ultracold gases. *Phys. Rev. Lett.*, 104:153202.

Landau, L. D. and Lifshitz, E. M. (1991). *Quantum Mechanics: non-relativistic theory*. Pergamon Press.

Lange, A. D., Pilch, K., Prantner, A., Ferlaino, F., Engeser, B., Nägerl, H.-C., Grimm, R., and Chin, C. (2009). Determination of atomic scattering lengths from measurements of molecular binding energies near Feshbach resonances. *Phys. Rev. A*, 79:013622.

LeBlanc, L. J. and Thywissen, J. H. (2007). Species-specific optical lattices. *Phys. Rev. A*, 75:053612.

Lee, M. D., Köhler, T., and Julienne, P. S. (2007). Excited Thomas-Efimov levels in ultracold gases. *Phys. Rev. A*, 76:012720.

Lévy-Leblond, J.-M. (1967). Electron capture by polar molecules. *Phys. Rev.*, 153:1–4.

Lim, T. K., Duffy, S. K., and Damer, W. C. (1977). Efimov state in the ^{4}He trimer. *Phys. Rev. Lett.*, 38:341–343.

Lin, C. (1995). Hyperspherical coordinate approach to atomic and other coulombic three-body systems. *Physics Reports*, 257(1):1 – 83.

Liu, I. C. and Rost, J. M. (2006). Polyatomic molecules formed with a Rydberg atom in an ultracold environment. *The European Physical Journal D - Atomic, Molecular, Optical and Plasma Physics*, 40(1):65–71.

Liu, I. C. H., Stanojevic, J., and Rost, J. M. (2009). Ultra-long-range Rydberg trimers with a repulsive two-body interaction. *Phys. Rev. Lett.*, 102:173001.

Lompe, T., Ottenstein, T. B., Serwane, F., Viering, K., Wenz, A. N., Zürn, G., and Jochim, S. (2010a). Atom-dimer scattering in a three-component Fermi gas. *Phys. Rev. Lett.*, 105:103201.

Lompe, T., Ottenstein, T. B., Serwane, F., Wenz, A. N., Zürn, G., and Jochim, S. (2010b). Radio-frequency association of Efimov trimers. *Science*, 330(6006):940–944.

Lu, M., Burdick, N. Q., and Lev, B. L. (2012). Quantum degenerate dipolar Fermi gas. *Phys. Rev. Lett.*, 108:215301.

Lu, M., Burdick, N. Q., Youn, S. H., and Lev, B. L. (2011). Strongly dipolar Bose-Einstein condensate of dysprosium. *Phys. Rev. Lett.*, 107:190401.

Macek, J. (1968). Properties of autoionizing states of He. *Journal of Physics B: Atomic and Molecular Physics*, 1(5):831.

Macek, J. (1986). Loosely bound states of three particles. *Zeitschrift für Physik D Atoms, Molecules and Clusters*, 3(1):31–37.

Macek, J. H. (2007). Efimov states: what are they and why are they important? *Physica Scripta*, 76(2):C3.

Machtey, O., Kessler, D. A., and Khaykovich, L. (2012a). Universal dimer in a collisionally opaque medium: Experimental observables and Efimov resonances. *Phys. Rev. Lett.*, 108:130403.

Machtey, O., Shotan, Z., Gross, N., and Khaykovich, L. (2012b). Association of Efimov trimers from a three-atom continuum. *Phys. Rev. Lett.*, 108:210406.

Maier, R. A. W., Marzok, C., Zimmermann, C., and Courteille, P. W. (2010). Radio-frequency spectroscopy of ^{6}Li p-wave molecules: Towards photoemission spectroscopy of a p-wave superfluid. *Phys. Rev. A*, 81:064701.

Manz, J., Meyer, R., Pollak, E., and Römelt, J. (1982). A new possibility of chemical bonding: vibrational stabilization of IHI. *Chemical Physics Letters*, 93(2):184 – 187.

Manz, J., Meyer, R., and Römelt, J. (1983). On vibrational bonding of IHI. *Chemical Physics Letters*, 96(6):607 – 612.

Marcelis, B., Kokkelmans, S. J. J. M. F., Shlyapnikov, G. V., and Petrov, D. S. (2008). Collisional properties of weakly bound heteronuclear dimers. *Phys. Rev. A*, 77:032707.

Marzok, C., Deh, B., Zimmermann, C., Courteille, P. W., Tiemann, E., Vanne, Y. V., and Saenz, A. (2009). Feshbach resonances in an ultracold ^{7}Li and ^{87}Rb mixture. *Phys. Rev. A*, 79:012717.

Massignan, P., Zaccanti, M., and Bruun, G. M. (2014). Polarons, dressed molecules and itinerant ferromagnetism in ultracold fermi gases. *IOP Publishing Rep. Prog. Phys.*, 77(034401).

Mehta, N. P., Rittenhouse, S. T., D'Incao, J. P., and Greene, C. H. (2008). Efimov states embedded in the three-body continuum. *Phys. Rev. A*, 78:020701.

Mehta, N. P., Rittenhouse, S. T., D'Incao, J. P., von Stecher, J., and Greene, C. H. (2009). General theoretical description of n-body recombination. *Phys. Rev. Lett.*, 103:153201.

Mies, F. H. and Raoult, M. (2000). Analysis of threshold effects in ultracold atomic collisions. *Phys. Rev. A*, 62:012708.

Mikkelsen, M., Jensen, A. S., Fedorov, D. V., and Zinner, N. T. (2015). Three-body recombination of two-component cold atomic gases into deep dimers in an optical model. *ArXiv:1501.05137*.

Moerdijk, A. J., Verhaar, B. J., and Axelsson, A. (1995). Resonances in ultracold collisions of ^{6}Li, ^{7}Li, and ^{23}Na. *Phys. Rev. A*, 51:4852–4861.

Molony, P. K., Gregory, P. D., Ji, Z., Lu, B., Köppinger, M. P., Le Sueur, C. R., Blackley, C. L., Hutson, J. M., and Cornish, S. L. (2014). Creation of ultracold $^{87}Rb^{133}Cs$ molecules in the rovibrational ground state. *Phys. Rev. Lett.*, 113:255301.

Mudrich, M., Kraft, S., Singer, K., Grimm, R., Mosk, A., and Weidemüller, M. (2002). Sympathetic cooling with two atomic species in an optical trap. *Phys. Rev. Lett.*, 88:253001.

Naidon, P., Endo, S., and Ueda, M. (2014a). Microscopic origin and universality classes of the Efimov three-body parameter. *Phys. Rev. Lett.*, 112:105301.

Naidon, P., Endo, S., and Ueda, M. (2014b). Physical origin of the universal three-body parameter in atomic Efimov physics. *Phys. Rev. A*, 90:022106.

Naidon, P., Hiyama, E., and Ueda, M. (2012). Universality and the three-body parameter of ^{4}He trimers. *Phys. Rev. A*, 86:012502.

Naidon, P. and Ueda, M. (2011). The Efimov effect in lithium 6. *Comptes Rendus Physique*, 12(1):13 – 26.

Nakaichi-Maeda, S. and Lim, T. K. (1983). Zero-energy scattering and bound states in the ^{4}He trimer and tetramer. *Phys. Rev. A*, 28:692–696.

Nakajima, S., Horikoshi, M., Mukaiyama, T., Naidon, P., and Ueda, M. (2010). Nonuniversal Efimov atom-dimer resonances in a three-component mixture of ^{6}Li. *Phys. Rev. Lett.*, 105:023201.

Nakajima, S., Horikoshi, M., Mukaiyama, T., Naidon, P., and Ueda, M. (2011). Measurement of an Efimov trimer binding energy in a three-component mixture of ^{6}Li. *Phys. Rev. Lett.*, 106:143201.

Napolitano, R., Weiner, J., Williams, C. J., and Julienne, P. S. (1994). Line shapes of high resolution photoassociation spectra of optically cooled atoms. *Phys. Rev. Lett.*, 73:1352–1355.

Ni, K.-K., Ospelkaus, S., de Miranda, M. H. G., Pe'er, A., Neyenhuis, B., Zirbel, J. J., Kotochigova, S., Julienne, P. S., Jin, D. S., and Ye, J. (2008). A high phase-space-density gas of polar molecules. *Science*, 322(5899):231–235.

Nielsen, E., Fedorov, D., Jensen, A., and Garrido, E. (2001). The three-body problem with short-range interactions. *Physics Reports*, 347(5):373 – 459.

Nielsen, E., Fedorov, D. V., and Jensen, A. S. (1998). The structure of the atomic helium trimers: halos and Efimov states. *Journal of Physics B: Atomic, Molecular and Optical Physics*, 31(18):4085.

Nielsen, E. and Macek, J. H. (1999). Low-energy recombination of identical bosons by three-body collisions. *Phys. Rev. Lett.*, 83:1566–1569.

Nishida, Y., Kato, Y., and Batista, C. D. (2013). Efimov effect in quantum magnets. *Nature*.

Nishida, Y. and Tan, S. (2008). Universal Fermi gases in mixed dimensions. *Phys. Rev. Lett.*, 101:170401.

Nishida, Y. and Tan, S. (2009). Confinement-induced Efimov resonances in Fermi-Fermi mixtures. *Phys. Rev. A*, 79:060701.

Ospelkaus, C., Ospelkaus, S., Humbert, L., Ernst, P., Sengstock, K., and Bongs, K. (2006). Ultracold heteronuclear molecules in a 3D optical lattice. *Phys. Rev. Lett.*, 97:120402.

Ospelkaus, S., Pe/'er, A., Ni, K.-K., Zirbel, J. J., Neyenhuis, B., Kotochigova, S., Julienne, P. S., Ye, J., and Jin, D. S. (2008). Efficient state transfer in an ultracold dense gas of heteronuclear molecules. *Nat Phys*, 4(8):622–626.

Ottenstein, T. B., Lompe, T., Kohnen, M., Wenz, A. N., and Jochim, S. (2008). Collisional stability of a three-component degenerate Fermi gas. *Phys. Rev. Lett.*, 101:203202.

Pal, T., Sadhukhan, P., and Bhattacharjee, S. M. (2013). Renormalization group limit cycle for three-stranded DNA. *Phys. Rev. Lett.*, 110:028105.

Pal, T., Sadhukhan, P., and Bhattacharjee, S. M. (2015). Efimov-like phase of a three-stranded DNA and the renormalization-group limit cycle. *Phys. Rev. E*, 91:042105.

Papp, S. B. and Wieman, C. E. (2006). Observation of heteronuclear Feshbach molecules from a ^{85}Rb $-^{87}$ Rb gas. *Phys. Rev. Lett.*, 97:180404.

Park, J. W., Will, S. A., and Zwierlein, M. W. (2015). Ultracold dipolar gas of fermionic ^{23}Na^{40}K molecules in their absolute ground state. *ArXiv:1505.00473*. 1505.00473.

Petrov, D. (2010). *Many-Body Physics with Ultracold Gases: Lecture Notes of the Les Houches Summer School: Volume 94, July 2010*, chapter The Few-atom problem, page Chapter 3. OUP Oxford.

Petrov, D. S., Salomon, C., and Shlyapnikov, G. V. (2005). Diatomic molecules in ultracold Fermi gases—novel composite bosons. *Journal of Physics B: Atomic, Molecular and Optical Physics*, 38(9):S645.

Petrov, D. S. and Werner, F. (2015). Three-body recombination in heteronuclear mixtures at finite temperature. *ArXiv:1502.04092*.

Phillips, W. D. (1998). Nobel lecture: Laser cooling and trapping of neutral atoms. *Rev. Mod. Phys.*, 70:721–741.

Pillai, M., Goglio, J., and Walker, T. G. (2012). Matrix Numerov method for solving Schrödinger's equation. *American Journal of Physics*, 80(11):1017–1019.

Pinkse, P. W. H., Mosk, A., Weidemüller, M., Reynolds, M. W., Hijmans, T. W., and Walraven, J. T. M. (1997). Adiabatically changing the phase-space density of a trapped Bose gas. *Phys. Rev. Lett.*, 78:990–993.

Pires, R. (2014). *Efimov Resonances in an Ultracold Mixture with Extreme Mass Imbalance*. PhD thesis, Ruperto-Carola-University of Heidelberg.

Pires, R., Repp, M., Ulmanis, J., Kuhnle, E. D., Weidemüller, M., Tiecke, T. G., Greene, C. H., Ruzic, B. P., Bohn, J. L., and Tiemann, E. (2014a). Analyzing Feshbach resonances: A ^{6}Li-^{133}Cs case study. *Phys. Rev. A*, 90:012710.

Pires, R., Ulmanis, J., Häfner, S., Repp, M., Arias, A., Kuhnle, E. D., and Weidemüller, M. (2014b). Observation of Efimov resonances in a mixture with extreme mass imbalance. *Phys. Rev. Lett.*, 112:250404.

Platter, L. (2009). Low-energy universality in atomic and nuclear physics. *Few-Body Systems*, 46(3):139–171.

Platter, L., Ji, C., and Phillips, D. R. (2009). Range corrections to three-body observables near a Feshbach resonance. *Phys. Rev. A*, 79:022702.

Pollack, S. E., Dries, D., and Hulet, R. G. (2009). Universality in three- and four-body bound states of ultracold atoms. *Science*, 326(5960):1683–1685.

Porsev, S. G. and Derevianko, A. (2003). Accurate relativistic many-body calculations of van der waals coefficients C_8 and C_{10} for alkali-metal dimers. *The Journal of Chemical Physics*, 119(2):844–850.

Porsev, S. G., Safronova, M. S., Derevianko, A., and Clark, C. W. (2014). Relativistic many-body calculations of van der Waals coefficients for Yb-Li and Yb-Rb dimers. *Phys. Rev. A*, 89:022703.

Quéméner, G. and Julienne, P. S. (2012). Ultracold molecules under control! *Chemical Reviews*, 112(9):4949–5011.

Regal, C. A., Ticknor, C., Bohn, J. L., and Jin, D. S. (2003). Creation of ultracold molecules from a Fermi gas of atoms. *Nature*, 424(6944):47–50.

Rem, B. S., Grier, A. T., Ferrier-Barbut, I., Eismann, U., Langen, T., Navon, N., Khaykovich, L., Werner, F., Petrov, D. S., Chevy, F., and Salomon, C. (2013). Lifetime of the Bose gas with resonant interactions. *Phys. Rev. Lett.*, 110:163202.

Repp, M. (2013). *Interspecies Feshbach Resonances in an Ultracold, Optically Trapped Bose-Fermi Mixture of Cesium and Lithium*. PhD thesis, Ruperto-Carola-University of Heidelberg.

Repp, M., Pires, R., Ulmanis, J., Heck, R., Kuhnle, E. D., Weidemüller, M., and Tiemann, E. (2013). Observation of interspecies ^{6}Li-^{133}Cs Feshbach resonances. *Phys. Rev. A*, 87:010701.

Riisager, K. (2013). Halos and related structures. *Physica Scripta*, 2013(T152):014001.

Rittenhouse, S. T., von Stecher, J., D'Incao, J. P., Mehta, N. P., and Greene, C. H. (2011). The hyperspherical four-fermion problem. *Journal of Physics B: Atomic, Molecular and Optical Physics*, 44(17):172001.

Roy, S., Landini, M., Trenkwalder, A., Semeghini, G., Spagnolli, G., Simoni, A., Fattori, M., Inguscio, M., and Modugno, G. (2013). Test of the universality of the three-body Efimov parameter at narrow Feshbach resonances. *Phys. Rev. Lett.*, 111:053202.

Sakurai, J. J. and Napolitano, J. J. (2010). *Modern Quantum Mechanics*. Addison-Wesley.

Samboy, N. and Côté, R. (2013). Rubidium Rydberg linear macrotrimers. *Phys. Rev. A*, 87:032512.

Schempp, H., Günter, G., Robert-de Saint-Vincent, M., Hofmann, C. S., Breyel, D., Komnik, A., Schönleber, D. W., Gärttner, M., Evers, J., Whitlock, S., and Weidemüller, M. (2014). Full counting statistics of laser excited Rydberg aggregates in a one-dimensional geometry. *Phys. Rev. Lett.*, 112:013002.

Schirotzek, A., Wu, C.-H., Sommer, A., and Zwierlein, M. W. (2009). Observation of Fermi polarons in a tunable Fermi liquid of ultracold atoms. *Phys. Rev. Lett.*, 102:230402.

Schmidt, R., Rath, S., and Zwerger, W. (2012). Efimov physics beyond universality. *The European Physical Journal B*, 85(11):1–6.

Schönhals, A. (2013). Imaging of ultracold cesium atoms at high magnetic fields. Master's thesis, Ruprecht-Karls-Universität Heidelberg, Germany.

Schöllkopf, W. and Toennies, J. P. (1994). Nondestructive mass selection of small van der Waals clusters. *Science*, 266(5189):1345–1348.

Schuster, T., Scelle, R., Trautmann, A., Knoop, S., Oberthaler, M. K., Haverhals, M. M., Goosen, M. R., Kokkelmans, S. J. J. M. F., and Tiemann, E. (2012). Feshbach spectroscopy and scattering properties of ultracold Li + Na mixtures. *Phys. Rev. A*, 85:042721.

Schwabl, F. (2007). *Quantenmechanik*. Springer-Verlag.

Serwane, F., Zürn, G., Lompe, T., Ottenstein, T. B., Wenz, A. N., and Jochim, S. (2011). Deterministic preparation of a tunable few-fermion system. *Science*, 332(6027):336–338.

Silber, C., Günther, S., Marzok, C., Deh, B., Courteille, P. W., and Zimmermann, C. (2005). Quantum-degenerate mixture of fermionic lithium and bosonic rubidium gases. *Phys. Rev. Lett.*, 95:170408.

Simons, J. (2008). Molecular anions. *The Journal of Physical Chemistry A*, 112(29):6401–6511. PMID: 18630888.

Sørensen, P. K., Fedorov, D. V., Jensen, A. S., and Zinner, N. T. (2012). Efimov physics and the three-body parameter within a two-channel framework. *Phys. Rev. A*, 86:052516.

Sørensen, P. K., Fedorov, D. V., Jensen, A. S., and Zinner, N. T. (2013a). Finite-range effects in energies and recombination rates of three identical bosons. *Journal of Physics B: Atomic, Molecular and Optical Physics*, 46(7):075301.

Sørensen, P. K., Fedorov, D. V., Jensen, A. S., and Zinner, N. T. (2013b). Three-body recombination at finite energy within an optical model. *Phys. Rev. A*, 88:042518.

Sørensen, P., Fedorov, D., and Jensen, A. (2013). Three-body recombination rates near a Feshbach resonance within a two-channel contact interaction model. *Few-Body Systems*, 54(5-6):579–590.

Staanum, P., Pashov, A., Knöckel, H., and Tiemann, E. (2007). $X^1\Sigma^+$ and $a^3\Sigma^+$ states of LiCs studied by Fourier-transform spectroscopy. *Phys. Rev. A*, 75:042513.

Stellmer, S., Tey, M. K., Huang, B., Grimm, R., and Schreck, F. (2009). Bose-Einstein condensation of strontium. *Phys. Rev. Lett.*, 103:200401.

Stoof, H. T. C., Koelman, J. M. V. A., and Verhaar, B. J. (1988). Spin-exchange and dipole relaxation rates in atomic hydrogen: Rigorous and simplified calculations. *Phys. Rev. B*, 38:4688–4697.

Strauss, C., Takekoshi, T., Lang, F., Winkler, K., Grimm, R., Hecker Denschlag, J., and Tiemann, E. (2010). Hyperfine, rotational, and vibrational structure of the $a^3\Sigma_u^+$ state of $^{87}Rb_2$. *Phys. Rev. A*, 82:052514.

Stuhler, J., Griesmaier, A., Koch, T., Fattori, M., Pfau, T., Giovanazzi, S., Pedri, P., and Santos, L. (2005). Observation of dipole-dipole interaction in a degenerate quantum gas. *Phys. Rev. Lett.*, 95:150406.

Suno, H., Esry, B. D., Greene, C. H., and Burke, J. P. (2002). Three-body recombination of cold helium atoms. *Phys. Rev. A*, 65:042725.

Takekoshi, T., Reichsöllner, L., Schindewolf, A., Hutson, J. M., Le Sueur, C. R., Dulieu, O., Ferlaino, F., Grimm, R., and Nägerl, H.-C. (2014). Ultracold dense samples of dipolar RbCs molecules in the rovibrational and hyperfine ground state. *Phys. Rev. Lett.*, 113:205301.

Tanaka, K., Yamaguchi, T., Suzuki, T., Ohtsubo, T., Fukuda, M., Nishimura, D., Takechi, M., Ogata, K., Ozawa, A., Izumikawa, T., Aiba, T., Aoi, N., Baba, H., Hashizume, Y., Inafuku, K., Iwasa, N., Kobayashi, K., Komuro, M., Kondo, Y., Kubo, T., Kurokawa, M., Matsuyama, T., Michimasa, S., Motobayashi, T., Nakabayashi, T., Nakajima, S., Nakamura, T., Sakurai, H., Shinoda, R., Shinohara, M., Suzuki, H., Takeshita, E., Takeuchi, S., Togano, Y., Yamada, K., Yasuno, T., and Yoshitake, M. (2010). Observation of a large reaction cross section in the drip-line nucleus $^{22}\mathbf{C}$. *Phys. Rev. Lett.*, 104:062701.

Thalhammer, G., Barontini, G., Catani, J., Rabatti, F., Weber, C., Simoni, A., Minardi, F., and Inguscio, M. (2009). Collisional and molecular spectroscopy in an ultracold Bose-Bose mixture. *New Journal of Physics*, 11(5):055044.

Thøgersen, M., Fedorov, D. V., and Jensen, A. S. (2008). N-body Efimov states of trapped bosons. *EPL (Europhysics Letters)*, 83(3):30012.

Thomas, L. H. (1935). The interaction between a neutron and a proton and the structure of H^3. *Phys. Rev.*, 47:903–909.

Thompson, S. T., Hodby, E., and Wieman, C. E. (2005). Ultracold molecule production via a resonant oscillating magnetic field. *Phys. Rev. Lett.*, 95:190404.

Ticknor, C., Regal, C. A., Jin, D. S., and Bohn, J. L. (2004). Multiplet structure of Feshbach resonances in nonzero partial waves. *Phys. Rev. A*, 69:042712.

Ticknor, C. and Rittenhouse, S. T. (2010). Three body recombination of ultracold dipoles to weakly bound dimers. *Phys. Rev. Lett.*, 105:013201.

Timmermans, E., Tommasini, P., Hussein, M., and Kerman, A. (1999). Feshbach resonances in atomic Bose-Einstein condensates. *Physics Reports*, 315(1–3):199 – 230.

Treutlein, P., Chung, K. Y., and Chu, S. (2001). High-brightness atom source for atomic fountains. *Phys. Rev. A*, 63:051401.

Tscherbul, T. V., Calarco, T., Lesanovsky, I., Krems, R. V., Dalgarno, A., and Schmiedmayer, J. (2010). rf-field-induced Feshbach resonances. *Phys. Rev. A*, 81:050701.

Tscherbul, T. V. and Rittenhouse, S. T. (2011). Three-body radio-frequency association of Efimov trimers. *Phys. Rev. A*, 84:062706.

Tung, S.-K., Jiménez-García, K., Johansen, J., Parker, C. V., and Chin, C. (2014). Geometric scaling of Efimov states in a ^{6}Li-^{133}Cs mixture. *Phys. Rev. Lett.*, 113:240402.

Tung, S.-K., Parker, C., Johansen, J., Chin, C., Wang, Y., and Julienne, P. S. (2013). Ultracold mixtures of atomic ^{6}Li and ^{133}Cs with tunable interactions. *Phys. Rev. A*, 87:010702.

Ulmanis, J., Häfner, S., Pires, R., Kuhnle, E. D., Weidemüller, M., and Tiemann, E. (2015). Universality of weakly bound dimers and efimov trimers close to Li–Cs Feshbach resonances. *New Journal of Physics*, 17(5):055009.

Voigtsberger, J., Zeller, S., Becht, J., Neumann, N., Sturm, F., Kim, H.-K., Waitz, M., Trinter, F., Kunitski, M., Kalinin, A., Wu, J., Schöllkopf, W., Bressanini, D., Czasch, A., Williams, J. B., Ullmann-Pfleger, K., Schmidt, L. P. H., Schöffler, M. S., Grisenti, R. E., Jahnke, T., and Dörner, R. (2014). Imaging the structure of the trimer systems $^{4}He_3$ and $^{3}He^{4}He_2$. *Nat Commun*, 5:5765.

von Stecher, J. (2010). Weakly bound cluster states of Efimov character. *Journal of Physics B*, 43.

von Stecher, J. (2011). Five- and six-body resonances tied to an Efimov trimer. *Phys. Rev. Lett.*, 107:200402.

von Stecher, J., D/'Incao, J. P., and Greene, C. H. (2009). Signatures of universal four-body phenomena and their relation to the Efimov effect. *Nat Phys*, 5(6):417–421.

Vuletić, V., Chin, C., Kerman, A. J., and Chu, S. (1998). Degenerate Raman sideband cooling of trapped cesium atoms at very high atomic densities. *Phys. Rev. Lett.*, 81:5768–5771.

Wang, J., D'Incao, J. P., Esry, B. D., and Greene, C. H. (2012a). Origin of the three-body parameter universality in Efimov physics. *Phys. Rev. Lett.*, 108:263001.

Wang, J., D'Incao, J. P., Wang, Y., and Greene, C. H. (2012b). Universal three-body recombination via resonant d-wave interactions. *Phys. Rev. A*, 86:062511.

Wang, Y. (2015). Private communication.

Wang, Y., D'Incao, J. P., and Esry, B. D. (2011a). Ultracold three-body collisions near narrow Feshbach resonances. *Phys. Rev. A*, 83:042710.

Wang, Y., D'Incao, J. P., and Esry, B. D. (2013). *Ultracold Few-Body Systems*, volume 62 of *Advances in Atomic, Molecular, and Optical Physics*. Academic Press.

Wang, Y., D'Incao, J. P., and Greene, C. H. (2011b). Efimov effect for three interacting bosonic dipoles. *Phys. Rev. Lett.*, 106:233201.

Wang, Y., D'Incao, J. P., and Greene, C. H. (2011c). Universal three-body physics for fermionic dipoles. *Phys. Rev. Lett.*, 107:233201.

Wang, Y., D'Incao, J. P., Nägerl, H.-C., and Esry, B. D. (2010). Colliding Bose-Einstein condensates to observe Efimov physics. *Phys. Rev. Lett.*, 104:113201.

Wang, Y. and Esry, B. D. (2011). Universal three-body physics at finite energy near Feshbach resonances. *New Journal of Physics*, 13(3):035025.

Wang, Y. and Greene, C. (2015). Private commnunication.

Wang, Y. and Greene, C. H. (2012). Universal bound and scattering properties for two dipoles. *Phys. Rev. A*, 85:022704.

Wang, Y. and Julienne, P. S. (2014). Universal van der Waals physics for three cold atoms near Feshbach resonances. *Nat Phys*, 10:768–773.

Wang, Y., Julienne, P. S., and Greene, C. H. (2014). Few-body physics of ultracold atoms and molecules with long-range interactions. *ArXiv:1412.8094*.

Wang, Y., Laing, W. B., von Stecher, J., and Esry, B. D. (2012c). Efimov physics in heteronuclear four-body systems. *Phys. Rev. Lett.*, 108:073201.

Wang, Y., Wang, J., D'Incao, J. P., and Greene, C. H. (2012d). Universal three-body parameter in heteronuclear atomic systems. *Phys. Rev. Lett.*, 109:243201.

Weber, C., Barontini, G., Catani, J., Thalhammer, G., Inguscio, M., and Minardi, F. (2008). Association of ultracold double-species bosonic molecules. *Phys. Rev. A*, 78:061601.

Weber, T. (2003). *Bose-Einstein Condensation of Optically Trapped Cesium*. PhD thesis, University of Innsbruck.

Weber, T., Herbig, J., Mark, M., Nägerl, H.-C., and Grimm, R. (2003). Three-body recombination at large scattering lengths in an ultracold atomic gas. *Phys. Rev. Lett.*, 91:123201.

Wenz, A. N., Lompe, T., Ottenstein, T. B., Serwane, F., Zürn, G., and Jochim, S. (2009). Universal trimer in a three-component Fermi gas. *Phys. Rev. A*, 80:040702.

Wenz, A. N., Zürn, G., Murmann, S., Brouzos, I., Lompe, T., and Jochim, S. (2013). From few to many: Observing the formation of a Fermi sea one atom at a time. *Science*, 342(6157):457–460.

Wigner, E. P. (1948). On the behavior of cross sections near thresholds. *Phys. Rev.*, 73:1002–1009.

Wild, R. J., Makotyn, P., Pino, J. M., Cornell, E. A., and Jin, D. S. (2012). Measurements of Tan's contact in an atomic Bose-Einstein condensate. *Phys. Rev. Lett.*, 108:145305.

Williams, J. R., Hazlett, E. L., Huckans, J. H., Stites, R. W., Zhang, Y., and O'Hara, K. M. (2009). Evidence for an excited-state Efimov trimer in a three-component Fermi gas. *Phys. Rev. Lett.*, 103:130404.

Wilson, K. G. (1983). The renormalization group and critical phenomena. *Rev. Mod. Phys.*, 55:583–600.

Wu, C. F. J. (1986). Jackknife, bootstrap and other resampling methods in regression analysis. *Ann. Statist.*, 14(4):1261–1295.

Wu, C.-H., Park, J. W., Ahmadi, P., Will, S., and Zwierlein, M. W. (2012). Ultracold fermionic Feshbach molecules of ^{23}Na^{40}K. *Phys. Rev. Lett.*, 109:085301.

Xie, T., Wang, G.-R., Huang, Y., Zhang, W., and Cong, S.-L. (2012). The radio frequency field modulation of magnetically induced heteronuclear Feshbach resonance. *Journal of Physics B: Atomic, Molecular and Optical Physics*, 45(14):145302.

Yamashita, M., Fedorov, D., and Jensen, A. (2011). Brunnian and Efimov n-body states. *Few-Body Systems*, 51(2-4):135–151.

Yamashita, M. T., Bellotti, F. F., Frederico, T., Fedorov, D. V., Jensen, A. S., and Zinner, N. T. (2013). Single-particle momentum distributions of Efimov states in mixed-species systems. *Phys. Rev. A*, 87:062702.

Zaccanti, M., Deissler, B., D'Errico, C., Fattori, M., Jona-Lasinio, M., Müller, S., Roati, G., Inguscio, M., and Modugno, G. (2009). Observation of an Efimov spectrum in an atomic system. *Nat Phys*, 5(8):586–591.

Zenesini, A., Huang, B., Berninger, M., Besler, S., Nägerl, H.-C., Ferlaino, F., Grimm, R., Greene, C. H., and von Stecher, J. (2013). Resonant five-body recombination in an ultracold gas of bosonic atoms. *New Journal of Physics*, 15(4):043040.

Zenesini, A., Huang, B., Berninger, M., Nägerl, H.-C., Ferlaino, F., and Grimm, R. (2014). Resonant atom-dimer collisions in cesium: Testing universality at positive scattering lengths. *Phys. Rev. A*, 90:022704.

Zhang, S. and Ho, T.-L. (2011). Atom loss maximum in ultra-cold Fermi gases. *New Journal of Physics*, 13(5):055003.

Zhen, Z. and Macek, J. (1988). Loosely bound states of three particles. *Phys. Rev. A*, 38:1193–1201.

Zhu, S. and Tan, S. (2013). Universality in s-wave and higher partial-wave Feshbach resonances: An illustration with a single atom near two scattering centers. *Phys. Rev. A*, 87:063629.

Zhukov, M., Danilin, B., Fedorov, D., Bang, J., Thompson, I., and Vaagen, J. (1993). Bound state properties of Borromean halo nuclei: ^{6}He and ^{11}Li. *Physics Reports*, 231(4):151 – 199.

Zinner, N. T. and Jensen, A. S. (2013). Comparing and contrasting nuclei and cold atomic gases. *Journal of Physics G: Nuclear and Particle Physics*, 40(5):053101.

Zürn, G., Lompe, T., Wenz, A. N., Jochim, S., Julienne, P. S., and Hutson, J. M. (2013). Precise characterization of ^{6}Li Feshbach resonances using trap-sideband-resolved rf spectroscopy of weakly bound molecules. *Phys. Rev. Lett.*, 110:135301.

Zürn, G., Serwane, F., Lompe, T., Wenz, A. N., Ries, M. G., Bohn, J. E., and Jochim, S. (2012). Fermionization of two distinguishable fermions. *Phys. Rev. Lett.*, 108:075303.

Zürn, G., Wenz, A. N., Murmann, S., Bergschneider, A., Lompe, T., and Jochim, S. (2013). Pairing in few-fermion systems with attractive interactions. *Phys. Rev. Lett.*, 111:175302.

Acknowledgements

This thesis would not have been possible without the support and help from a large number of different sources and people, to whom I would like to express my deepest gratitude. The synergy between each one of them made this journey and the present destination possible.

I would like to thank Prof. Dr. Matthias Weidemüller for giving me the opportunity to pursue an exceptionally interesting and challenging PhD work in a vibrant and highly international group of extraordinary people. His continuous readiness to explain and discuss all the aspects of any question, from the most simplest to the most complicated ones, was a fantastic experience. Through the independent and at the same time interdependent working culture I could grow not only as a scientist, but also as a colleague and a person.

A special thanks goes to Prof. Dr. Selim Jochim for becoming my thesis referee and being my advisor. His persistent and adhesive enthusiasm for physics and the habit of asking tricky questions about the nature and our research was invaluable during all the stages of my work in Heidelberg.

It was a great pleasure to work in the Mixtures team, everyone of whom was always ready to spend long hours in the lab building up and measuring, as well as cracking hard physics challenges in an equally long and sometimes neverending discussions. It was a privilege to work and relax to together with them. I thank Dr. Marc Repp for the planning and setting up of an excellent apparatus and for a lot of fun in the lab and office, and out of them. Dr. Rico Pires for his always logical and structured approach to every problem and great management skills. Dr. Eva Kuhnle for the consistent generation of ideas and for so often being the driving force behind further developments on our experiment. Stephan Häfner for his critical thinking and readiness to tackle almost any challenge we threw at him. Alda Arias for the outstanding implementation of the second-generation reservoir trap and reminding us about the things outside the physics world. Carmen Renner for the great development of our next-generation imaging system and for brightening up our discussions so often. Arthur Schönhals for the superior work on the high-field imaging system and tough battles on a kicker table. Robert Heck for establishing the high-power dipole trap technology in our setup and trust in me as his supervisor.

Stefan Schmidt and Romain Müller for the exemplary setup of magneto-optical trapping and cooling system and for bringing joy into much of the initial stages of the experiment. Kristina Meyer for the first-generation reservoir trap, Manuel Gerken for the first approach to our gray-molasses cooling, Thomas Kirchner and Stefan Arnold for their early-stage contributions to our magic wavelength trap and magnetic field generation. Yicheng Zhang, Zhaodi Pan, and Jian-Pei Ang for their help in developing simple models for understanding the Li-Cs better. Andy McCulloch and Rodrigo Shiozaki for visiting and helping in the lab to get our very first experiments going.

I would like to thank all of our collaborators, from whom I could learn a lot about physics and our field. I thank Prof. Dr. E. Tiemann for his superb numerical support and involved discussions not only about molecular physics but also life in general. Dr. Dmitry Petrov for elucidating the zero-range three-body problem to us and indispensable assistance in developing the numerics to do so. Prof. Chris Greene and Dr. Yujun Wang for their willingness to take on a lot of exhaustive discussions about few-body physics and the excellent job in explaining our findings via hyperspherical calculations. Prof. Dr. John Bohm, Dr. Tobias Tiecke and Brandon Ruzic for their analysis of our measurements in the Li-Cs two-body sector and many fruitful discussions. Dr. Johannes Deiglmayr for his instrumental contributions to the special issue on ultracold molecule photoassociation and pleasant and enlightening conversations at various moments through these last years.

The great working atmosphere and the rapid progress of technology in our experiments that I was privileged to enjoy was a result of continuous effort of each group member. Therefore, I thank the Rydberg team around Dr. Georg Günter, Dr. Hanna Schempp, Dr. Christoph Hofmann, Vladislav Gavryusev, and Miguel Ferreira Cao, the HAITrap team around Bastian Höltkemeier, Henry Lopez, and Pascal Weckesser, and the EQM team around Dr. Shannon Whitlock, Stephan Helmrich, and Alda Arias for their steady exchange of ideas and developments with us in and out of the lab. They made the time spent working indeed worthwhile, and often created pleasant distractions from physics.

I thank the Ultracold Quantum Gases group, especially, but not limited to, Gerhard Zürn, Andre Wenz, Martin Ries, and Andrea Bergschneider for teaching us how to tame ultracold Li atoms and for their deep technical and physics knowledge that they were always willing to share. The group of Quantum Optics and Information that is led on the experimental front by Andreas Reingruber and Bing Yang for many fruitful discussions with them.

The realization of many technical aspects of our setup was enabled by the expertise of the mechanical and electronic workshops. I express my gratitude for the excellent collaboration with all the members from them. Ralf Ziegler and Dominic Litsch for always finding the perfect solutions for any of our mechanical problems.

Dr. Venelin Angelov, Esteban Rubio, and Peter von Walter for creating our experimental control system and so many more outstanding designs, and their infinite patience to teach me a lot about electronics. Frank Schumacher and Klaus Layer for their outstanding skill in building new electronic devices and support with the old ones. A special thanks goes to Claudia Krämer for helping with uncountable piles of administrative and organizational questions.

This journey was profoundly enriched by a lot of extraordinary people outside the Physics Institute and Heidelberg. I thank Prof. Dr. Rudolf Grimm, Prof. Dr. Christophe Salomon, Prof. Dr. Lincoln Carr, Prof. Dr. Olivier Dulieu, Dr. Jose D'Incao, Dr. Nikolaj Zinner, and Dr. Thomas Lompe for numerous insightful discussions that have been highly instructive in various aspects. I am indebted to the exchange of exciting ideas and sparkling conversations about all possible topics with Prof. Dr. Vyacheslavs Kashcheyevs, which were always great fun to be a part of. I am very grateful for the engaging time at LU in the dynamic group of Dr. Aigars Ekers, and his guidance during my early studies that has left a deep impact on me as a physicist.

My studies and research were immensely enhanced by the interconnected academic framework, in which I was proud to participate. I thank DAAD for providing me with a stipend and excellent opportunities to meet and connect with great people from all over the world. HGSFP and IMPRS-QD for their financial support and for outstanding seminars and various kinds of events, which altogether made my time as a graduate student in Heidelberg and Germany remarkable.

At last, but not least, I thank everyone else who helped me during this time. Especially, my family for their unlimited support in all possible and impossible ways, I am really happy to have you. And my most deepest thanks to my girlfriend Ieva for always being there for me, for her shining smile, understanding, and love.